Ultrasonic and Magnetic Investigations
in Frustrated Low-Dimensional Spin Systems

Dissertation

zur Erlangung des Doktorgrades

der Naturwissenschaften

vorgelegt beim Fachbereich Physik

der JohannWolfgang Goethe Universität

in Frankfurt am Main

von

Pham Thanh Cong

aus Hanoi, Vietnam

Frankfurt am Main (2011)

(D30)

vom Fachbereich Physik

der Johann Wolfgang Goethe-Universität

als Dissertation angenommen.

Dekan: Prof. Dr. Michael Huth

Gutachter:

1. Prof. Dr. Michael Lang

2. Prof. Dr. Wolf Assmus

Datum der Disputation:

Kính tặng bố mẹ:

Phạm Ngọc Thành

Nguyễn Thị Hải Yến

This thesis is dedicated to my parents
for their endless love, sacrificing
and encouragement.

KURZFASSUNG

.

In der modernen Festkörperphysik spielen elektronisch stark korrelierte Systeme mit ihrem komplexen Vielteilchenverhalten eine zentrale Rolle. Insbesondere das Wechselspiel zwischen thermischen und Quantenfluktuationen in den Ladungs- und Spinfreiheitsgraden führt zur Entstehung verschiedenster neuartiger Grundzustände.

Die vorliegende Dissertation „Ultrasonic and Magnetic Investigations in frustrated Low-dimensional Spin Systems" beschäftigt sich mit den besonderen physikalischen Eigenschaften niedrig dimensionaler Spinsysteme. Diese Materialklasse, die auch zu den stark korrelierten Systemen zählt, wird seit vielen Jahren intensiv sowohl experimentell als auch theoretisch untersucht. Auf theoretischer Seite sind die niedrigdimensionalen Spinsysteme besonders interessant, da sie als Modellsysteme die exakte Beschreibung des Grundzustandes und des Anregungsspektrums ermöglichen. Von experimenteller Seite ist es in den letzten Jahrzehnten gelungen, verschiedenste Materialklassen niedrigdimensionaler Spinsysteme zu synthetisieren.

In der vorliegenden Arbeit werden die grundlegenden Theorien und physikalischen Konzepte niedrigdimensionaler Spinsysteme diskutiert. Insbesondere auch die Spin-Phonon-Wechselwirkung dieser Materialien, die für die hier beobachteten elastischen Anomalien verantwortlich ist. Weiterhin wird auch das elastische Verhalten bei magnetischen Phasenübergängen beschrieben.

Da die Ultraschallexperimente einen Schwerpunkt dieser Arbeit bilden, wird der Versuchsaufbau zur phasenempfindlichen Detektion von Schallgeschwindigkeit und Ultraschalldämfung ausführlich

beschrieben. Diese Messmethode ist ideal zur Untersuchung der Spin-Phonon Wechselwirkung geeignet.

Die elastische Konstante, die aus der Schallgeschwindigkeit bestimmt werden kann, ist eine thermodynamische Größe. Sie ist die zweite Ableitung der freien Energie nach der Verzerrung und daher mit anderen thermodynamischen Größen wie zum Beispiel der spezifischen Wärme oder aber auch der Magnetisierung verknüpft. Die elastische Konstante zeigt daher auch bei magnetischen Phasenübergängen ausgeprägte Anomalien, die mit Dämpfungseffekten verbunden sind. Die Ultraschalldämpfung ist im Gegensatz zur elastischen Konstanten eine Transportgröße. Beide Größen zeigen aber bei magnetischen Phasenübergängen ein kritisches Verhalten. Die gewonnen Ergebnisse lassen sich sehr gut mit denen anderer thermodynamische Experimente oder Spektroskopischen Untersuchungen vergleichen.

Die Ultraschalluntersuchungen wurden über einen weiten Temperaturbereich von 0.03 K bis 300 K in magnetischen dc-Feldern bis 12 T durchgeführt. Für ein spezielles Experiment am quasi 2D-Heisenberg Antiferromagneten Cs_2CuBr_4 wurden die Messungen in gepulsten Magnetfeldern bis 50 T gemacht.

Das natürliche Mineral Azurit ist ein Modellsystem für eine quasi 1D Spinkette. Die magnetischen Ionen in Azurit sind Cu^{2+}, also Spin S = 1/2, die mit zwei dominanten magnetischen Wechselwirkungen J_1 und J_2 miteinander in Form einer verzerrten ($J_1 \neq J_2$) Diamandkette miteinander verknüpft sind. Daher handelt es sich bei Azurit um ein frustriertes magnetisches System.

In der vorliegenden Arbeit wurde die longitudinale c_{22}-Mode im gesamten Temperaturbereich für unterschiedliche Orientierungen des externen Magnetfeldes untersucht. Dabei führt die ausgeprägte Spin-Phonon Wechselwirkung dieses Systems zu deutlichen Anomalien in den

elastischen Konstanten bei 20 K und 5 K, worin sich die relevanten Energieskalen des Systems widerspiegeln.

Diese Ergebnisse decken sich mit denen, die aus thermischer Expansion und spezifischer Wärme gewonnen wurden. Aus der Temperaturabhängigkeit der c_{22}-Mode konnte die Verzerrungsabhängigkeit der dominanten magnetische Kopplungskonstante J_2 ermittelt werden, die sich direkt mit der aus magnetischen Suszeptibilitätsmessungen unter hydrostatischem Druck deckt.

Bedingt durch verschiedene deutlich kleinere magnetische Wechselwirkungen ordnet Azurit bei 1.88 K langreichweitig antiferromagnetisch. An diesem Phasenübergang wurde das kritische Verhalten der elastischen Konstanten und der Ultraschalldämpfung untersucht. Die dabei ermittelten kritischen Exponenten stimmen in der Schallgeschwindigkeit mit dem in den Neutronenstreuung gefundenen überein. Insbesondere an diesem Phasenübergang zeigt sich die starke Kopplung zwischen magnetischen und strukturellen Freiheitsgraden.

Die Tieftemperaturexperimente an Azurite im ^{3}He/^{4}He Mischkryostaten dienten vor allem dazu das komplexe BT-Phasendiagramm der Verbindung zu bestimmen. Dabei wurde eine bis dahin nicht bekannte magnetische Phase entdeckt und beschrieben.

Ein weiteres niedrigdimensinales Spinsystem, das in dieser Arbeit beschrieben wurde, ist Cs_2CuCl_4. Hier wurden die drei longitudinalen Moden c_{11}, c_{22} und c_{33} in externen Magnetfeldern für $B//a$ im gesamten Temperaturbereich vermessen.

Der Schwerpunkt der Messungen lag dabei auf Untersuchungen im Tieftemperaturbereich. Hier wurde das elastische Verhalten sowohl in der antiferromagnetischen Phase als auch im Spin-Flüssigkeitsbereich eingehend untersucht. Beide Bereiche zeichnen sich in allen untersuchten Moden durch ausgeprägte elastische Anomalien aus. In der geordneten Phase für nicht so sehr große Magnetfelder lassen sich sowohl die elastische Konstanten als auch die Ultraschalldämpfung mit Hilfe einer Spinwellentheorie beschreiben.

Für höhere Magnetfelder, um den quantenkritischen Punkt am Sättigungsfeld, gibt es zur Zeit noch keine mikrospische Theorie, so dass hier eine theoretische quantitative Analyse der elastischen

Anomalien nicht möglich ist. Dies gilt auch für den sehr ausgeprägten Spin-Flüssigkeitsbereich. Auffällig sind hier insbesondere die ausgeprägten Dämpfungsanomalien, die bis zu tiefsten Temperaturen verfolgt wurden. Dabei findet man um den quantenkritschen Punkt eine deutliche Doppelstruktur in der Dämpfung, aus deren Feld- und Temperaturabhängigkeit sich schließen lässt, dass sie zum einen vom Übergang aus der antiferromagnetischen Phase und zum anderen aus dem Spim-Flüssigkeitsbereich herrührt.

Abgeschlossen wurden die Ultraschalluntersuchen an den quasi 2D-Heisenberg Antiferromagneten durch Messung an Cs_2CuBr_4. Wegen des im Vergleich zum isostrukturellen Cl-System höheren kritischen Feldes von ~ 31 T für *B//a* wurden die Messungen in gepulsten Feldern bis 50 T durchgeführt. Dabei zeigte sich, ein ausgeprägtes Weichwerden in der c_{11}-Mode in Spin-Flüssigkeitsbereich.

Wie schon erwähnt, sind sowohl das Cl-System als auch das Br-System von Cs_2CuCl_4/Br_4 isostrukturell. Beide Verbindungen unterscheiden sich allerdings stark in der Beweglichkeit ihrer magnetischen Anregungen. Diese ist für das Cl-System recht groß. So dass man am unterhalb des quantenkritischen Punkts in der geordneten Phase die Kondensation von Magnonen beobachten kann.

In Gegensatz dazu ist die Beweglichkeit der magnetischen Anregungen im Br-System deutlich geringer, was zur Bildung von Plateaus in der Magnetisierung führt. Daher waren Untersuchungen an gemischten Systemen $Cs_2CuCl_{4-x}Br_x$ besonders interessant, um die Entwicklung der magnetischen Eigenschaften als Funktion der chemischen Zusammensetzung zu untersuchen.

Insgesamt wurden 18 verschiedene Konzentrationen im SQUID-Magnetometer untersucht. Dabei zeigt sich überaschender weise, dass es keine kontinuierliche Veränderung der magnetischen Eigenschaften gibt. Vielmehr lassen sich 3 Bereiche identifizieren, die sich in ihren magnetischen Eigenschaften deutlich unterscheiden. In der Arbeit wird gezeigt, dass mit Hilfe eines Modells der selektiven Substitution der Halogenionen das magnetische Verhalten erklärt werden kann. Dabei

existieren wohl zwei ausgezeichnet Konzentrationen, nämlich $x = 1$ und $x = 2$, wo völlig neuartige Verbindungen erwartete werden. Dies ist gleichzeitig der Ansatzpunkt für weitere Untersuchung in der Zukunft.

CONTENTS

.

Contents

9

1

INTRODUCTION

A major focus of modern condensed matter physics is the study of collective, many-body behavior in strongly-correlated systems. In these systems, the interplay of thermal and quantum fluctuations in both charge and spin degrees of freedom gives rise to many competing and co-existing novel phases. In this thesis, the focus of the study lies on a variety of compounds belonging to a class of correlated magnetic systems, called low-dimensional frustrated spin systems.

The low-dimensional spin system has a long history [Ising25, Bethe31] and for a number of reasons has now developed into one of the most active research fields of modern condensed matter physics.

Firstly, the interest in low-dimensional magnets is that these materials provide a unique possibility to study ground and excited states of quantum models. On the other hand, in contrast to magnetic systems with classical long-ranged ferro - or antiferromagnetic order, novel ground state properties arise due to the existence of strong quantum fluctuations in reduced dimensions and the interplay of quantum fluctuations and thermal fluctuations.

Secondly, this is a very attractive field for theoretical studies. Theorists were attracted by the chance of finding interesting exact results without having to deal with the hopelessly complicated case of models in 3D [Richter04]. A number of powerful numerical and analytical techniques has been developed including Density-Matrix-Renormalization-Group methods (DMRG), Quantum-Monte-Carlo simulations (QMC) and exact diagonalization (ED), or the Bethe ansatz for integrable models and field-theoretical approaches such as bosonization [Mikeska04].

Thirdly, the successful preparation of materials that are good realizations of quasi-two- or one-dimensional quantum magnets have rendered possible a fruitful interplay between theory and experiment. Actually, low-dimensional magnets have a natural realization since they exist as real bulk crystals thus having all the advantages of bulk materials in providing sufficient intensity for experiments investigating thermal properties (e.g. specific heat), as well as dynamic properties (in particular quantum excitations) by e.g. neutron scattering.

Frustrated magnetism has also become an extremely active field of research over the last decade. Frustration arises in magnetic systems when not all nearest-neighbor interaction energies can be simultaneously minimized. It creates a highly degenerated ground state in which the system can fluctuate with almost no energy expenditure, even down to a few mK in temperature thus preventing the formation of long-range magnetic order [Ong04, Heidarian05 and Greedan01]. In the absence of long-range magnetic order at low temperatures, spin-liquid states, characterized by a large remanent entropy associated with the fluctuating nature of the spins, are among the possible ground states of frustrated systems. The existence of spin liquids and their corresponding universality classes is a matter of intense debate both theoretically and experimentally as they exhibit many interesting properties. These consist of pressure or magnetic field-induced antiferromagnetic phase transitions, Bose-Einstein condensation (BEC), magnetization plateaux and possible applications in topological quantum computation, to name a few. They show both classical phases as well as new quantum phases with interesting cross-over regimes. New quantum phases are not only interesting in their own right, but they are also important for application, such as having an enhanced magnetocaloric effect in a frustrated spin system [Brück03], which may be useful for efficient magnetic refrigeration [Zhitomirsky03, Tegus02, Wolf11] or a natural candidate for quantum information processing applications [Gershoni06].

Among the various techniques used to investigate the properties of condensed matter is the ultrasound measurement, a powerful technique used to study phase transitions and critical phenomena. Physical acoustics embrace the measurements of ultrasonic velocity and attenuation. The elastic constants can be gained from the ultrasonic velocities. The elastic constants are thermodynamic derivatives, the second derivative of the free energy with respect to the strains. Therefore, they are directly related to the atomic and molecular bonding in the crystal. In addition, they are connected to thermal properties of solids through the Debye theory. In combination with specific heat and thermal expansion measurements, elastic constant data can be used to determine the equation of state and various thermodynamic functions. This technique has been well established as an important tool for the investigation of low-dimensional spin systems [Lüthi05, Sherman03 and Wolf00]. It is proven to be a powerful tool to probe the spin-lattice interactions [Wolf01a], lattice instabilities and phase transitions [Zherlitsyn10]. The investigation of the correlations between magnetic and lattice degrees of freedom provides a better understanding of the underlying physics of frustrated and low-dimensional spin systems. In this thesis, ultrasound will be used as the main

experimental technique while supplementary thermodynamic probes such as magnetic susceptibility and thermal expansion will be employed over wide ranges of temperature and magnetic field.

After a brief introduction and motivation, a description of interesting quantum spin systems studied in this thesis is given in Chapter 1. The other chapters are organized as follows:

- Chapter 2 contains relevant theoretical and material specific background in two parts. In the first part, I give a general introduction in the basic theories and concepts of low-dimensional spin systems including the phenomenon of frustration and its effect on magnetic ordering. In the second part, I present the basic theory of ultrasound as well as the necessary background of sound-wave propagation at magnetic phase transitions.

- Chapter 3 is devoted to the experimental technique. The ultrasound setup is discussed here in detail as it is the prime experimental method of the present work. In addition, the instrumentation to maintain the system at low temperature and the setup for magnetic susceptibility measurement will be shortly reviewed.

- Chapter 4 presents the study of the quasi-1D frustrated diamond chain compound Azurite.

- Chapter 5 deals with ultrasound studies of the 2D spin systems Cs_2CuCl_4 and Cs_2CuBr_4.

- Chapter 6 contains experimental details of the magnetic characterization of single crystals of the mixed system $Cs_2CuCl_{4-x}Br_x$.

- Chapter 7 In this chapter, a summary of the conclusions drawn from the research is presented and an outline is given for future research in this area.

2

GENERAL THEORETICAL ASPECTS

This chapter introduces some general theoretical aspects of quantum magnetism and physical acoustics necessary to understand the concepts presented in this thesis. In the first section, we examine the Heisenberg model, an effective description of the interaction of localized magnetic moments, and its solutions on some classical antiferromagnetic spin lattices. The second section is dedicated to the basic theory of sound-waves and ultrasound attenuation in an elastic media. The backgrounds on spin-phonon coupling mechanism and sound-wave propagation at a magnetic phase transition are also given.

2.1 Quantum magnets and spin liquids

2.1.1 Heisenberg model

When the temperature of a magnetic material is lowered sufficiently, it undergoes a phase transition from a disordered paramagnetic phase to an ordered magnetic phase. The temperature at which this occurs is called the Néel (T_N) or Curie (T_C) temperature, if the material is antiferromagnetic or ferromagnetic, respectively.

Spontaneous alignment of magnetic moments in magnetic material implies the presence of an internal field. This internal field is called the molecular field. In 1928, Heisenberg proposed that the molecular field, responsible for the magnetic ordering in solids, is the result of a spin-dependent exchange interaction between moments on neighboring lattice sites [Heisenberg28]. Furthermore, he proposed that the exchange (potential) energy between atoms of net spin S_i and S_j on neighboring sites is given by:

$$V_{ij} = J_{ij} S_i \cdot S_j. \tag{2.1}$$

Consequently, if $J_{ij} > 0$, the lowest energy configuration is when the spins are aligned anti-parallel to one another, corresponding to antiferromagnetic ordering (AFM) of the moments. In the case where $J_{ij} < 0$, the lowest energy configuration occurs when spins are aligned parallel to one another, resulting in a ferromagnetic ordering (FM) of the moments. The physical origin of the

exchange energy is governed by the laws of quantum mechanics. Electrons interact classically via Coulomb's law, and quantum mechanically via the Pauli Exclusion Principle. The exchange energy can then be thought of as the difference in potential energy of the parallel and anti-parallel spin states. This spin-dependent exchange energy is responsible for magnetic ordering in materials.

In describing a lattice of spins with the exchange energy given in Eq. 2.1, the Heisenberg Hamiltonian for the system is written as:

$$H = \sum_{ij} J_{ij} S_i S_j \tag{2.2}$$

where S_i is the total spin of the ith ion in the lattice. Exchange interactions fall off rapidly with increasing distance; thus it is sufficient to consider only nearest-neighbor exchange interactions. The term "nearest neighbors" means the moments which are physically closest to one another on a crystal lattice. On the hypothetical square lattice in Fig 2.1, the pairs of moments at lattice sites 1 and 2 and at sites 1 and 3 are nearest neighbors' pairs.
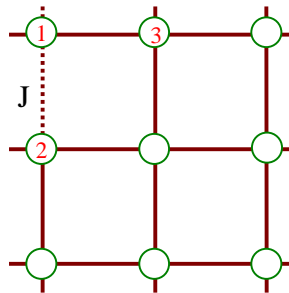
Figure 2.1 *Spin moments situated on a square lattice. Atoms 1 and 3, and 1 and 2 are nearest neighbors.*

2.1.2 Dimensionality and long-range ordering of spin systems

By specifying the dimension of the lattice as well as the dimension of the spin space, a useful classification of the possible spin models of the form in Eq. 2.2 can be constructed. On the one hand, restricting the spin space to one dimension leads to the Ising model, where the spins can only point in up or down direction. Similarly, we can restrict the spin space to two dimensions in an XY model or three dimensions in the Heisenberg model.

In the following, we restrict the study to the Heisenberg model. On the other hand, as introduced in Chapter 1 the exchange couplings *J* could be predominantly uni-directional, leading to the 1D spin

systems, such as the linear chain. They could also be predominant along two directions, leading to 2D spin systems, such as the square or triangular lattices (see Fig. 2.2). Finally, the exchange interactions could give rise to 3D spin systems.

The dimensionality of the lattice has profound consequences on the long-range ordering properties of the magnetic moments. Indeed, due to the Mermin-Wagner theorem [Mermin66], at any nonzero temperature, long-range order (meaning the presence of a bulk magnetization) is impossible in one and two dimensions in the isotropic Heisenberg model. Interestingly, nothing is said in the limit $T \rightarrow 0$. However, it turns out that one-dimensional antiferromagnetic spin chains described by Eq. 2.2 have a ground state with quasi-long-range order (the spin-spin correlation function decays at long distance following a power law), exactly calculated with the Bethe ansatz. The excitation spectrum of the spin chain exhibits interesting properties, such as a gapless excitation spectrum with deconfined fractional elementary excitations, known as spinons.

a) Linear chain

b) Square lattice   c) Triangular lattice
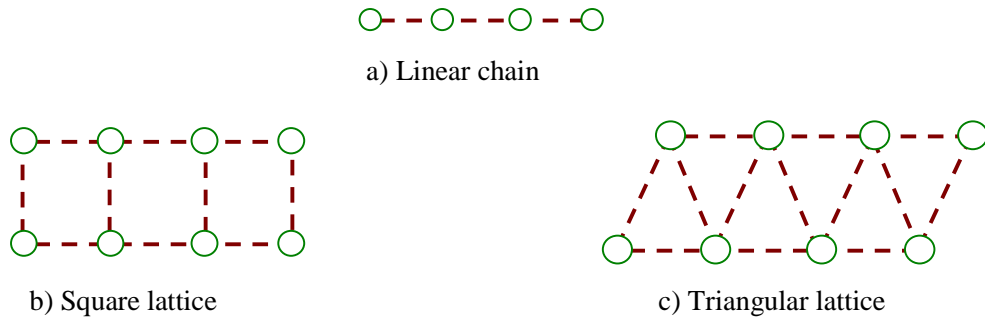
Figure 2.2 The most common spin lattices studied theoretically are the linear chain (a), the square lattice (b) and the triangular lattice (c).

The two-dimensional lattices show long-range ordering at $T = 0$. For example, on the square lattice, the ground state is Néel ordered at wave vector q = (π , π) and with $S = 1$ transverse spin-wave excitations [Lüther75]. The same situation is true for the isotropic triangular lattice. At the classical level, the minimum energy configuration is the well-known 120° Néel state. At the quantum level, numerical work indicates that even in the presence of strong quantum fluctuations (the magnetization is reduced by about 59% from its classical value), long-range order with an ordering vector ($q = (2\pi/3 , 2\pi/3)$ is still favored [Manousakis91].

In three-dimensional lattices, such as the cubic lattice or the inter-coupled lattice the Heisenberg antiferromagnet (HAF) can order at finite temperature ($T > 0$). The associated ordered spin structure

is shown in Fig. 2.3. For $T > T_N$, the spin system is found in the paramagnetic state, where each magnetic moment behaves independently. The emergence of long-range order breaks the spin-rotation symmetry and the system can be treated by the Landau theory of phase transitions. In this theory, an order parameter ψ is defined such that $\psi = 0$ in the paramagnetic phase (symmetric phase) and $\psi \neq 0$ in the ordered phase (broken-symmetry phase). Elementary excitations in long-range ordered system are found by linearizing the equations of motion of the local deviations of the spins from their ground state positions [Blundell01, Coldea03]. The resulting low-lying excitations are called magnons and obey the Bose-Einstein statistics. They can be pictured as long-wavelength deformations of the order parameter. They represent the conventional behavior of the elementary excitations in long-range-ordered systems.
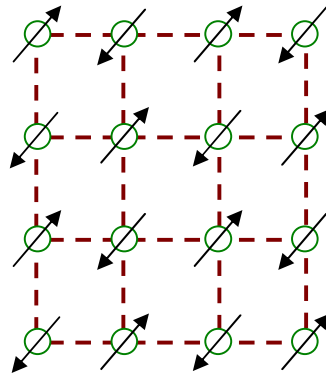
Figure 2.3 *Antiferromagnetic long-range order on the square lattice*

Thermal fluctuations can lead to the destruction of long-range order, as we saw in the 3D case for $T > T_N$. A similar situation could arise at $T = 0$ where the long-range order can be weakened by quantum fluctuations. Quantum effects are amplified in a magnetic system with a low value of the spin, e.g. $S = 1/2$ or $S = 1$, in the presence of antiferromagnetic coupling and in low-dimensional lattices (1D or 2D lattices) with a small number of nearest-neighbors [Rice02]. The consequences of these quantum fluctuations are a renormalization of the ground-state energy and a reduction of the magnetization [Lhuillier02]. Ultimately, quantum fluctuations can lead to the destruction of long-range order and a preference for a quantum ground state with high symmetry and small degeneracy.

2.1.3 Frustration

A spin system is called frustrated when it cannot satisfy simultaneously all its interactions between every pair of spins. The resulting configurations minimize the energy of the whole system,

but not all the energies of interactions between one spin and its neighbors. Frustrated systems exhibit interesting properties such as a very large ground-state degeneracy. Particular interest in those magnetic systems stems from the fact that they were found to present new phases such as Resonating Valence Bonds (RVB) spin liquids [Anderson73], super solids [Wessel05, Melko05] and spin ices [Bramwell01, Castelnovo08].

Frustration has two possible origins: it can arise either from competing magnetic interactions, such as in the $J_1 - J_2$ spin chain, or from geometry. Geometric frustration will be illustrated through a couple of examples among the family of corner-sharing lattices [Moessner01]. The exploration of frustrated systems is a wide and expanding field of condensed matter physics. The purpose of this section is just to gives a brief overview on frustrated systems. Reviews on frustrated quantum magnets can be found in Ref. [Anderson73] or [Misguich01].

In the case of frustration that arises from competing interactions, let us consider a pair of two nearest-neighbor spins interacting through an antiferromagnetic coupling J_1. The energy of this pair is minimized if the spins are antiparallel (Néel order). If we add a next-nearest-neighbor antiferromagnetic interaction J_2 and J_2 is "low enough", each nearest-neighbor pair (S_i, S_{i+1}) still tends to align antiparallel. However, above a certain value of J_2, the pairs of next-nearest-neighbors (S_i, S_{i+2}) will also try to lie antiparallel, which is impossible due to the J_1 coupling. As a consequence, for a range of values of the ratio J_1/J_2, the interplay between the two antiferromagnetic couplings will lead to a non-collinear configuration, a spiral state, that does not fully satisfy any of the interactions. In such case the system is *frustrated by the competition* between the J_1 and J_2 couplings.
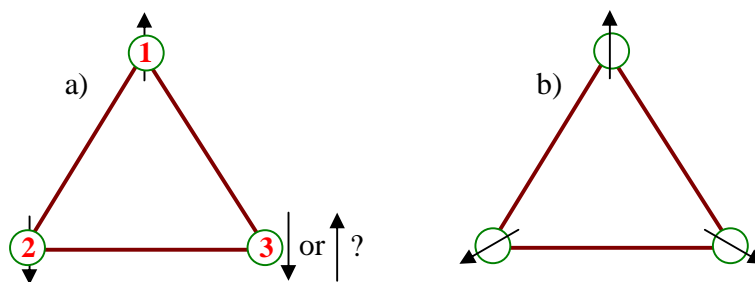

Figure 2.4 *The geometry of the triangular lattice (a) prohibits AF ordering since spin 3 cannot be aligned antiparallel to both of its nearest neighbors 1 and 2. The system is said to be frustrated. (b) Possible ordered phases in a triangular antiferromagnetic (TAF), derived from simplified expression for the total energy of the system.*

In the case of geometric frustration, the simplest example to illustrate these kinds of systems is a triangular lattice with antiferromagnetic couplings J on all edges. In order to satisfy independently all interactions, spins should align antiparallel along each edge, which is not possible as shown in Fig. 2.4(a). It is possible for the moments at lattice site 1 and 2 to align antiparallel, but the moment at lattice site 3 cannot be placed exactly anti-parallel to the other two. Instead, spins will realize a 120° coplanar configuration in order to minimize the energy of the whole triangle as displayed in Fig. 2.4(b).

To generalize this to lattices containing elementary plaquettes (triangles, squares . . .), Toulouse [Toulouse77] proposed a criterion on the product of the bonds of a plaquette P:

$$P = \prod_{<i,j>} sign(J_{ij}) .$$

(2.3)

If $P < 0$, the plaquette is geometrically frustrated. For example, if we consider only antiferromagnetic couplings, examples of geometrically frustrated two-dimensional systems are the triangular lattice, the Kagomé lattice, the checkerboard lattice and the Shastry-Sutherland lattice. The square lattice, with an even number of antiferromagnetic couplings per plaquette, fails Toulouse's criterion. However, a square plaquette with three ferromagnetic bonds and one antiferromagnetic bond becomes frustrated.
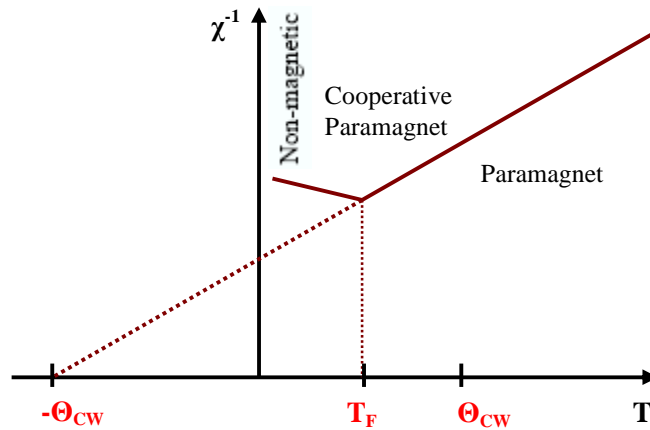

Figure 2.5 *Schematic curve of the inverse of the susceptibility χ as a function of temperature showing the signature of geometrical frustration (adapted from Ref. [Moessner01]). θ_{CW} is the Curie-Weiss temperature and T_F is the temperature of deviation.*

If we consider a whole lattice of N spins, the number of degrees of freedom increases with the number of bonds q in a single plaquette (for example, $q = 3$ if the plaquette is a triangle). The classical ground states satisfy $\mathbf{L} = 0$ in each plaquette. This condition leads to $n = 3$ constraints for Heisenberg spins. The dimension of the ground state grows with q and n. If we call F the number of degrees of freedom and K the number of constraints, the dimension of the ground state D is [Moessner01, Chalker07]:

$$D = F - K = \frac{N(n(q-w)-q)}{2} .$$

Hence the ground state of geometrically frustrated systems is highly degenerated and its dimension increases with the number of bonds per plaquette and the number of spin components. Quantum or thermal fluctuations can partially lift this degeneracy, which is called the *Order by Disorder* effect [Villain80].

Experimentally, strong frustration can be identified from the behavior of the inverse of the susceptibility χ^{-1}. Fig. 2.5 shows a schematic curve of a strongly frustrated magnet. The usual paramagnetic regime takes place above the Curie-Weiss temperature θ_{CW}. Between θ_{CW} and T_F, strongly frustrated systems then present a phase in which correlations are weak (cooperative paramagnet region). A deviation takes place at a temperature $T_F \sim \theta_{CW}$ indicating a transition to a non-generic state which varies from one compound to another [Moessner01]. The ratio $T_F / \theta_{CW} << 1$ is considered as a characteristic of strong frustration.

2.1.4 Effects of applied field on S = 1/2 Heisenberg antiferromagnets

A finite magnetic field orients spins towards the field direction, thus breaking the planar spin alignment, which may be the ground state at zero field. In this sense, the presence of an external magnetic field can be viewed as a competing interaction, which can affect quantum fluctuations. Moreover, a magnetic field gives the possibility to tune the ground state and move the spin system towards a quantum critical point. Here we will discuss effects of a magnetic field applied to some classical spin system.

a) Magnetization plateau

For classical spin systems, Misguish showed under the assumption that the classical energy is a continuous and differentiable function of the spins' directions [Misguich04], that the spin

configurations in the plateau *must be collinear* with the magnetic field direction. Let *n* be the number of spins in the unit cell and *p* an integer. The possible configurations are:

$$U^{n-p}D^p$$

where *n-p* is the number of spins 'Up' (*U*) and *p* of spins 'Down' (*D*). The corresponding magnetization plateau arises at:

$$\frac{M}{M_{sat}} = 1 - 2\frac{p}{n}.$$

For example, the magnetization as function of applied magnetic field for the $S = 1/2$ HAF on a triangular lattice is shown in Fig 2.6 [Farnell09]. The spin configuration in the plateau at 1/3 of the saturation magnetization M_{sat} is the collinear "Up-Up-Down" state (*UUD*), in which two out of three spins are pointing up along the *z*-axis and the last one is pointing down. Classical plateau states can sometimes survive in quantum-spin systems. Affleck and Hida [Hida05] studied the competition of two possible states in the 1/3 magnetization plateau of an $S = 1/2$ frustrated Heisenberg spin chain using bosonization, renormalization group and numerical diagonalization methods. Depending on the exchange modulation, the $M/M_{sat} = 1/3$ *classical* or *quantum* plateau state is favored.
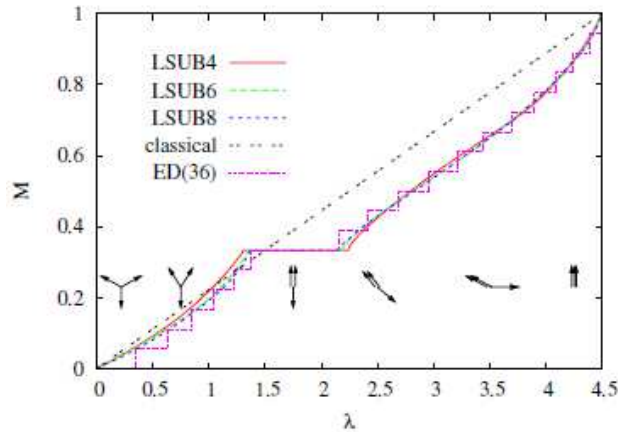

Figure 2.6 *Magnetization of the S = 1/2 HAF on a triangular lattice in the presence of an external magnetic field (Reprinted from Ref. [Farnell09]).*

The classical 1/3 plateau state, which appears in the conventional $S = 1/2$ frustrated Heisenberg chain

$$H_\partial = J \sum_i^L S_i S_{i+1} + \partial S_i S_{i+2} \tag{2.4}$$

consists in a 3-fold degenerate ↑↓↑ structure (i.e. the quantum analog of the classical collinear *UUD* configuration) accompanied by the spontaneous *Z3* translational symmetry breakdown [Farnell09].

The quantum case corresponds to •–• ↑ (where •–• is a singlet dimer). This state is favored by a period-exchange modulation:

$$H_\partial = J \sum_i^{L/3} \left[(1-\alpha)(S_{3l-1} S_{3l} + \partial S_{3l} S_{3l+1}) + (1+\alpha) S_{3l+1} S_{3l+2} \right]. \tag{2.5}$$

b) *Quantum phase transitions*

A classical phase transition (CPT) involves thermal fluctuations occurring at finite temperatures only. In the thermodynamic limit at $T = 0$ K, where the thermal energy scale is absent, only the fluctuations associated with the Heisenberg's uncertainty principle are present. In some cases those zero-point fluctuations lead to transitions which, in analogy to a CPT, are called a quantum phase transition (QPT) and occur at $T = 0$ K. In analogy with a temperature-driven CPT, every QPT is governed by an external parameter, for instance magnetic field, pressure or a doping percentage of a chemical [Vojta03].

A system approaches a quantum-critical point (QCP) in the thermodynamic limit under application of the external parameter. Every continuous QPT is characterized by an order parameter: At zero in the disordered phase, an order parameter becomes non-zero while the system reaches a QCP. Correlations of the order parameter diverge as $|\xi| \sim |\tau|^{-\nu}$ in the vicinity of QCP. Here τ is a measure of closeness to the QCP and ν is the correlation length critical exponent. An order parameter fluctuates not only in space but also in time. Close to the QCP corresponding time correlations τ_c diverges as $\tau_c \sim |\tau|^{-\nu z}$, where z is the dynamical critical exponent [Sachdev99].

Critical length and time scales are the only characteristics of the system close to QCP. All scaling observable variables' critical exponents depend on ξ and τ_c exclusively. Therefore the scaling is universal and depends only on the symmetry of the order parameter. Consequently, QPTs can be classified by the symmetry of order parameter which forms the universality class. It means that all observable variables in various QPTs posses a universal behavior which can be described by a model system with a corresponding symmetry of the order parameter [Vojta03, Sachdev99].

Quantum-ordered phases occurring at $T = 0$ K survive to a finite temperature range, which is important for experimental physics. This makes empirical investigations of QPTs possible. A wide range of QPTs was discovered: from superfluid helium and the cuprate superconductors, which can be tuned from a Mott insulating to a superconducting phase by a carrier doping [Keimer91, Aeppli97], to various QPTs in quantum magnets and unconventional metals [Schröder00]. The main role in the phenomena is played by electrons and their collective behavior. Quantum magnets, i.e. systems with localized electrons in reduced dimensions, belong to the most important candidates for the investigations of novel quantum phases. In the next section 1.2.1(c), a specific example of a QPT in a low-dimensional magnet is given: Bose-Einstein condensation of magnons.

c) *Bose-Einstein condensation of magnons*

Bose-Einstein condensation (BEC) remains one of the most exotic predictions of quantum mechanics. In the last half decade, a continuous interest has been shown with respect to this phenomenon because of its experimental evidence in ultra-cold diluted atomic gases. It is also known that a quantum spin system can be mapped onto an interacting Bose gas. The analogy between a quantum spin system which presents long-range order, and an interacting Bose gas, which presents BEC, has been well known for a long time [Matsubara56].

Here we show that field-induced QPTs from paramagnetic to the 3D-XY ordered antiferromagnetic phase can be mapped onto Bose-Einstein condensation of magnons (BEC) in axially symmetric magnets. The materials of choice have been crystalline networks of antiferromagnetically coupled $S = 1/2$ dimers. The starting point is the spin Hamiltonian of the system, which, for instance, in case of the ladder models with rungs made of spin-1/2 dimers [Oosawa99, Rüegg03], can be written as:

$$\tilde{H} = J_{rung} \sum_{rung} S_{1,rung} S_{2,rung} + J_{leg} \sum_{i,j} S_i S_j - g\mu_B H \sum_k S_k^z . \tag{2.6}$$

Here the first sum is taken over all rungs in the spin ladder, the second sum runs over all legs and the third term describes the impact of the magnetic field H and its sum runs over all spins in the system. We assume that the rung exchange interaction, J_{rung}, is the strongest in Eq. 2.6, coupling S_1 and S_2 into dimers. Thus the system effectively consists of interacting $S = 1$ particles. Using second-order quantization, it was shown [Nikuni00, Giamarchi99] that the Hamiltonian in Eq. 2.6 can be mapped onto the following form:

$$\tilde{H} = \sum_i \left(J_{rung} - g\mu_B H \right) a_i^+ a_i + \sum_{i,j} t_{ij} a_i^+ a_i + \frac{1}{2} \sum_{i,j} U_{ij} a_i^+ a_j^+ a_i a_j \qquad (2.7)$$

where the operators a_i^+ and a_i create and annihilate a boson on dimer i, respectively, t_{ij} describes a hopping between sites i and j and U_{ij} is a repulsion energy. The coupling of the transverse, $S_i^x S_j^x + S_i^y S_j^y$, and longitudinal, $S_i^z S_j^z$, components in the spin Hamiltonian in Eq. 2.6 maps onto the hopping t_{ij} and repulsion U_{ij} terms in the bosonic representation in Eq. 2.7, respectively. The singlet $S = 0$ is the ground state of the system and is separated by a finite energy gap Δ from the excited triplet $S^z = 0; \pm 1$. An applied magnetic field induces the Zeeman splitting and lowers the energy of the dispersive $S^z = 1$ excitation. When the field energy is equal to the value of the gap, $g\mu_B H_{c1} = \Delta$, the excitation $S^z = 1$ mixes with the ground state and the system undergoes a QPT from quantum paramagnetic to the 3D antiferromagnetically ordered state. In the bosonic representation, this process can be viewed as a condensation of magnons carrying $S = 1$, thus obeying Bose-Einstein statistics [Sorensen93]. In spin space, the field-induced Bose-Einstein condensation (BEC) of magnons corresponds to the order of the transverse spin components, perpendicular to the applied field, which spontaneously breaks the *O(2)* symmetry of the Hamiltonian in Eq. 2.6. The list of the respective parameters of the Bose gas and the quantum antiferromagnet is given in Tab. 2.1 [Giamarchi08].

Table 2.1 *The respective parameters of a Bose gas and a quantum antiferromagnet. The table is adapted from the review of T. Giamarchi et al. [Giamarchi08].*

Bose gas	Antiferromagnet
Particles	Magnons carrying spin-1
Boson number N	Spin component S^z
Charge conservation U(1)	Rotational invariance O(2)
Condensate wavefunction $\psi_i(r)$	Transverse order ($S_i^x + iS_i^y$)
Chemical potential	Magnetic field

The upper critical dimension d_c and the dynamical exponent z of the BEC are equal to two. However the magnetically quantum-ordered phase exists at finite temperature and its dimension is $d > 2$. Therefore, the experimentally observed field-induced phase transition in the low-temperature

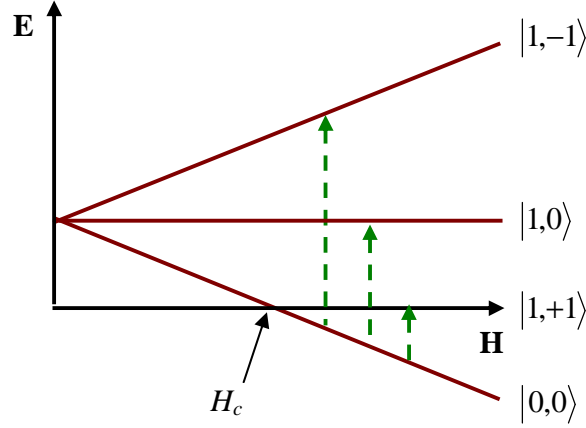region, corresponding to the BEC of magnons, belongs to the 3D-XY universality class with $d = 3$ and $z = 2$.

Figure 2.7: *The schematic representation of the field-driven Bose-Einstein condensation of magnons (adapted from Ref. [Rüegg03]).*

The process of the field-induced antiferromagnetic order was observed experimentally in the gapped $S = 1/2$ compound TlCuCl$_3$ by Oosawa *et al*. [Oosawa99] and explained as the BEC of magnons by Nikuni *et al*. [Nikuni00]. The magnetization measurements [Oosawa99], [Shiramura97] have shown that the magnetic subsystem of TlCuCl$_3$ consists of weakly antiferromagnetically coupled $S = 1/2$ spin dimers and the first excited state is separated from the ground state singlet by the energy gap $\Delta = 0.7$meV. At the quantum-critical point, which corresponds to the critical magnetic field $H_c = 5.7$ T, the energy gap collapses. The diagram of the field-induced QPT from a magnetically disordered towards a 3D XY antiferromagnetic state is shown in Fig. 2.7. The solid lines correspond to the Zeeman splitting of the excited triplet state. At the quantum-critical point, the triplet mode $S^z = +1$ reaches the nonmagnetic ground state $S^z = 0$ and the system turns into a 3D antiferromagnetic state, which is proved by the detected Goldstone mode [Rüegg03].

2.2 Physical acoustic properties

2.2.1 Elastic theory

Let us begin with a survey of continuum elastic theory. Only the main results will be presented. The proper derivation and the full development of the theory can be found in various monographs, such as [Landau59] or [Kittel05].

When an elastic deformation is applied to a medium, a point originally at R moves to $R' = R + u(R, t)$. Obviously, the effect of a constant u is just a translation of the whole medium. For deformations, u is position dependent and we can express dR' by the partial derivatives:

$$v_{ij} = \frac{\partial u_i}{\partial R_j}, \text{ i.e. } dR_i^{'} = dR_i + \sum_j v_{ij} dR_j .$$

Here v_{ij} is a component of the deformation tensor. A general deformation in a solid can be built up by a pure strain deformation followed by a rotation. Usually, only infinitesimal displacements are considered in the elasticity theory. Therefore, a component of the infinitesimal strain tensor reads: $\varepsilon_{ij} = \frac{1}{2}(v_{ij} + v_{ji})$ and the rotation tensor R reduces to $R_{ij} = \delta_{ij} + \omega_{ij}$, where $\omega_{ij} = 1/2(v_{ij} - v_{ji}) = -\omega_{ji}$. The ω_{ij} are the components of a vector $\Omega = 1/2 \text{ rot} u = (\omega_{yz}, \omega_{zx}, \omega_{xy})$ which describes a bulk rotation of the body in first order for a homogeneous deformation. So the finite strain tensor can be written as:

$$\eta_{ij} = \varepsilon_{ij} + \frac{1}{2}\sum_k (\varepsilon_{ki} + \omega_{ki})(\varepsilon_{kj} + \omega_{kj}).$$

Applying Hook's law to a continuous elastic medium, we obtain the equations of motion:

$$\rho \frac{\partial^2 u_i}{\partial t^2} = \sum_k \frac{\partial T_{ik}}{\partial R_k}.$$

Here T_{ik} is a component of the stress tensor and u the displacement vector introduced above. With the linearized stress-strain relation, which is the phenomenological Hooke law:

$$T_{ij} = \sum_{kl} c_{ijkl} v_{kl}$$

and for plane waves $u_i = Ue_i\exp(i(k\cdot r - \omega t))$ (U amplitude, e polarization vector) we get the eigenfrequencies and normal modes:

$$\sum_{jlm} \left[\rho \omega_k^2 \delta_{il} - c_{ijlm}k_m k_j \right] e_l(k) = 0.$$

Here ω_k is the eigenfrequency for the wave vector k and c_{ijkl} are the elastic stiffness constants. The components of the inverse tensor to the (c_{ijkl}) are denoted by s_{ijkl}, the components of the compliance tensor.

2.2.2 Background elastic constant

In the harmonic approximation without phonon-phonon interaction, the elastic constants are temperature independent. In the harmonic approximation, the Hamiltonian H_h has terms due to strains and due to harmonic phonons:

$$\mathrm{H}_h = \mathrm{H}_{el} + \mathrm{H}_{ph} = \frac{1}{2}\sum_\Gamma c^0_\Gamma \varepsilon^2_\Gamma + \frac{1}{2}\sum_q \hbar\omega_q\left(n_q + \frac{1}{2}\right) \tag{2.8}$$

where c^0_Γ is a symmetry elastic constant and $\mathrm{n}_q = (\exp(\hbar\omega_q/kT)-1)^{-1}$ is the thermal occupation number of the phonon q. The lowest-order an-harmonic theory starts with a quasi-harmonic free energy with $n_q = 0, 1, 2\ldots$

$$F_{qh} = F_0 - kBT\,\ln Z$$

$$= F_0 + KT\sum_q \ln\left[2\sinh\left(\frac{\hbar\omega_q}{2k_BT}\right)\right] \tag{2.9}$$

where F_0 is the elastic energy H_{el}. But now H_{el} and ω_q depend on R_i, the lattice vectors. For equilibrium we have $\partial F_{qh}/\partial\varepsilon_{ij} = 0$, i.e.

$$c^0_{ij}\varepsilon_{ij} + \frac{1}{2}\sum_q \frac{1}{\omega_q}\frac{\partial\omega_q}{\partial\varepsilon_{ij}}E(\omega,T) = 0 \ \text{ with } \ E = \hbar\omega(n+\frac{1}{2}) .$$

$E(\omega)$ is the average energy of an oscillator. Due to the third- and fourth-order anharmonic terms in the crystal potential, there is a coupling between the homogeneous strains and the phonons. This an-harmonicity can be described by the strain dependence of the phonon frequencies via the phonon Grüneisen parameter:

$$\gamma_{kl} = \frac{\partial\ln<\omega^2>}{\partial\varepsilon_{kl}}, \ \Gamma_{klk'l'} = -\frac{\partial^2\ln<\omega^2>}{\partial\varepsilon_{kl}\partial\varepsilon_{k'l'}} .$$

From the above equations with:

$$c_{ij} = c^0_{ij} + \frac{1}{2}\frac{\partial}{\partial\varepsilon_{ij}}\sum_q \frac{1}{\omega_q}\frac{\partial\omega_q}{\partial\varepsilon_{ij}}E(\omega,T) \tag{2.10}$$

$$c_{ij} = c^0_{ij} - \frac{1}{2}\Gamma U(T) + \frac{1}{4}\gamma_{ph}\left[U(T) - TC_V(T)\right]. \tag{2.10a}$$

For $T > \Theta_D$, c_{ij} is proportional to T since $U \approx T$, they reach a constant value at $T = 0$ and for low temperatures c_{ij} is proportional to T^4 ($C \approx T^3$, $U \approx T^4$). Fig. 2.8 shows a typical result for $c_{ij}(T)$ for cubic LaAl$_2$ [Schiltz74]. With $\Theta_D = 374$ K, a linear temperature dependence already for $T > 150$ K is observed, i.e. for $T > \Theta/2$ for all elastic modes and a bend over ($\sim T^4$) towards saturation for $T < 100$ K.
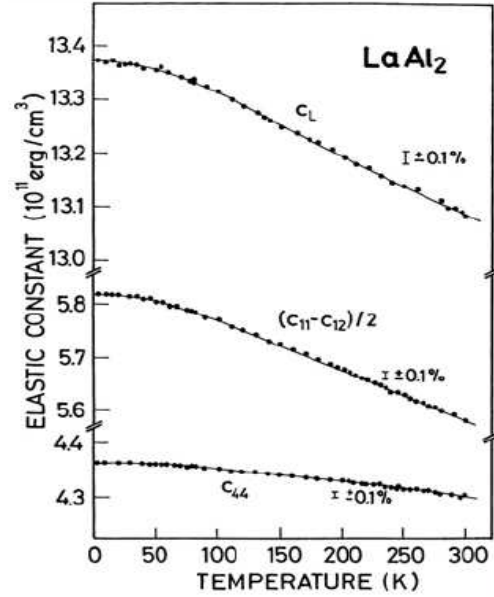
Figure 2.8 *Temperature dependence of elastic constants for LaAl$_2$ (reprinted from Ref. [Schiltz74]).*

The range of the T^4 dependence of the elastic stiffness constants is difficult to estimate. There are phenomenological expressions for the temperature dependence of the elastic constants, the best known is given by Varshny [Varshny70]. It reads:

$$c_{ij} = c_{ij}^0 - \frac{s}{e^{t/T} - 1} \tag{2.11}$$

where s and t are constants which can be fitted to the experimental results. This empirical expression for the temperature dependence due to anharmonic phonon interaction describes the background elastic stiffness constants surprisingly well. It is therefore widely used.

2.2.3 Magnetic susceptibility and elastic constants

Here we discuss magnetic susceptibility and elastic constants for crystals with magnetic ions in the presence of crystalline electric fields (CEF). First, we discuss systems where other effects such

as magnetic exchange interactions or quadrupolar interactions between the magnetic ions are negligible. After that the more complicated effects will be introduced.

The necessary formula for the different thermodynamic derivatives, the free energy density of the system, can be written as:

$$F = F_{qh} + F_{CEF} = F_{qh} - N_s k_B T \sum_n e^{-\frac{E_n(\varepsilon_\Gamma)}{k_B T}} \tag{2.12}$$

where F_{qh} is the background free energy density of the quasi-harmonic crystal and the crystal field free energy density is given by $F_{CEF} = -N_s k_B T \ln Z$ with Z the partition function. The energies E_n are strain-dependent. N_s is the number of magnetic ions per unit volume. The CEF magnetic susceptibility χ_m measures the response of a system of magnetic ions to an applied magnetic field B

$$\chi_m = N_s \frac{\partial \langle J_z \rangle}{\partial B} = -\frac{\partial^2 F}{\partial B^2} = -N_s \left\{ < \frac{\partial^2 E}{\partial B^2} > -\frac{1}{k_B T} < \left(\frac{\partial E}{\partial B} \right)^2 > +\frac{1}{k_B T} < \frac{\partial E}{\partial B} >^2 \right\}. \tag{2.13}$$

In this expression the first term is a Van Vleck contribution, which probes the off-diagonal magnetic dipole matrix elements. The next two terms are the so-called Curie terms showing a strong temperature dependence that is due to the diagonal matrix elements.

In an analogous way, the strain susceptibility is the response of the structural order parameter $<O_\Gamma>$ to an applied strain ε_Γ. The strain dependence of the CEF energy levels in second-order perturbation theory is obtained from the magneto-elastic interaction:

$$E_n(\varepsilon_\Gamma) = E_n - g_\Gamma \varepsilon_\Gamma < n|O_\Gamma|n > + g_\Gamma^2 \varepsilon_\Gamma^2 \sum_{n \neq m} \frac{|< n|O_\Gamma|n >|^2}{E_n - E_m} \tag{2.14}$$

where E_n are the unperturbed CEF energies. This perturbation theory is appropriate for small strains as used in ultrasonic measurements. This gives for the elastic constant:

$$\Delta c_\Gamma = c_\Gamma(T) - c_\Gamma^0(T)$$

$$\Delta c_\Gamma = \frac{\partial < O_\Gamma >}{\partial \varepsilon_\Gamma} = \frac{\partial^2 F}{\partial \varepsilon_\Gamma^2} = -g_\Gamma^2 \chi_\Gamma^{str} \tag{2.15}$$

$$= N \left\{ < \frac{\partial^2 E}{\partial \varepsilon_\Gamma^2} > -\frac{1}{k_B T} < \left(\frac{\partial E}{\partial \varepsilon_\Gamma} \right)^2 > +\frac{1}{k_B T} < \frac{\partial E}{\partial \varepsilon_\Gamma} >^2 \right\}. \tag{2.15a}$$

Eq. 2.15a can be interpreted in the same way as Eq. 2.13. c_Γ^0 is the background elastic constant. We can distinguish again between Van Vleck type terms $\partial^2 E/\partial\varepsilon^2$ and the strongly temperature-dependent Curie term.

Now, if we include the exchange interaction: $H_{ex} = \sum_{i,j} J_{ij} S_i S_j$, the magnetic susceptibility changes from the single-ion susceptibility to:

$$\chi_m = \frac{\chi_0}{1 - j\chi_0}. \tag{2.16}$$

Here, j is the $q = 0$ exchange constant which has positive and negative values for ferromagnets and antiferromagnets, respectively.

In a similar way, an expression for the elastic constants in the presence of two-ion interactions can be obtained. The Hamiltonian is taken as:

$$H = c_\Gamma \frac{\varepsilon_\Gamma^2}{2} + g_\Gamma \varepsilon_\Gamma \sum_i O_{\Gamma_i} + K \sum_{i \neq j} O_{\Gamma_i} O_{\Gamma_j}. \tag{2.17}$$

Here, the first and second terms are the elastic and magneto-elastic energy. The last term gives the orbital interactions between the quadrupoles with a coupling constant K. Eq. 2.17 in molecular-field approximation reads:

$$H = c_\Gamma \frac{\varepsilon_\Gamma^2}{2} + g_\Gamma \varepsilon_\Gamma \sum_i O_{\Gamma_i} + K <O_\Gamma> \sum_{i \neq j} O_{\Gamma_i} = c_\Gamma \frac{\varepsilon_\Gamma^2}{2} + \zeta \sum_i O_{\Gamma_i} \tag{2.18}$$

with $\zeta = g\varepsilon + K<O_\Gamma>$. For the free energy we get in the molecular field approximation:

$$H = c_\Gamma \frac{\varepsilon_\Gamma^2}{2} + KN_s \frac{<O_\Gamma>^2}{2} - k_B T \ln \sum_i e^{-\frac{E_i}{k_B T}}. \tag{2.19}$$

Here the magnetic ion energies E_i depend on ζ as $E_i = E_i^0 + a_i\zeta + b_i\zeta^2$. We get the equilibrium condition $\partial F/\partial<O_\Gamma> = K<O_\Gamma> + <\partial E/\partial<O_\Gamma>> = 0$. With the single-ion strain susceptibility $\chi_s = d<O_\Gamma>/d\varepsilon$ we get $d\zeta/d\varepsilon = g/(1 - K\chi_s)$ and $c_\Gamma = d^2F/d\varepsilon^2 = c^0 - gN_s\chi_s d\zeta/d\varepsilon$ or:

$$c_\Gamma = c_\Gamma^0 - g^2 N_s \chi_{str} \text{ with } \chi_{str} = \frac{\chi_s}{1 - K\chi_s}. \tag{2.20}$$

This equation has the same structure as the magnetic susceptibility in Eq. 2.16. The expression has wide-spread applications in various fields such as in the cooperative Jahn–Teller effect [Lüthi05], certain structural transitions and the magnetic dimer–strain coupling [Wolf01a].

2.2.4 Ultrasonics at magnetic phase transitions

The exchange interaction is the dominant interaction responsible for a magnetic phase transition. The isotropic Heisenberg exchange interaction explains many different phenomena in magnetism, such as the occurrence of the phase transition or the elementary excitations called magnons or spin waves. The magneto-elastic interaction, i.e. the coupling of the lattice coordinates (strains or phonon coordinates) to the spin system plays only a secondary role. Here, we will discuss the effect of the strain-spin coupling on the sound velocity and the attenuation near magnetic phase transitions.

a) Critical attenuation coefficient

Critical effects on sound velocity and attenuation are expected because of the spin–phonon coupling, especially the exchange striction coupling. With this interaction, energy is transferred from the sound wave to the spin system, which has relaxation channels whose relaxation times can diverge at the critical temperature. Hence from the strain-order parameter coupling (discussed detail in [Lüthi05]), it is seen that the sound attenuation α can diverge for $\omega\tau < 1$ and dispersive effects can occur for $\omega\tau << 1$, cf. Fig. 2.9.

The relaxation time τ measures the time the system needs to come from a non-equilibrium state to the thermodynamic equilibrium. This parameter diverges upon approaching the critical point, with the critical slowing down. This is the source of divergencies in transport coefficients, here the ultrasonic attenuation. The attenuation coefficient can be determined by calculating the number of phonons with wave vector q absorbed minus those (induced) emitted [Stern65] leading to time-dependent four-spin correlation functions:

$$\alpha = \sum_{ij\delta\delta'} b(\delta,\delta',q) \int_0^\infty dt e^{i\omega t} e^{iq(R_i - R_j)} < S_i(0) S_{i+\delta}(0) S_j(t) S_{j+\delta'}(t) > \qquad (2.21)$$

with $b = \left(\dfrac{1}{\delta} \dfrac{\partial J}{\partial \delta} \right)^2 (\delta \cdot e_q)(\delta' \cdot e_q)(\delta \cdot q)(\delta' \cdot q)(1 - e^{h\omega/kT})(2eMh\omega)^{-1}$.

31

In this formula, the attenuation coefficient α is proportional to the space-time Fourier-Laplace transform of a four–spin correlation function. For the evaluation of this correlation function, the different theories can be divided into three groups: the so-called conventional theories, the mode–mode coupling theories and the coupling to energy fluctuations.
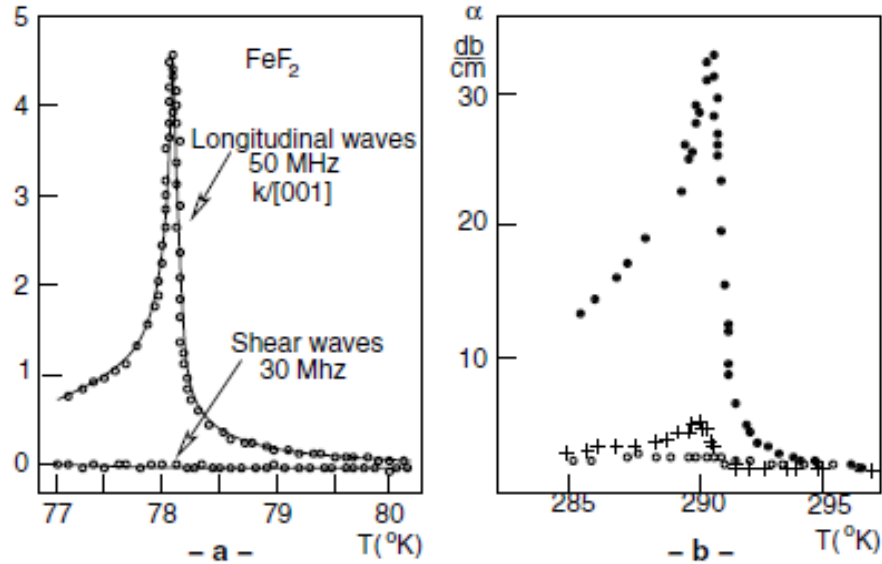

Figure 2.9 *Ultrasonic attenuation of longitudinal and shear waves along the c-axis near T_N and T_C for (a) FeF$_2$ (reprinted from Ref. [Ikushima71]), (b) Gd (reprinted from Ref. [Lüthi68]) (full circles correspond to longitudinal, crosses and open circles to shear waves).*

Conventional theories: The four–spin correlation function of Eq. 2.21 is first factorised. In the next step, the hydrodynamic form is used for the two–spin correlation function: $<S_k S_{-k}(t)> = <S_k S_{-k}> e^{-t/\tau}{}_k$ which is valid only for $k\xi <<1$ with ξ the correlation length of spin fluctuations and τ_k the characteristic decay time of the spin fluctuations. Finally with $\omega << \tau_k^{-1}$ the attenuation becomes

$$\alpha \sim \omega^2 \chi^{1/2} \tau_c \tag{2.22}$$

where χ is the spin susceptibility and $\tau_c = \tau_{k<1/\xi}$. ω^2 originates from the linear q dependence of Eq. 2.21. Eq. 2.22 indicates that the critical slowing down of the spin fluctuations, $1/\tau_c$, enhances the singularity in the attenuation α on approaching T_C.

Mode–mode coupling theories: In the above discussion, the conventional theories overestimate the effect of correlations. This can be shown, for example, by calculating the specific heat using the

32

factorization approximation, which gives $C \sim \chi^{1/2}$. In fact as pointed out by Bennett [Bennett69a], if, correspondingly, $\chi^{1/2}$ is replaced by C in Eq. 2.22, then

$$\alpha_S \approx \frac{\omega^2 C \tau_C}{1 + \omega^2 \tau_C^2} .$$

(2.23)

In these theories, one hydrodynamic mode decays into several hydrodynamic modes, leading to a divergence in the transport coefficients. These theories retain the assumption $\omega << \tau_c^{-1}$ and the hydrodynamic form of the spin fluctuations but do not factorize the four–spin correlation function of Eq. 2.21.

Energy-density coupling: Finally, we discuss the energy density coupling mechanism. An important variant of the theories outlined above occurs if the exchange striction Hamiltonian H_{exs} is proportional to the exchange Hamiltonian, i.e. if in the corresponding expressions

$$H_{exs} = \sum_i A e^{iqR_i} z_i' b_i (S_0 \cdot S_{R_i}) \text{ and } H_{ex} = \sum_i z_i J_i S_0 S_{R_i} .$$

(2.24)

Each individual term of H_{exs} is proportional to the corresponding term in H_{ex}. Here A is the amplitude of the sound wave, z_i is the number of neighbors (R_i) for a given site. z_i' is generally different from z_i, i.e. the sound wave couples in general only to part of the spin energy density. Then the attenuation is proportional to an energy correlation function instead of the four-spin correlation function discussed above

$$\alpha_E \propto \omega^2 \int_0^\infty dt e^{i\omega t} < E_q E_{-q}(t) > .$$

(2.25)

Here $<E_q E_{-q}(t)> = <E_q E_{-q}>e^{-t/\tau_{sl}}$ with $\tau_{sl}^{-1} = \gamma/C_m$ the spin-lattice relaxation time of the spin-energy density with γ a constant. The evaluation of Eq. 2.22 gives the same expression as for α_S (2.24) but with a weaker singularity like C_M for τ_{sl}. Another relaxation channel via energy diffusion $\tau_E^{-1} = \kappa q^2/C_M$, with κ the thermal conductivity, is less effective. This coupling to energy fluctuations was introduced by Lüthi and Pollina [Lüthi69].

b) *Sound velocity effects near magnetic phase transitions*

Similar to the critical ultrasonic attenuation, sound velocities also exhibit sharp dips at the magnetic phase transitions. An example of sound velocities for MnF_2 near T_N for different propagation directions [Kawasaki70] is shown in Fig. 2.10. The anomalies amount to $\Delta v/v_0 \leq 1/2\%$.

Experimentally, both quantities are usually measured together. As introduced in Sec. 2.2.1, for $\omega\tau$ << 1 the sound velocity does not depend on the relaxation time τ and therefore it is not a transport coefficient in contrast to the attenuation. It is a thermodynamic quantity and it can be calculated by the static part of the spin fluctuations.
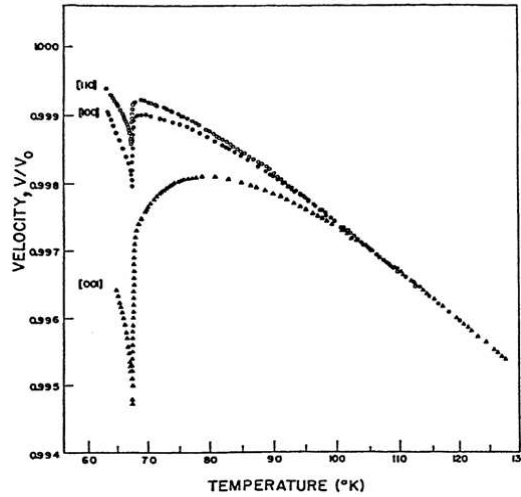
Figure 2.10 *Anomalous temperature dependence of the velocity of 10MHz longitudinal sound in MnF₂ for three different directions (reprinted from Ref. [Kawasaki70]).*

To get a feeling for the velocity anomaly, consider a magnetic free energy of the form $F_m = -Tf(T/T_c)$. The spin–phonon coupling is of the exchange-striction type and the coupling constant is given by $dT_C/d\varepsilon$ and the longitudinal elastic constant is $c = c_0 + \mathrm{d}^2F_m/\mathrm{d}\varepsilon^2 = c_0 - (\mathrm{d}T_c/\mathrm{d}\varepsilon)^2(T/T_c)C_V$ with the magnetic specific heat $C_V = -T\mathrm{d}^2F_m/\mathrm{d}T^2$. Therefore we expect only a small divergence in the sound velocity, the same as the specific heat divergence and with no frequency dependence.

$$\frac{\Delta v}{v_0} \approx -\omega^0(T-T_N)^{-\varsigma}.$$

3

EXPERIMETAL TECHNIQUE AND ANALYSIS

This chapter describes the experimental technique and the data-analysis procedure. The experiments are divided into two parts. The first part presents an overview of the method employed to perform ultrasonic measurements and a short note is given about the cryomagnetic systems which are used to perform measurements at low temperature. The second part discusses the system and method that was used to study the magnetic properties of the materials investigated in this thesis.

3.1 Ultrasonic measurements

The common method we use to measure the elastic constants is determined from the propagation of acoustic waves. Sound waves are generated and detected by transducers attached to the plane faces of the specimen which are ideally parallel to each other. The most widely used methods to measure sound velocity and attenuation are the pulse-echo technique and the shape resonance technique, also called resonant ultrasound spectroscopy (RUS). In the latter case the specimen acts as a resonator operated at one of its eigenmodes so its quality is strongly related to the acoustic attenuation of the specimen. Most specimens of interest exhibit rather large attenuation leading to very low resonator quality. Therefore the pulse-echo excitation method [Lüthi94] has been chosen and successfully setup in our lab and is presented in detail below.

3.1.1 Pulse-echo technique and phase-comparative method

The basic idea of the pulse-echo technique is to send a pulse of sound through a sample. Assuming the input pulse signal $A_1 = A_0cos(\omega t)$ is applied to a transducer which emits a radio frequency acoustic wave (sound) into the sample, the sound wave propagates in the sample with velocity v_s and arrives at the second transducer after a time $\tau = L/v_s$, L being the length of the sample. The transducer detects a signal $B = B_0cos[\omega(t-\tau)]$ which is delayed by the propagation time τ and reduced in amplitude by a factor A_0/B_0 as illustrated in Fig. 3.1. Due to acoustic impedance mismatch at the interface between sample and transducer (or bond) part of the acoustic wave is reflected and propagates back to the first transducer. There it is reflected again and after a total time

$\tau_3 = 3L/v_s$ it arrives again at the second transducer. This process is repeated producing a detected pulse train where each transit gives a phase shift for the signal of $\Phi_n = (2n+1)\omega L/v_s$ (n = 0, 1, 2…).
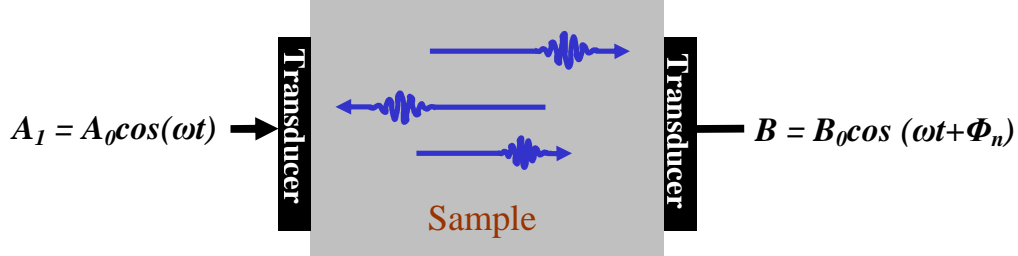

Figure 3.1 Schematics of sound pulse traveling inside the sample.

By taking the total differential of sound velocity $v_s = (2n+1)\omega L/\Phi_n$ we have:

$$dv_s = (2n+1)\left[\frac{L}{\Phi_n}d\omega + \frac{\omega}{\Phi_n}dL - \frac{\omega L}{\Phi_n^2}d\Phi_n\right].$$

(3.1)

After division by v_s from Eq. 3.1, it reads:

$$\frac{dv_s}{v_s} = \frac{d\omega}{\omega} + \frac{dL}{L} - \frac{d\Phi}{\Phi}.$$

(3.2)

Partial integration gives:

$$\ln\left(\frac{v_s}{v_{s0}}\right) = \ln\left(\frac{\omega}{\omega_0}\right) + \ln\left(\frac{L}{L_0}\right) - \ln\left(\frac{\Phi}{\Phi_0}\right).$$

(3.3)

Here the index 0 denotes some constant initial value. Taking the exponential finally:

$$\frac{v_s}{v_{s0}} = \frac{\omega L \Phi_0}{\omega_0 L_0 \Phi}.$$

(3.4)

By replacing the entire variable in Eq. 3.4 as the initial value plus changing the form $x = x_0 + \Delta x$, performing multiplications and subtracting with the note that the higher-order products are negligible because the relative changes of $\frac{\Delta x}{x_0}$ have a magnitude of order 10^{-6} to 10^{-3}, one obtains:

$$\frac{\Delta v_s}{v_{s0}} = \frac{\Delta\omega}{\omega_0} + \frac{\Delta L}{L_0} - \frac{\Delta\Phi}{\Phi}.$$

(3.5)

Usually $\dfrac{\Delta L}{L_0}$ is neglected since it is mostly one or two orders less than $\dfrac{\Delta v_s}{v_{s0}}$. If this is not valid, it must be corrected by other measurements such as magnetostriction or thermal expansion. The Eq. 3.5 now contains two parameters ω and Φ to be determined in order to obtain the sound velocity v_s. Conveniently, the measurement is performed while keeping $\Delta\Phi = 0$ with the electronic setup as described in Sec. 3.1.2. So the change of frequency immediately gives the relative change of sound velocity

$$\frac{\Delta v_s}{v_{s0}} = \frac{\Delta\omega}{\omega_0}.\tag{3.6}$$

3.1.2 Electronic setup

Figure 3.2 shows the electronic part of the ultrasonic setup for the simultaneous detection of the relative changes of ultrasonic velocity and attenuation, based on the technique presented above. The frequency range of 5–500 MHz is covered and the duration of the ultrasonic echo pulse is 0.1–1 μs. The repetition rate depends on the available cooling power in the cryostat and lies between 100 Hz in the mK temperature range and a few kHz at higher temperatures.

(1) *The frequency generator* produces a signal $A_1 = A_0 cos(\omega t)$ with a frequency between 10–500 MHz, depending on the transducer.

(2) *The voltage divider* that divides the signal into two. One signal is sent through the sample and the other one for the reference.

(3) *The diode switch* that is used to create a radio-frequency pulse signal.

(4) *The pulse generator* that triggers *the diode switch*.

(5) *Power amplifier*: amplifies the signal before sending it to the sample.

(6) *Transducer*: converts the electronic signal to an ultrasonic signal and vice versa.

(7) *Sample*.

(8) *Receive amplifier*: amplifies the signal received from the sample and splits it into two channels.

(9) *Power amplifier*: amplifies the reference signal.

(10) *Quadrature hybrid*: Splits the reference signal into two equal amplitudes but 90° out of phase.
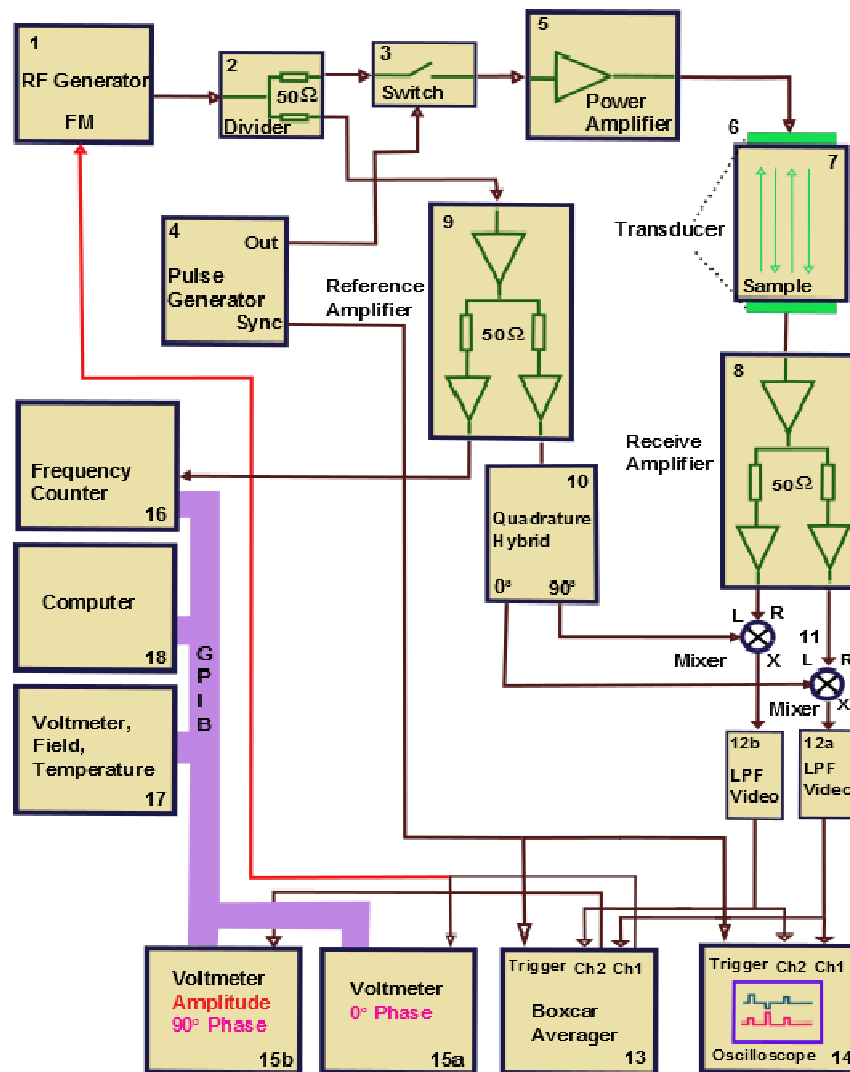
Figure 3.2 *Experimental setup for the measuring sound velocity and the attenuation (adapted from Ref. [Lüthi05]).*

(11) *Mixer*: multiplies each reference signal by one of the identically received signals from sample using for phase-sensitive detection.

$$A_1B = 1/2A_0B_0[cos\Phi_n + cos(2\omega t + \Phi_n)]$$

$$A_2B = 1/2A_0B_0[sin\Phi_n + sin(2\omega t + \Phi_n)]$$

(12) *Low-pass filter*: suppresses the time-dependent component leaving the time-independent one as the so-called phase signal.

In-Phase-signal: $I_n = 1/2A_0B_0 cos\Phi_n$ Quadrature-signal: $Q_n = 1/2A_0B_0 sin\Phi_n$

(13) *Boxcar averager*: Since the phase signal contains several echoes, *the boxcar averager* is used to select a particular one, performs some averaging both during each echo and between successive echoes and reads the output signal as the I_n and Q_n as mentioned above.

(14), (15), (16), (17) Oscilloscope and Voltmeters used to display the results.

(18) *Computer*: used to determine the frequency change and the amplitude of the 90° phase-shifted signal Q_n.

There is a direct feedback from the voltmeter to keep the phase of the signal I_n constant, usually equal to zero, by changing the frequency of the signal generator. As explained in Sec. 3.1.1 with the constant phase, the relative change of frequency $\dfrac{\Delta f}{f_0} = \dfrac{\Delta \omega}{\omega_0}$ gives directly $\dfrac{\Delta v_s}{v_{s0}}$ and is recorded by a frequency counter (16).

For the attenuation measurements, the principle way is to fit echo trains with an exponential function

$$A_n = A_0 e^{-\alpha(2n+1)L} \tag{3.7}$$

where α is the attenuation coefficient, *L* the sample length and n the number of the echo. Actually, the ultrasonic attenuation calculation is more difficult because the damping of the sound wave is not only due to the attenuation but also due to other sources such as reflection at boundaries between transducers, interference effects and so forth. Thus it is impossible to calculate the attenuation α from the Eq. (3.7) because in fact it is

$$A_n = z_n A_0 e^{-\alpha(2n+1)L}$$

with the unknown factor z_n due to the losses mentioned above. Under the assumption that the value of this unknown factor remains constant during the experiment, the ratio $\dfrac{A_n}{A_{n0}} = e^{-(\alpha - \alpha_0)(2n+1)L}$ will give the attenuation change.

We set and kept $Q_n \sim 0$ to determine the change in the sound velocity, so that I_n of the corresponding echo has its maximum value. Setting a second boxcar gate again at the position of the *n*th echo to record I_n, we obtain information about the changes of its amplitude so the relative ultrasound attenuation Δα can be easily calculated.

3.1.3 Sample

To use this technique, the pulses need to be long enough to include at least a few cycles of the frequency. With frequencies around 100 MHz, this implies that 10 cycles are included in a pulse length of 1μs. A pulse that is too short will not provide a clean excitation at the reference frequency. This restriction on the pulse length is then translated into a restriction in the sample length (L). This is because the echoes need to be separated into distinct pulses so the travel time ($\tau = L/v_s$) through the sample must be longer than the pulse length (T_{pulse})

$$T_{pulse} < \tau = L/v_s.$$

Because sound velocities are of the order of 10^3 m/s, and assuming the pulse length of 1 μs, this would imply a requirement for the sample length to be in the millimeter range.

It is also necessary to have the two surfaces, where the sound should bounce, to be as parallel and as flat as possible. The flatness requirement is to insure a good reflection (like in a mirror) at the surface of the sample. For this purpose, the surface roughness must be smaller than the wavelength of the sound. If the polishing is not good enough, the sound waves will suffer a diffuse scattering, so that a large fraction of the signal will not come back along the incoming direction and will be seen as a source of attenuation.

Besides that the parallelism requirement is important because otherwise the signal does not come back to the same location. But even more important is that a small misalignment will produce an interference effect.

3.1.4 Ultrasonics at low temperature

All the ultrasonic measurements herein were carried out using a VTI *^4He* evaporation cryostat and a *^3He*-*^4He* dilution top-loading refrigerator. All these are standard techniques and widely known so they will not be described in detail here apart from some short notes. More details about the operating principle of these systems can be found in the literature [Pobell07].

Figure 3.4 shows the operating setup of the VTI ^{4}He refrigerator with the needle valve. Static magnetic fields were supplied by a superconducting magnet inside the cryostat which can reach up to 14 Tesla at 4.2 K. For temperatures above 4.2 K, cooling can be achieved by simply using the ^{4}He gas flow taken directly from the main bath via the needle valve.
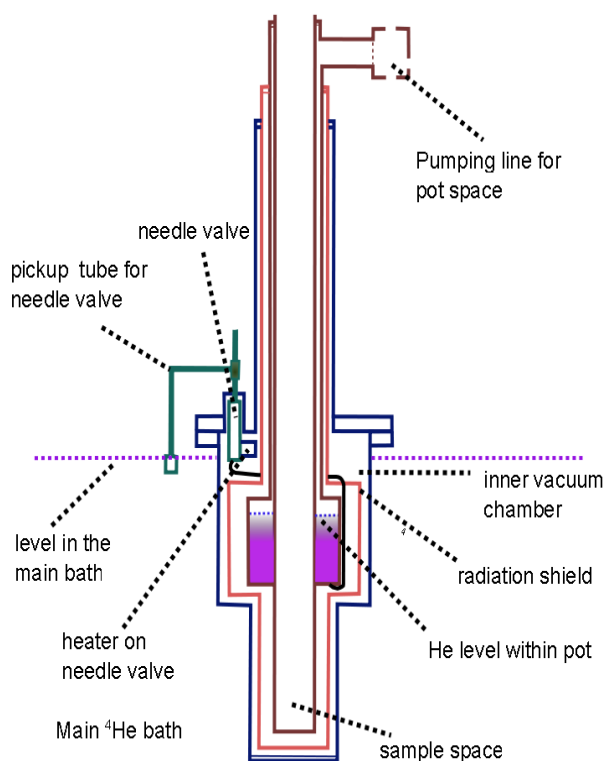
Figure 3.4 *Continuously operating ^4He refrigerator with needle valve.*

For the temperature range 1.3 K < *T* < 4.2 K, the simplest way is to pump a helium bath of ^4He cryostat with an immersed sample. However, since about 40% of the helium is evaporated when the bath is pumped and cooled from 4.2 K to 1.3 K, this method is not economically profitable, especially if such an experiment requires long times. The problem can be solved if a small amount of helium taken from the main bath is cooled only. In this case, after the insert has been cooled to 4.2 K, a small flow of liquid helium from the main bath is obtained via a needle valve to the insert. The insert is connected to the pump and then pumped down by a room-temperature vacuum pump. Using a needle valve allows more flexibility to adjust the temperature of the insert, although adjusting the flow can be quite difficult. Samples are mounted on a probe which is loaded through an airlock and a gate valve at the top of the insert. This top-loading arrangement allows samples to be changed without warming the system or contaminating the VTI with air.

For the temperature below 1 K, all the measurements are performed in a commercial top-loading $^3He/^4He$ dilution refrigerator model 400 TLM from Oxford Instruments company. A dilution refrigerator is a cryogenic device first proposed by Heinz London. Its refrigeration process uses a mixture of two isotopes of helium: ^3He and ^4He. When cooled below a critical temperature, the mixture undergoes

spontaneous phase separation to form a ^3He-rich phase and a ^3He-poor phase. The concentration of ^3He in each phase is dependent upon the temperature as shown in Fig. 3.5(a). Since the enthalpy of the ^3He in the two phases is different, the "evaporation" of ^3He from the concentrated phase into the dilute phase may provide highly effective cooling. In a gross simplification, the concentrated phase of the mixture is pretty much liquid ^3He, and the dilute phase is effectively ^3He gas. The ^4He composing the bulk of the dilute phase is inert and noninteracting, and may be neglected. The evaporation of ^3He from the "liquid" phase to the "gas" phase cools the sample.
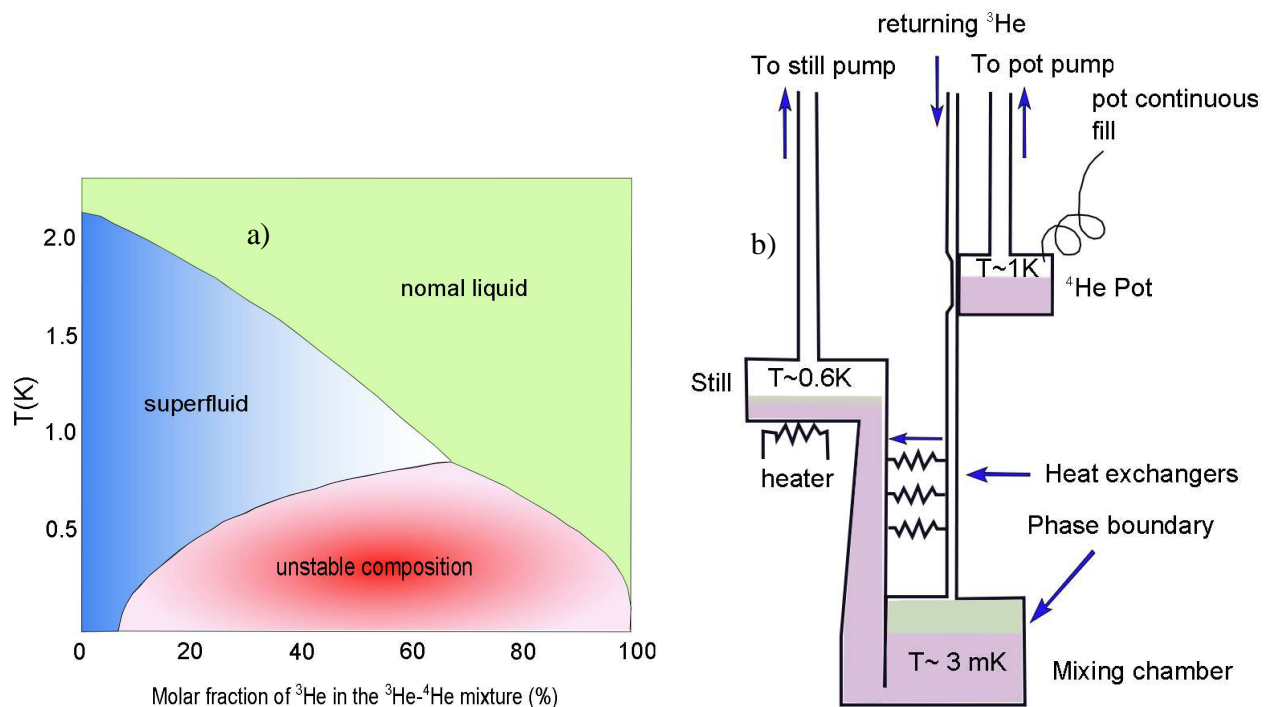
Figure 3.5 *a)* ^3He-^4He *phase diagram b) Schematic of dilution refrigerator (adapted from Ref.* *[Enss05]).*

When the refrigerator begins operation as shown in Fig. 3.5(b), the 1 K pot is used to condense the $^3He/^4He$ mixture in the dilution unit. It does not cool the mixture sufficiently to form the phase boundary, but simply to bring it to 1.2 K. Phase separation may be attained only once the temperature falls below the tri-critical point at 0.86 K. This cooling is provided by the still; incoming ^3He is cooled by the still before it enters the heat exchangers and mixing chamber. Gradually, the rest of the dilution unit cools to the point where phase separation occurs. During continuous operation, the ^3He must be extracted from the dilute phase and resupplied to the concentrated phase.

The ^{3}He is pumped down from the liquid surface in the still, where at ~ 0.6 K ^{3}He evaporates preferentially. ^{3}He leaving the mixing chamber is used to cool the returning flow of concentrated ^{3}He in a series of heat exchangers. A room-temperature vacuum pumping system is used to remove ^{3}He from the still and compress it before passing it through impurity-removing filters and cold traps (one at 77 K, the other at 4.2 K) and returning it to the cryostat. The inflowing mixture is pre-cooled by the main helium bath and condensed on the 1 K pot. A flow impedance is used to maintain a sufficiently high pressure in the 1 K pot region for the gas to condense. The experimental apparatus is mounted in the mixing chamber to ensure adequate thermal contact.

The advantage of top-loading dilution refrigerators is that the measurements became more easily feasible and the exchange of samples could be achieved within a few hours. Additionally, to reach up to milliKevin range, it is very important to use efficient ultrasonic transducers for low input power (piezoelectric foils). The transducers have to be contacted with very fine 20 μm gold wires. The repetition frequency of the signal has to be as low as possible. With all these precautions, low temperatures below 50 mK can be achieved.

3.1.5 Ultrasonics in pulsed magnetic field

Fig. 3.6 shows our high magnetic field equipment containing a computer-controlled capacitor bank of 32.65 mF with a maximum voltage of 7 kV and a stored energy of 800 kJ. The capacitors are discharged using a thyristor switch where the current is limited to 100 kA. A crowbar diode with a variable resistor is used to adjust the pulse length, the temperature rise of the coil after the pulse and the reversed voltage at the capacitor bank. It becomes active when the voltage changes sign, thus dissipating the energy and protecting the capacitors [Wolf01b].

The 50 T coil (developed at the National High Field laboratory in Tallahassee) has an inductance of $L = 1.81$ mH with a rise time of 8 ms and a typical pulse length of 25 ms. The coils are cooled down to 77 K to reduce their resistivity before each pulse measurement. With a crowbar resistor of 412 mΩ the temperature change after a 50 T pulse is raises up to 310 K. This change of temperature limits the maximum field and the pulse length. For such a 50 T pulse, we need an energy of 390 kJ. With a rise time of 8 ms the magnetic field changes 'slowly' in comparison with the important physical time constants of the sample. The experimental conditions are quasi-static.

However, in the case of experiments in pulsed magnetic fields, the feedback loop is now much too slow to follow the changes of the magnetic field. Therefore, all measurements must be

performed at a fixed frequency and the phase shifts, which are proportional to changes in sound velocity $\Delta v/v$, have to be calculated numerically using a computer afterwards. Thus we exchanged the feedback loop with a digital storage oscilloscope (or special AD converter) and we record I_n and Q_n at constant frequency as well as the magnetic field pulse as a function of time.
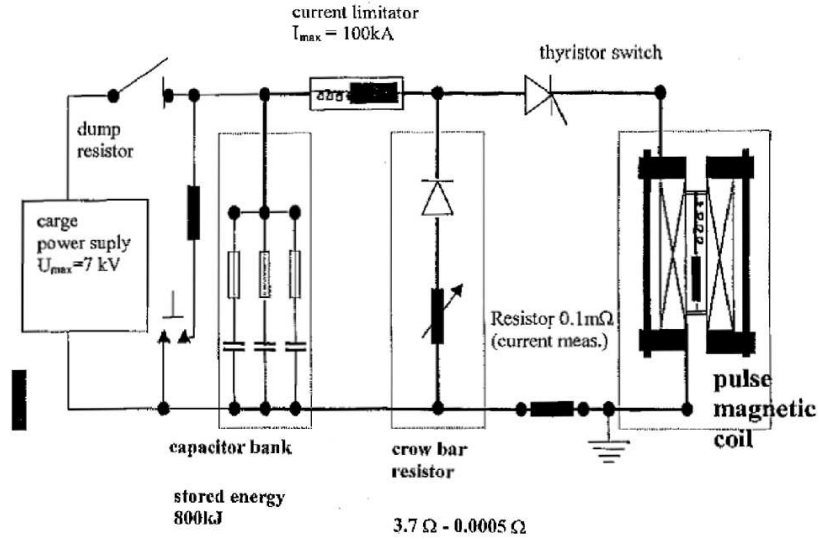
Figure 3.6 *High field apparatus (reprinted from Ref. [Lüthi05]).*

The analysis of the data in this so-called quadrature procedure is based on the following equations, see Fig. 3.7. The amplitude of the sound wave is calculated according to:

$$A_n = A_0 e^{-\alpha(2n+1)L} = \sqrt{I_n^2 + Q_n^2} \; . \tag{3.8}$$

The sound velocity v is proportional to the phase of the signal. One gets for a given echo n, and angular frequency ω of the sound wave and propagation time in the sample τ

$$\Phi_n = (2n+1)\omega\tau = \frac{(2n+1)\omega L}{v_s} = \arctan\left[\frac{Q_n}{I_n}\right]. \tag{3.9}$$

To determine the change of the sound velocity from the changes of the phase $\Delta\Phi$ one has to measure the initial sound velocity which is correlated to the initial phase $\Phi_0 = \omega n \tau_0$, τ_0 can be determined directly from the time delay between the electromagnetic signal and the *nth* echo where the data are taken. The resolution for sound velocity measurements for the equipment in Fig. 3.2 is

usually of the order of 10^{-6}. In the pulsed field mode this changes to $\sim 10^{-5}$. In order to get a high resolution it is also important to use a digital storage with large vertical resolution.
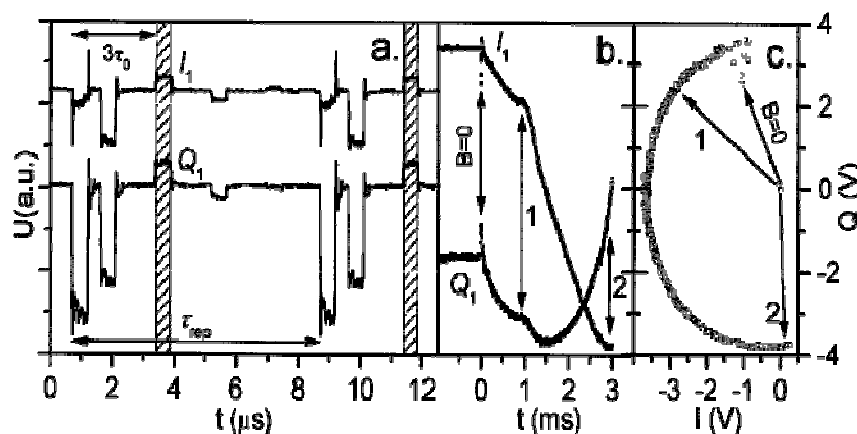

Figure 3.7 *Typical echo pattern in pulsed field ultrasonic experiments. Two channels I and Q are shown. Shaded area indicates the position of the gates. (b) Output voltage of gated integrator during a field pulse. (c) Vector representation of I_n and Q_n. The arrows correspond to the positions in time scale from (b) (reprinted from Ref. [Wolf01b]).*

3.2 Magnetic characterization

The macroscopic magnetic moment (*M*) of the samples in the presence of an external applied field (*H*) was measured at different temperatures *T*. The magnetic susceptibility $\chi(T)$ (normalized per mole) was calculated from *M* and *H* as:

$$\chi(T) = \frac{M}{H}\left(\frac{molar\,weight}{sample\,weight}\right).$$

The magnetization measurements were performed in a commercial SQUID magnetometer (Quantum Design MPMS XL-5) in the range 1.8 K < *T* < 400 K and for applied fields *H* up to 5 Tesla (5×10^4 G). The sensitivity of this equipment is of the order of 1×10^{-7} *emu* for the measured magnetic moments.

The SQUID (Superconducting Quantum Interference Devices) is the most sensitive device known for the measurement of magnetic flux. In this system, the magnetic moment of the sample is measured by moving the sample through superconducting detection coils (configured as a second

order gradiometer) which are connected by superconducting wires to the SQUID input coils forming a closed loop as shown in the sketch of Fig. 3.8. Any change of magnetic flux in the detection coils produces a proportional change in the persistent current in the detection circuit.
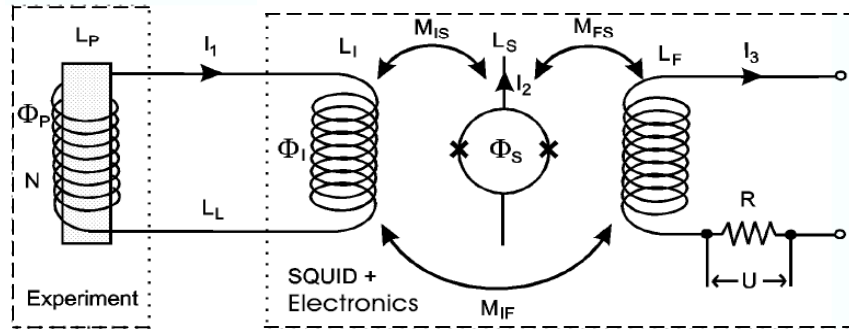
Figure 3.8 *Schematics of the magnetometer. Flux changes $\delta\Phi_P$ detected by the pickup coil are coupled into the SQUID via the flux transformer (reprinted from Ref. [Drung96]).*

Since the SQUID functions as a highly sensitive and linear current-to-voltage convertor, a variation in the detection coil current produces a corresponding variation in the SQUID output voltage, which is thus proportional to the magnetic moment of the sample.
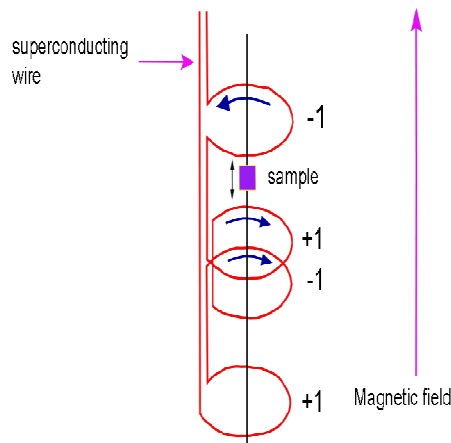
Figure 3.9 *Second-order gradiometer superconducting pick-up coils (adapted from Ref. [Drung96]).*

The sample is driven through the detection coils either by a continuous sinusoidal movement (RSO mode) or in discrete steps (DC mode) along the scan length. The currents induced in the

detection coil are ideally those associated with the movement of a point-source magnetic dipole through a second-order gradiometer detection coil as seen in Fig. 3.9. This signal requires that the sample has a size much smaller than the distance between the detection coils. If a sample is very long, extending well beyond the coil during a scan, its motion in the gradiometer will not be observable, since there would be no net change of magnetic flux in the detection coil. For this reason long uniform tubes were used as sample holders. The samples were mounted in a tube (made of a plastic material) and located in the centre of the detection coils, coinciding with the region of uniform external field in the centre of the superconductive magnet. The powder samples were mounted in a capsule made of cigarette paper and fixed in the tube by cotton. This paper and cotton have a very small diamagnetic signal that was carefully measured and subtracted as background, in an independent measurement. A careful determination of the magnetic background is important, especially at high temperatures where the magnetic signal is small. These capsules have a cylindrical shape and a typical size of about 2 mm long by 2 mm in diameter.

4

THE QUASI-1D DIAMOND CHAIN COMPOUND AZURITE

This chapter presents the experimental results of ultrasonic, thermal expansion and magnetic susceptibility measurements, performed on a single crystal of the quasi-1D distorted diamond-chain compound Azurite $[Cu_3(CO_3)_2(OH)_2]$. We aim to explore the strain dependence and the magneto-elastic coupling in this compound. In addition, ultrasound is used in combination with other thermodynamic probes such as thermal expansion and magnetic susceptibility to construct the detailed low-temperature phase diagram of Azurite.

4.1 Introduction

The distorted diamond chain (DDC) is a one-dimensional quantum-spin model with a structure as shown in Fig. 1(a). This model with spin-1/2 can be viewed as one of the simplest one-dimensional (1D) quantum frustrated systems, assuming that the exchange interactions along the chain are all antiferromagnetic. It has received a substantial amount of theoretical attention [Takano00, Tonegawa01, Honecker01, Okamoto99, Okamoto03, and Sakai09]. One reason is the occurrence of a plateau that could be observed at one-third of the saturation magnetization in the magnetization curve.
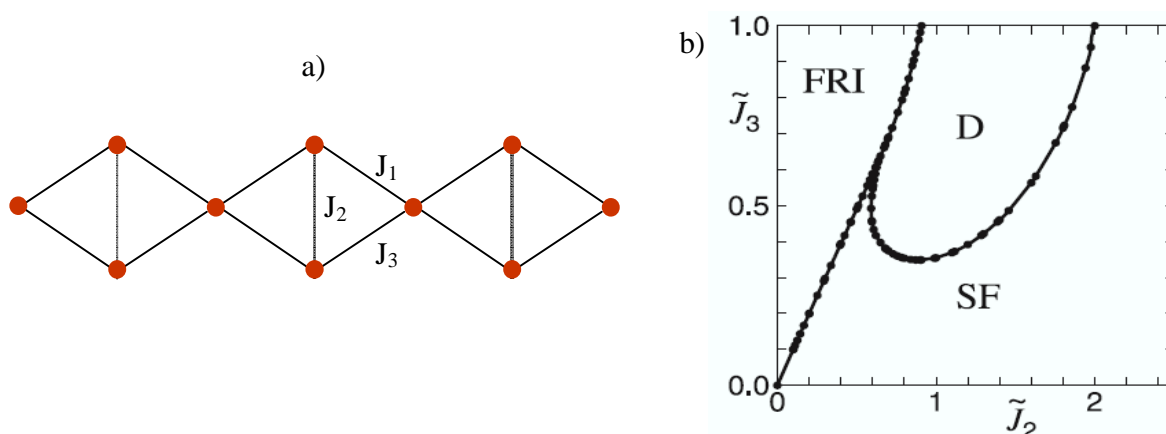

Figure 4.1 *(a) Structure and (b) phase diagram of the distorted diamond chain model (reprinted from Ref. [Tonegawa00])*

Another reason is the very rich ground-state phase diagram that comes from the competition of interactions as shown in Fig. 1(b), including the spin-fluid (SF), the dimerized (D), and the ferromagnetic (FRI) state [Tonegawa00]. Tonegawa *et al.* [Tonegawa01] investigated the ground state of the more general distorted-diamond chain in which exchange coupling constants J_1, J_2 and J_3 between adjacent $S=1/2$ spins are different. They pointed out that the distorted-diamond chain can be viewed as a periodic array of J_2 dimer and monomer spins if $J_2 \gg J_1$, J_3, or as an alignment of linear trimer spins when J_1 (or J_3) $\gg J_2$ as presented in Fig. 4.2(a) and (b), respectively.
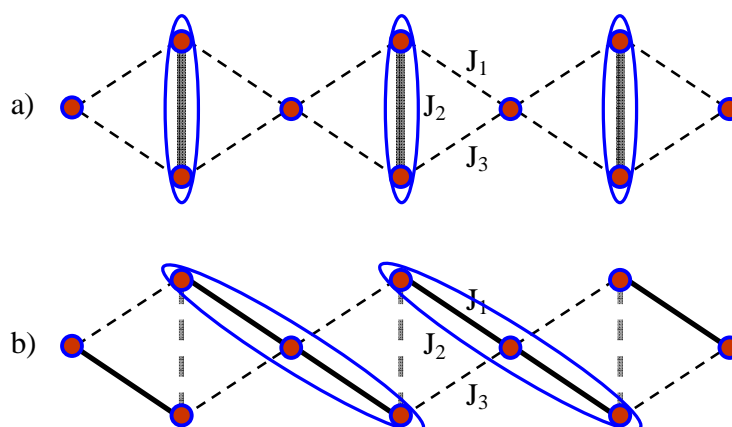
Figure 4.2 *Structure of the spin model of a diamond chain (a) dimer-monomer model and (b) linear-trimer model.*

In these two extreme cases, a one-third magnetization plateau is intuitively understood to be present, and the one-third magnetization plateau is found to appear in a broad region of the phase diagram. However, past theoretical studies primarily concentrated on the ground-state properties of the system, whereas thermodynamic features are still sparse. One reason being a lack of appropriate actual real materials needed for experimental work in past years. Recently, it was proposed that Azurite, a natural mineral of composition $Cu_3(CO_3)_2(OH)_2$, can be regarded as a model substance of a distorted-diamond chain which revealed a distinct plateau at 1/3 of the saturation magnetization [Kikuchi05a].

4.2 Structure and magnetic properties

Azurite has a monoclinic crystal structure (space group *$P2_1/c$*) with room-temperature lattice parameters $a = 5.01$ Å, $b = 5.85$ Å, $c = 10.3$ Å, and a monoclinic angle, $\beta = 92.4°$ in which *Cu^{2+}* (S =

1/2) magnetic ions located at the corners of diamond units form infinite chains along the *b*-axis as shown in Fig. 4.3 (a) [Gattow58, Zigan72 and Belokoneva01].
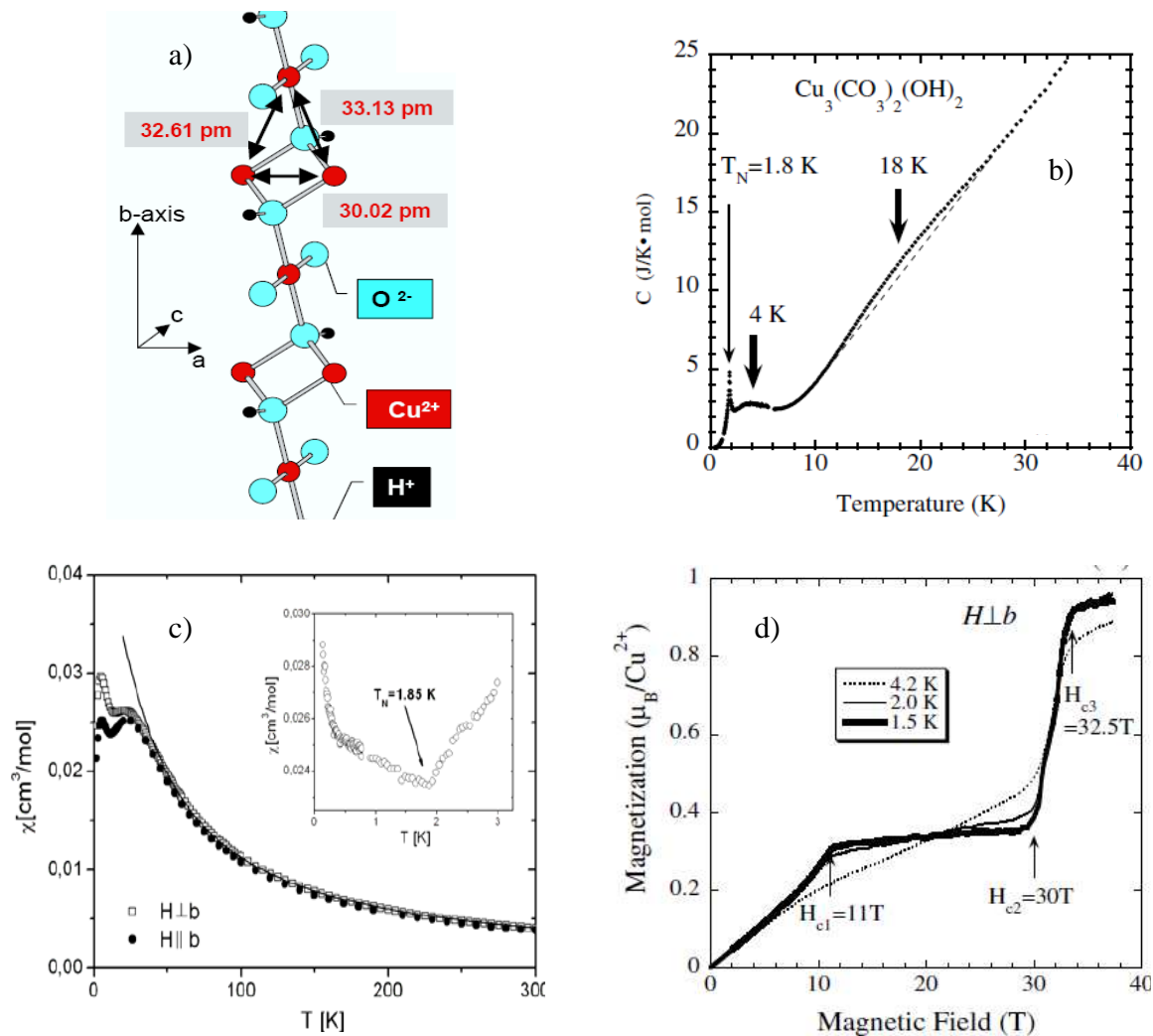
Figure 4.3 *(a) Structure of Azurite (reprinted from Ref. [Krämer06]). (b) and (c) show the temperature dependence of the specific heat and magnetic susceptibility χ(T), respectively. Inset of (b) shows the low-temperature part of χ(T). (c) displays the high-field magnetization curves measured below 4.2 K. The applied magnetic field was perpendicular to the b-axis ((b), (c) and (d) are reprinted from Refs. [Kikuchi05a] and [Lang06]).*

Investigations by high-field electron spin resonance [Okubo05], as well as by static measurements (magnetization, susceptibility, specific heat) have been performed [Kikuchi05a, Lang06]. Fig. 4.3 (b) and (c) display the experimental data of the magnetic susceptibility and

specific heat. We can observe a double-peak structure around ~ 25 K and ~ 5 K, followed by an antiferromagnetic (AFM) long-range order at T_N = 1.86 K. Figure 4.3 (d) shows the magnetization measurements. The existence of the 1/3 magnetization plateau has been clearly established between 16 T - 26 T or 11 T – 30 T when the magnetic field H was applied parallel (not shown here) or perpendicular to b-axis, respectively, consistent with theoretical predictions. It is also indicated that the coupling of the spins within the chain could be described by a monomer-dimer model as displayed in Fig. 4.2(a). This interpretation was later confirmed by nuclear magnetic resonance (NMR) measurements [Aimo09], which revealed the singlet state of the dimers and the full polarization of the monomers at the plateau region. Beyond the static properties investigated so far, the dynamical properties of Azurite remain attractive both experimentally [Rule08] and theoretically, [Gu07] and [Mikeska08]. The characteristic features of the model, namely, the presence of two different energy scales and their mutual influence will show up most clearly in the energy spectra. These are best investigated by inelastic neutron scattering (INS) experiments, as clearly seen in Ref. [Rule08].

The proposed magnetic model and the dimensionality of Azurite is, however, disputed both in experimental and theoretical studies. Some authors have suggested a ferromagnetic J_3 < 0 [Rule08, Gu06] which would render the model non-frustrated, whereas other authors have argued that the interchain coupling is important [Kang09]. Recent first-principles density-functional computations [Jeschke11] indeed yield a three-dimensional coupling geometry with a dominant antiferromagnetic dimer exchange constant J_2 > 0. Nevertheless, a closer inspection of the exchange geometry allows one to map this three-dimensional network effectively onto the *generalized diamond chain* which gives a reasonable description at higher energy scales, (*i.e.*, T > 2 K or in the plateau region) covering a broad range of experimental results, including the magnetization curve, the magnetic susceptibility, the specific heat [Kikuchi05a], the structure of the one-third plateau as determined by NMR [Aimo09] and inelastic neutron scattering on this one-third plateau [Rule08]. These studies thus place Azurite in the highly-frustrated parameter regime of the 1D diamond chain. However, at an energy scale of a few Kelvin, *i.e.*, T < 2 K, some parameters such as inter-chain coupling and magnetic anisotropy, neglected in the above *generalized diamond chain* model, now play an important role and affect the magnetic properties of Azurite in the very low-temperature region. The studies of magnetic and structural properties of Azurite recently performed at very low temperature by inelastic neutron scattering (ISN) and muon-spin resonance (μSR) measurements, suggest a more complicated micromagnetic structure than has been previously thought, with the coexistence of

magnetic order with structural distortion [Gibson10]. Besides that, the detailed field-temperature (*B-T*) phase diagram as well as the static spin structure at low temperature is still unknown. This motivated the current study about the magnetic phase diagram and the interdependence of structure to magnetic degrees of freedom.

In this thesis, ultrasound measurements were used to study the strain dependence and the magnetoelastic coupling in Azurite. The results were discussed in connection with the supporting information obtained from magnetic susceptibility under pressure [Mariano09] and thermal expansion measurements [Brüehl08]. The *B-T* phase diagram at very low temperature was also revealed in detail up to the plateau region in both directions $B // b$ and $B \perp b$-axis.

4.3 Sample preparation

The samples for the various measurements were cut out of a large high-quality single crystal that was also used in INS and μSR measurements [Rule08], [Gibson10]. The crystal was supplied by the Institute of Mineralogy at the University of Frankfurt. The crystal, which is used for ultrasonic measurement, has a dimension of about 2.7 x 2.3 x 2.5 mm^3. Two opposite surfaces, normal to the [010] crystallographic axis, were polished and a pair of piezoelectric thin-film transducers were glued to the surfaces. These transducers generate longitudinal sound waves propagating along the [010] direction, corresponding to the acoustic c_{22} mode**.** The measurements with the acoustic frequency of 75 MHz were performed as the function of temperature (down to 80 mK) and static fields (up to 12 Tesla).

Magnetic susceptibility measurements under pressure have been performed with a SQUID magnetometer (Quantum Design, MPMS). High pressure was generated by a piston cylinder clamped cell, using Daphne oil 7373 as a pressure-transmitting medium. The pressure at low temperature was determined by the superconducting transition temperature of Indium. Thermal expansion measurements, $\alpha_i(T) = l_i^{-1}(\partial l_i/\partial T)$, where $l_i(T)$ is the sample length, were carried out by using an ultrahigh-resolution capacitive dilatometer with resolution up to $\Delta l/l = 10^{-10}$ [Pott83]. Measurements were conducted along a', b and c^* axes, where a' and c^* are perpendicular to the (-102) and (102) crystallographic planes, respectively.

4.4 Results and discussions

4.4.1 Strain dependence
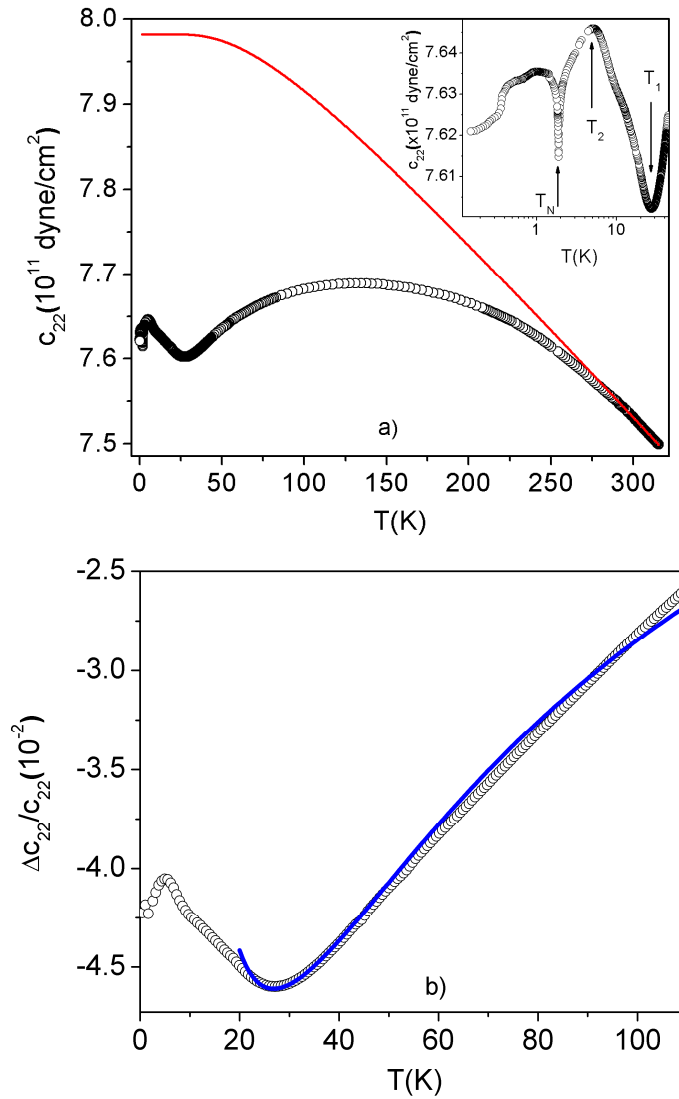
Figure 4.4 a) Temperature dependence of the $c_{22}(T)$ mode. Full line is the background $c_{22}^0(T)$. Inset: low-temperature part of $c_{22}(T)$ vs. log(T). Arrows mark the short-range ordering of dimer (T_1), monomer (T_2) and long-range ordering (T_N). b) $\Delta c_{22}(T) = (c_{22}(T) - c_{22}^0(T))/c_{22}^0(T = 0)$ data (open circles) as a function of temperature with a fit according to Eq. (4.1) (solid line).

Fig. 1 (a) shows the temperature dependence of the longitudinal elastic constant $c_{22}(T)$ plotted together with the elastic constant background $c_{22}^0(T)$ that is derived from the phenomenological expressions $c_{ij} = c_{ij}^0 - \dfrac{s}{e^{t/T} - 1}$, where s and $t \sim \theta_D/2$ (θ_D is the Debye temperature) are constants, cf. chapter 2 for details. Using the value of $\theta_D = 350$ K that was used in Ref. [Kikuchi05b] to estimate the lattice contribution to specific heat data, the function given above has been fitted to the high-

temperature part of the experimental data ($T > 275$ K) where the temperature dependence of the elastic constant obeys this expression. The fitted results are displayed as the solid lines in Fig. 4.4(a). The magnetic contribution to the elastic constants is obtained by subtracting the measured data from the elastic background as illustrated in Fig. 4.4(b). Details of the low-temperature part of $c_{22}(T)$ are exhibited in the inset of Fig. 4.4(a). A sharp anomaly is observed at 1.8 K, reflecting the occurrence of the long-range magnetic order. This temperature is consistent with the reported value for the Néel temperature T_N [Kikuchi05a]. A new finding from our sound velocity measurement is the observation of the steep decreasing of $c_{22}(T)$ at very low temperature ($T < 0.5$ K) as well as the appearance of two anomalies, a minimum and a maximum around 25 K and 5 K, respectively, corresponding to the temperature at which the formation of dimers and short-range ordering of monomers occur, respectively.

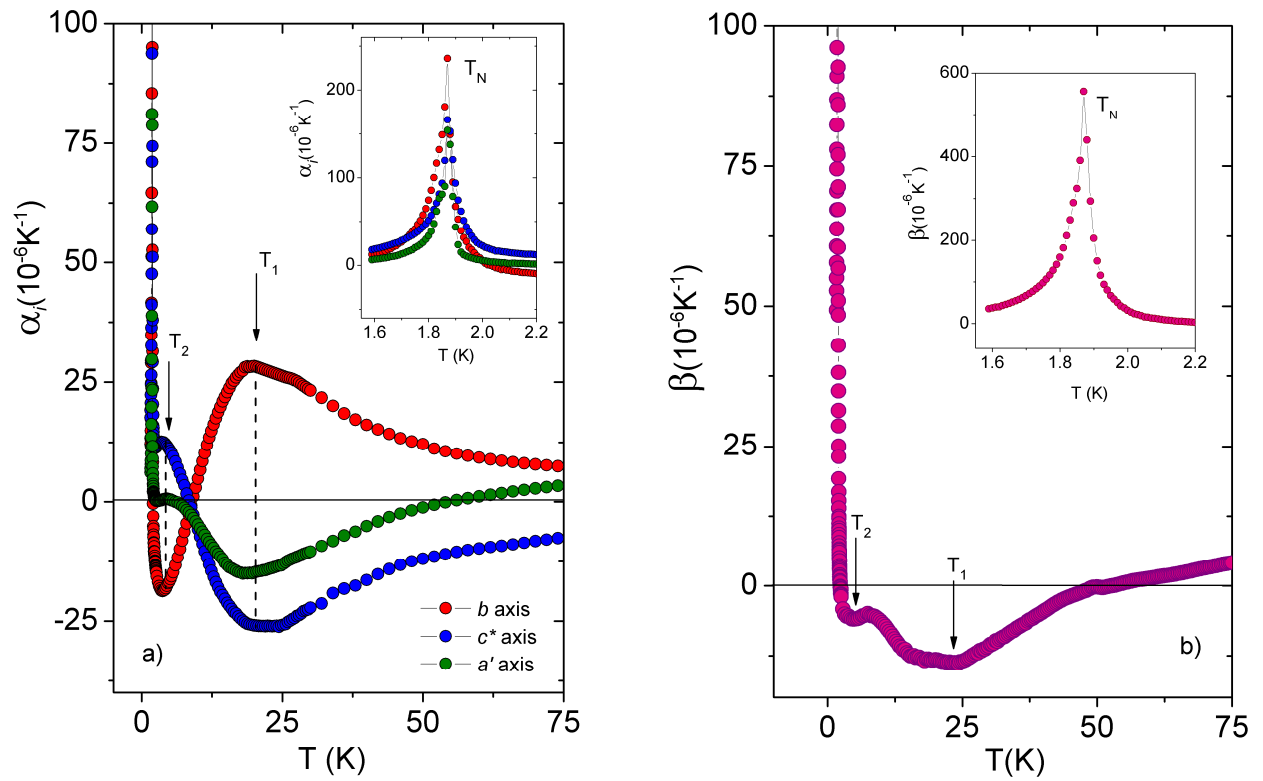**Figure 4.5** a) Uniaxial expansivities along three orthogonal axes. Arrows mark the short-range ordering temperatures of dimer (T_1) and monomer (T_2). Broken lines at T_1 and T_2 are guides for the eyes. b) Volume expansivity $\beta = \alpha_{a'} + \alpha_b + \alpha_{c*}$ determined from the data in a). The insets of (a) and (b) show details of the anomalies at T_N [Brüehl08].

Fig. 4.5(a) shows the results of the temperature dependence of the thermal expansion coefficient $\alpha_i(T)$ ($i = a', b, c*$) for temperatures below $T = 75$ K at ambient pressure and zero magnetic field. Three distinct anomalies are observed along the three different crystallographic axes. Upon cooling, the data, measured along the b-axis, show a broad positive maximum at $T_1 \approx 20$ K whereas along the two other axes (a' and $c*$) a negative minima appears. Upon further cooling to lower temperatures, one more feature which appears as a minimum in the b, a'-axes and as a maximum in the $c*$-axis, is observed at $T_2 \approx 5$ K. These temperatures coincide closely with those where the rounded peaks appear in the magnetic susceptibility and specific heat, cf. Fig. 4.3(b and c) and Fig. 4.6. Finally the long-range AFM order takes place at $T_N \approx 1.88$ K reflected in a huge λ–like peak in the thermal expansion coefficients. This is shown clearly in the inset of Fig. 4.5(a) on expanded scales. The various anomalies are also seen clearly in the volume expansion coefficient $\beta(T) = \alpha_a(T) + \alpha_b(T) + \alpha_{c*}(T)$, shown in Fig. 4.5(b).

The huge softening of $c_{22}(T)$ and large anomalies in $\beta(T)$ observed in the low-temperature region, indicates the strong influence of the magnetic properties to the elastic behavior, $i.e.,$ a strong spin-phonon interaction. The anomalies observed at T_1 and T_2 reveal clearly two energy scales governing the thermodynamic properties of this material. The higher and dominant energy scale is associated with the intradimer coupling whereas the lower energy scale has been identified as the correlation between monomers induced via the coupling through the dimers. The effect of $c_{22}(T)$ at T_1 is reminiscent of the behavior observed for the coupled-dimer system $SrCu_2(BO_3)_2$, where the minimum of $c(T)$ is also recognized to be due to the formation of spin dimers [Wolf01a].

In order to quantitatively evaluate the elastic coupling of the Cu^{2+} dimer interaction, the generalized strain susceptibility χ_{str} formula is used to calculate the temperature dependence of the elastic constants in the frame of a random-phase approximation (RPA) molecular-field theory for the coupled-dimer model [Wolf01a]. We define the strain susceptibility as the response function of an applied strain. So the temperature dependence of elastic constant can be expressed as follows:

$$c_{22}(T) = \frac{\delta^2 F}{\delta \varepsilon_{22}^2} = c_{22}^0(T) - G^2 N \chi_{str} \tag{4.1}$$

where: $\chi_{str} = \dfrac{\chi_s}{1 - K\chi_s}$,

and the strain susceptibility of the single dimer with respect to singlet-triplet gap Δ:

$$\chi_s = G^{-2}\frac{\partial^2 F}{\partial \varepsilon^2} = \frac{3e^{-\Delta/kT}}{k_B T Z^2}.$$

Here Z is the partition function, K is the strength of the effective dimer-dimer interaction that can be mediated, e.g., by phonons, $G = \dfrac{\partial \Delta}{\partial \varepsilon}$, i.e., $G = \dfrac{\partial J_2}{\partial \varepsilon}$ is a single-dimer coupling or exchange-striction coupling constant and N is the density of dimers [Lüthi05].

Using the number of dimers N = 3.3×10^{21} cm^{-3} and c^0(T = 0) = 7.96×10^{21} erg/cm^3, we conducted the nonlinear least-square fitting with two free parameters K and G in the high-temperature region down to T_1 where the dimers play the dominant role. The solid line in Fig. 4.4(b) shows the result of the fitting based on equation (4.1). The fit plotted in Fig. 4.4(b) has a minimum at the same temperature T_1 as the experimental data and shows a fairly good agreement with the experimental data at $T \geq 22$ K, while the difference is large for $T \leq 22$ K due to the complex magnetic interactions at lower temperatures. The fitting result gives the singlet-triplet gap, $\Delta = 54$ K and the dimer-dimer coupling constant $K \sim 100$ K. The value or the gap Δ is very close to the value of 50 K obtained by ESR measurements [Okubo05]. The single-dimer coupling constant G, which measures the strain dependence of the singlet-triplet gap, has been also obtained to $G \sim 1700$ K. This value is comparable with the largest one found in the coupled-dimer system SrCu$_2$(BO$_3$)$_2$ [Zherlitsyn00] and implies a very strong coupling of the Cu^{2+} spin dimers to the lattice. It may be responsible for the structural distortions observed at the AFM transition as discussed below.

In order to have a more quantitative evaluation of the strain dependence of the dimer interaction, we conducted the magnetic susceptibility measurement under various pressures. Fig. 4.6 displays the data of the magnetic susceptibility $\chi(T,p)$ as a function of temperature in the range from 300 K to 2 K under different constant pressures. The data were taken in a field of 2 T applied parallel to the b-axis with pressure varying from 0 to 6.2 kbar. At $p = 0$ kbar, the data are consistent with those reported by Kikuchi et al. [Kikuchi05a], including the broadened maxima at T_1 and T_2. A remarkable decrease of the position of T_1 (-1 K·kbar^{-1}) to lower temperatures with increasing pressure was observed. On the other hand, the position of T_2 changes only by $\sim$ -0.2 K·kbar^{-1}, cf. Fig. 4.6(b). Simultaneously, the low-temperature value of the magnetic susceptibility increases with increasing pressure.

The isolated-dimer model was again applied to describe the magnetic susceptibility data using the similar value of the singlet-triplet gap $\Delta = 54$ K for the data at $p = 0$ kbar in the temperature

range of $T_1 < T < 300$ K. It gives a rather good overall agreement with the data and can well reproduce especially the position of T_1 at the different pressure values as shown in Fig. 4.5.
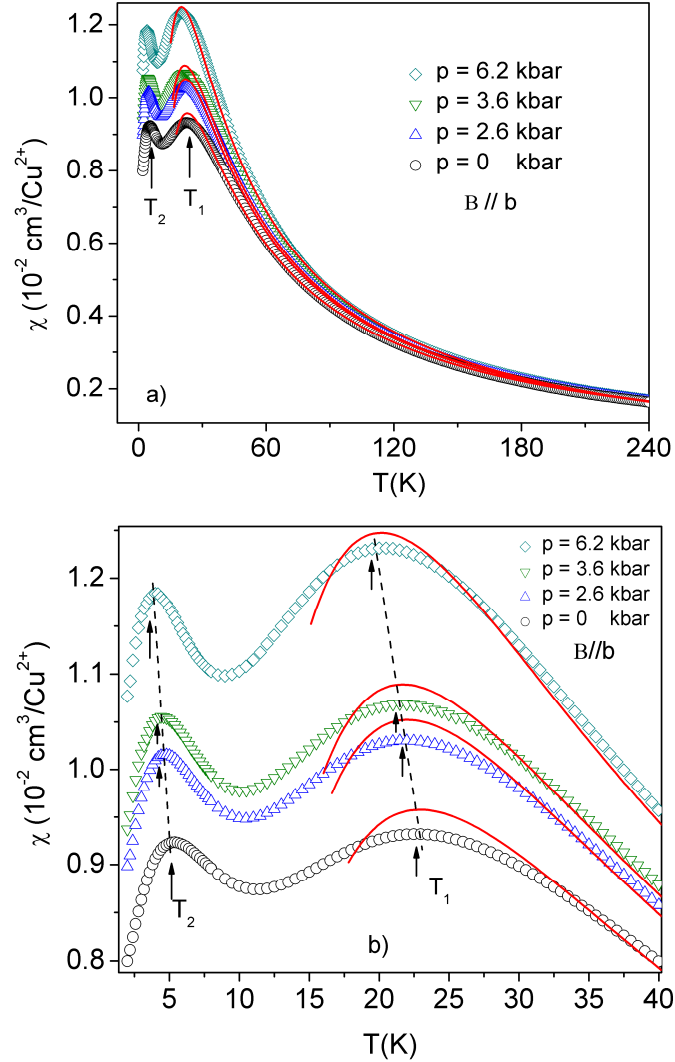
Figure 4.6 *a) Temperature dependence of the magnetic susceptibility under various applied pressures and the field parallel to the b-axis. Red solid line is the result of a fit based on the isolated-dimer model (see text). b) Data in the vicinity of T_1 and T_2 are shown on an enlarged scale. Arrows indicate the changes of the positions of T_1 and T_2 under pressure [Mariano09].*

At finite pressure, we also obtained a fairly good description with the value of the pressure dependence of the singlet-triplet gap of $d\Delta/dp \sim 1$ K·kbar^{-1}, i.e., $\dfrac{\partial J_2}{\partial p} \approx -1\,\mathrm{K}\cdot\mathrm{kbar}^{-1}$. The temperature T_1, being the characteristic temperature of the intra-dimer interaction, provides the measure for the

strength of the intra-dimer coupling constant. The strain dependence of the exchange coupling can be derived from the pressure dependence of the corresponding characteristic temperature T_1 by the relation $\delta(k_B T_1)/\delta p = C^{-1}\delta J/\delta\varepsilon$; here C, ε and J are the elastic modulus, the strain and the exchange coupling constant, respectively. Using this relation, we can estimate the strain dependence of the single-dimer coupling constant $\dfrac{\partial J_2}{\partial \varepsilon}$ and find it to be of the order of ~ 1000 K, in rough agreement with the result for the strain dependence obtained above.

This simple RPA expression for the dimer-model accounts quite well for the effect of the dominant energy scale characterized by the temperature T_1 as observed in $\chi(T)$, $c_{22}(T)$ and $\beta(T)$. From these results, we can conclude that the strain interactions are very important in this compound. These experimental findings are interpreted appropriately by the monomer-dimer model which also provides a natural explanation for the 1/3 plateau seen in magnetization experiments as discussed in Refs. [Kikuchi05a], [Rule08] and [Aimo09].

4.4.2 Magneto-elastic coupling

At T_N = 1.88 K, we observed a very sharp minimum and a sharp kink in $c_{22}(T)$ and $\chi(T)$, respectively, displayed in Fig. 4.7(a), coinciding with a pronounced anomaly in $\alpha_i(T)$, cf. inset of Fig. 4.5(b), that reflects the entrance into the AFM ordered state. The size of the elastic anomaly is of the order of 0.1%, which is considerably larger than the features observed in other low-dimensional quantum spin systems, where only *kink-like* anomalies were observed at the AFM transition, cf. Ref. [Sytcheva10] for an example. Additionally, the volume thermal expansion coefficient $\beta(T)$ has an extraordinary large anomaly of $\Delta\beta = 550 \cdot 10^{-6}\,\mathrm{K}^{-1}$, as exhibited in the inset of Fig. 4.5(b), implying a strong reduction that leads to a significant strain in the lattice. These results thus indicate that there is a huge spin-lattice coupling accompanying the occurrence of long-range magnetic ordering in agreement with the conclusion from Ref. [Gibson10].

To get more information on the field dependence of the acoustic anomalies, measurements were conducted in both static and high pulsed fields. In static fields, the data of $c_{22}(B)$, reveal a pronounced softening with increasing field and show an anomaly at around 10 T marking the entrance into the 1/3 plateau region [Kikuchi05a], regardless of the applied field direction. The size of this softening increases quickly as the system enters deeply into the long-range ordered state, cf. Fig. 4.7(b) and Fig. 4.12. The field dependence of $c_{22}(B)$ in the ordered AFM phase resembles the *b-*

axis magnetostriction data [Wolff-Fabris09]. At 0.85 K, the softening of $c_{22}(B)$ reaches values of about 1% as illustrated in Fig. 4.7(b) which cannot be explained by magnetostriction (~10^{-4}). This observation is a clear evidence for a strong magneto-elastic interaction within the AFM ordered state. The same conclusion was also obtained from the pulsed field data measured for B // *b*-axis reported previously [Lang06]. The results showed a drastic softening of the elastic c_{22} mode with a minimum at 31 T - a typical behavior of a resonant interaction between the sound wave and the magnetic excitations indicating a significant spin-phonon interaction in this material.
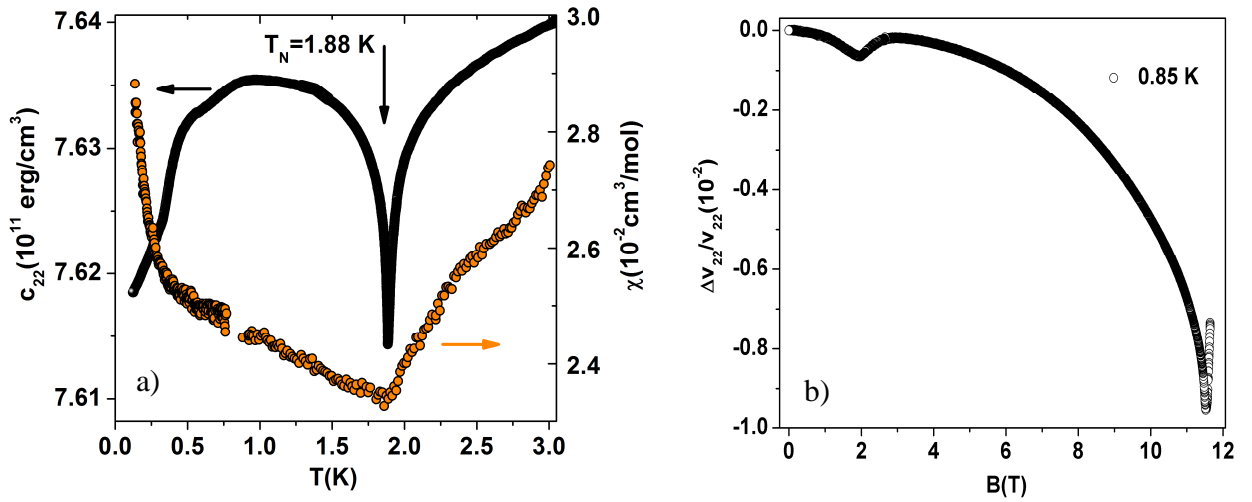
Figure 4.7 *a) Temperature dependence of the $c_{22}(T)$ acoustic mode for B = 0 T (left scale) and the magnetic susceptibility $\chi_{mol}(T)$ (right scale) in the vicinity of the AFM transition. b) Field dependence (B $\perp$ b-axis) of $\Delta v_{22}/v_{22}$ at 0.85 K up to the critical field of the plateau region.*

To conclude this subsection, we emphasize that Azurite can be well described as a model system for the 1D diamond chain at temperatures above 2 K [Jeschke11]. However, a strong magneto-elastic exchange coupling must be taken into account in the "full model" Hamiltonian for describing the low-temperature region, including the 3D long-range AFM order.

4.4.3 Critical behavior of sound velocity and attenuation

Fig. 4.8 (a) shows a typical attenuation and sound velocity results for the c_{22} mode in the temperature range around the AFM phase transition. The sharp dip observed in the velocity, closely coincides with the maximum of the λ-like anomaly of the attenuation at this second-order phase transition. To check for the frequency dependence of these anomalies, the data of the sound velocity

and the attenuation, measured at 50 MHz and 75 MHz, are shown in Fig 4.8 (b) and (c), respectively. In the case of the sound velocity, there was no significant difference within the accuracy of the experiment, either above or below the transition. However, the attenuation increases by about a factor of 2 when the frequency increases from 50 MHz to 75 MHz. This agrees nicely with the discussion in chapter 2.2.4 indicating that the critical contributions to the sound velocity at magnetic phase transitions are frequency independent while those of the sound wave attenuation closely follow a quadratic frequency dependence. So the anomalous contribution to the sound velocity Δv and attenuation α can be described by power-law formulas $-\dfrac{\Delta v}{v_0} \sim \omega^0 \varepsilon^\varsigma$ and $\alpha \sim \omega^2 \varepsilon^\eta$, respectively.

ς and η are the critical exponents, v_0 is the velocity of the normal variation at the critical point T_N, ω is the angular frequency of the acoustic mode and ε is the reduced temperature $\varepsilon = (T - T_N)/T_N$. To get the critical contribution, one has to subtract a background arising from other sources (anharmonic terms, imperfections, etc) by following the same procedure as indicated in subchapter 4.3.1 for the sound velocity and Ref. [Lüthi70] for the attenuation.
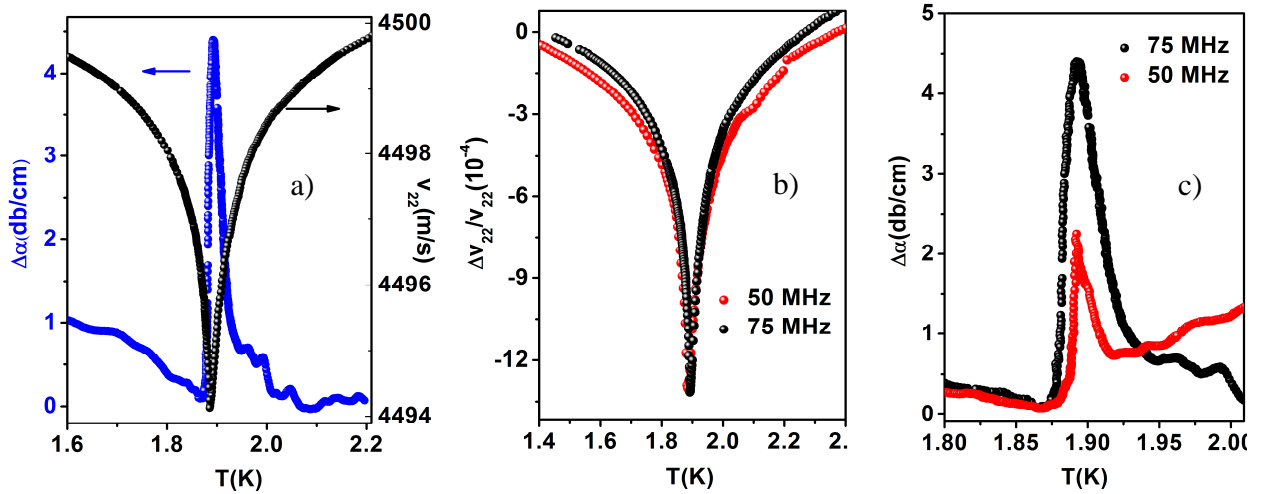
Figure 4.8 *a) Sound velocity (black balls) and attenuation (blue balls) changes measured at 75 MHz of Azurite as a function of temperature around the AFM phase transition. b) and c) show the temperature dependence of the relative change of the sound velocity and the sound attenuation measured at 50 MHz (red balls) and 75 MHz (black balls), respectively.*

Fig. 4.9 shows the critical sound attenuation (panel (a)), and critical sound velocity (panel (b)) deduced from Fig 4.8 (a) in a double-logarithmic plot. The main panel of a) and b) displays the data

for $T > T_N$ and the insets for $T < T_N$, respectively. The clear critical behavior can be observed in the temperature range $\varepsilon > 6 \cdot 10^{-3}$ in both sound velocity and sound attenuation for above and below T_N. The observed roll-off in critical behavior close to T_N ($\varepsilon < 10^{-3}$) may be caused by impurities and can also be due to the strong magnetoelastic-coupling in the vicinity of the critical point [Lang11]. However it is not related to a breakdown of the conditions such as $\omega\tau_c << 1$ (chapter 2.2) which would cause a marked frequency dependence, contrary to the observations shown in Fig 4.9 (c).

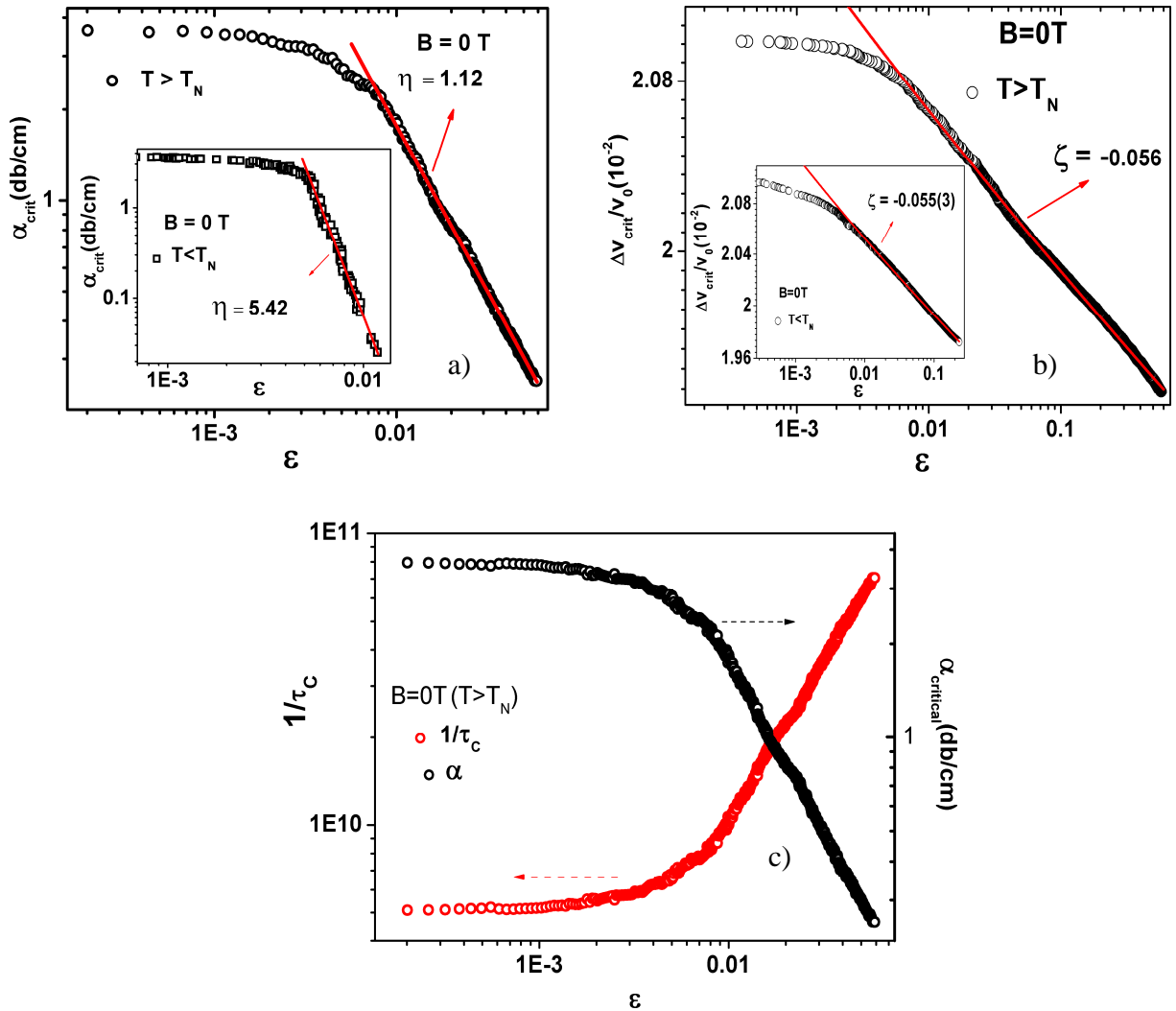**Figure 4.9** *The log-log plot of the sound attenuation, shown in panel (a), and sound velocity, shown in panel (b) of 75 MHz longitudinal waves versus reduced temperature ε for $T > T_N$ (main panel) and $T < T_N$ (inset), respectively. c) Double-log plot of the sound attenuation (right-hand ordinate) and $1/\tau_c$ (left-hand ordinate) versus reduced temperature ε.*
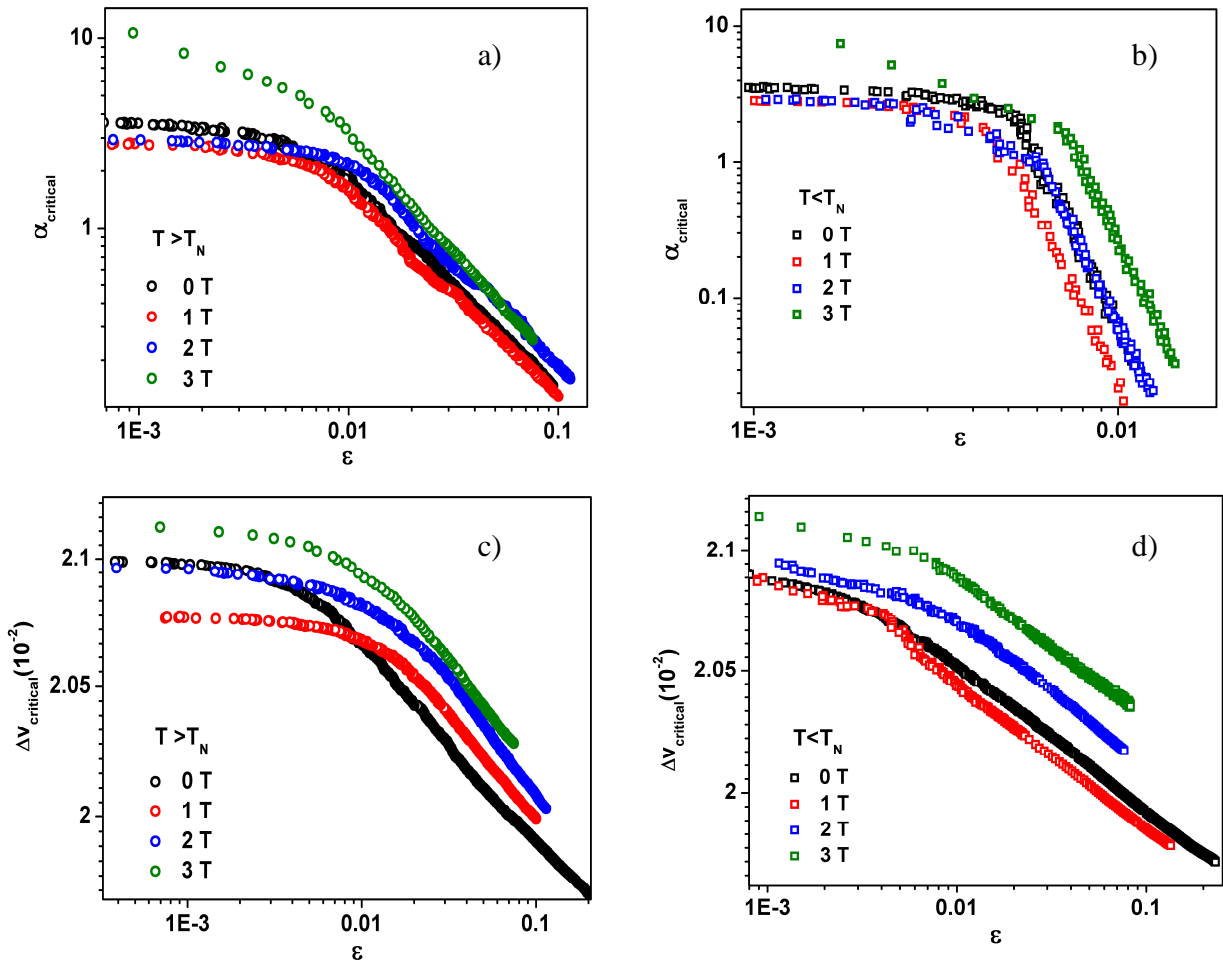
Figure 4.10 *The log-log plot of the sound attenuation, shown in panel (a) and (b), and the sound velocity, shown in panel (c) and (d), of 75 MHz longitudinal waves versus reduced temperature ε measured at various applied magnetic fields for $T > T_N$ and $T < T_N$, respectively.*

In the case of the attenuation, by fitting the data with a power law, we find a critical exponent of $\eta \sim 1.12$ in the paramagnetic state ($T > T_N$) that is significantly different from $\eta \sim 5.422$, obtained in the ordered state ($T < T_N$). The value of $\eta = 1.12$ obtained here for the paramagnetic phase is in agreement with the theoretical prediction by Bennett [Bennett69] of $\eta \sim 1$ for the isotropic Heisenberg antiferromagnet. Here a perturbation treatment was made for the decay rate of one sound wave into two, three or four other sound waves and the scaling law concept was used. The extraordinarily large value of *η* in the ordered state might indicate additional extrinsic damping effects. As a possible source we mention the extraordinarily strong lattice distortion accompanying the magnetic transition which may lead to the formation of domains acting as scattering centres for the sound waves.

In the case of the sound velocity, we obtain the same critical exponent of $\zeta \sim -0.056$ for both $T > T_N$ and $T < T_N$ that indicate a common mechanism driving the system at the critical region. According to ref. [Lüthi70] the critical contribution of the sound velocity is expected to show the same power-law behavior as the specific heat, i.e., $\zeta \approx \alpha$. Therefore $\zeta \sim -0.056$ is indicative of a 3D isotropic antiferromagnet, for which $\alpha = -0.12$ is predicted [Pelissetto02], rather than the anisotropic variant where $0 \leq \alpha \leq 0.14$ [Pelissetto02]. .

In addition, in Ref. [Lüthi70], Lüthi pointed out that the ratio of $\Delta v/v$ and α should then give directly a measure of $1/\tau_c$. In Fig. 4.9(c) we have made a log-log plot of $1/\tau_c$ for $T > T_N$ (left-hand ordinate scale) calculated from the actual experimental values of both $\Delta v/v$ and α by using the formula:

$$\frac{1}{\tau_c} = -\frac{\omega^2}{v_0} \frac{\Delta v / v_0}{\alpha} \ .$$

One can clearly see the critical slowing down of $1/\tau_c$ as a function of diminishing ε. The slope indicates that $1/\tau_c$ is proportional to $\sim \varepsilon^{1.26}$, rather close to the expected value of the attenuation shown above.

Fig 4.10 shows the log-log plots of the critical attenuation (panel (a) for $T > T_N$ and (b) for $T < T_N$) and the sound velocity (panel (c) for $T > T_N$ and (d) for $T < T_N$) vs. reduced temperature ε under various applied fields. The plots show a uniform behavior as the applied field changes from the AFM to SF state. It means that a similar mechanism drives the critical contribution when crossing from the PRM to the AFM or to the SF state.

4.4.4 B-T phase diagram

The *B-T* phase diagrams have been constructed from various measurements of $c_{22}(B,T)$ and $\alpha_i(T,B)$ as a function of field and temperature. Here only some selected results are presented and discussed. Fig. 4.11 shows variations of the uniaxial thermal expansion coefficient $\alpha_{c*}(T)$ (shown in panel (a) with applied field perpendicular to *b*-axis) and relative change of the sound velocity (shown in panel (b) and (c) with applied field parallel and perpendicular to *b*-axis, respectively) at different magnetic fields in the vicinity of the AFM phase transition temperature. In thermal expansion, the transition into the AFM phase appears as a λ-like anomaly reflecting the character of

the second-order phase transition. Interestingly, this anomaly has a double-peak structure with a temperature difference in the two anomalies of ≈ 0.2 K.
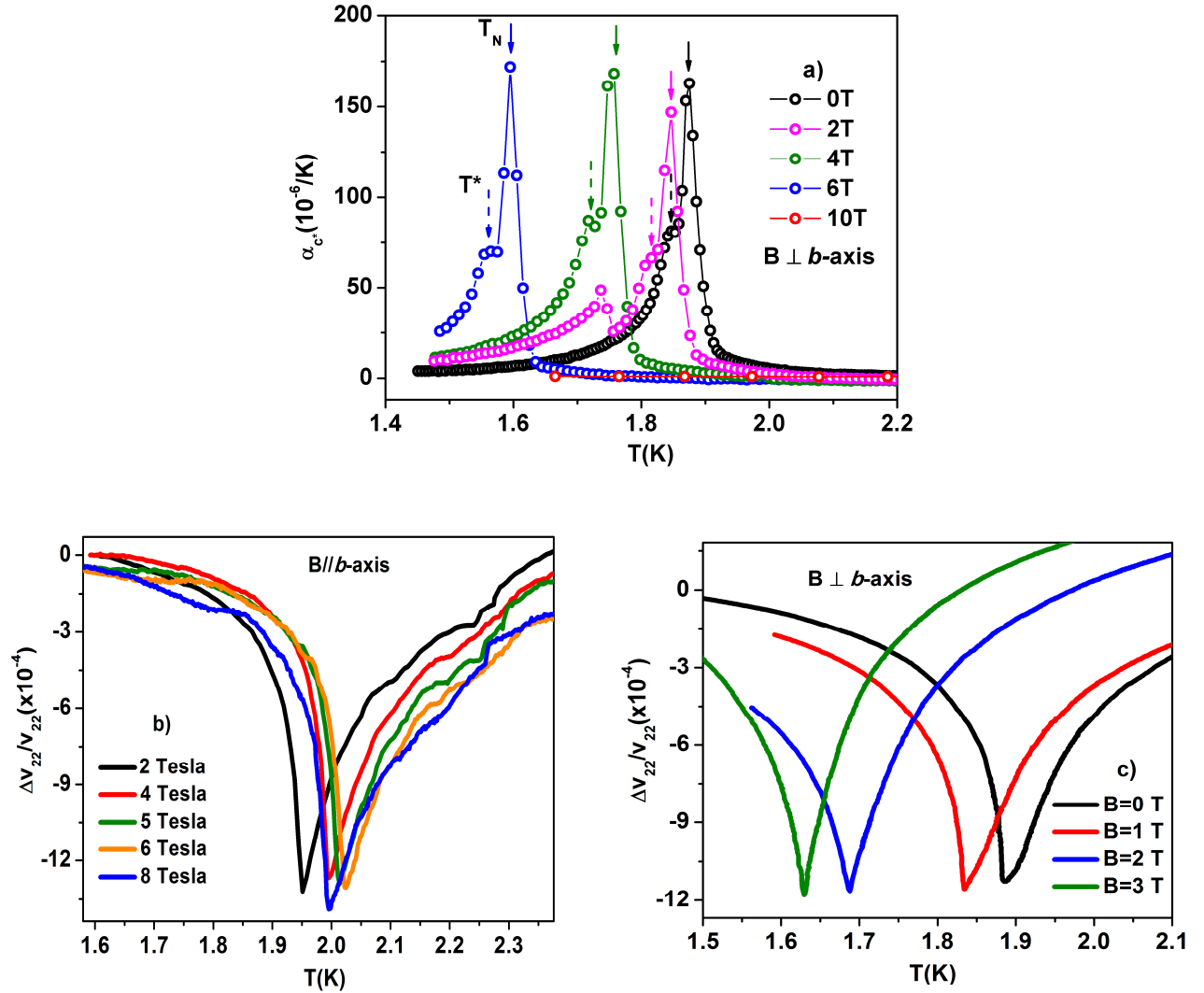
Figure 4.11 *a) Uniaxial expansitivity along the b-axis as a function of temperature at different applied magnetic fields (B $\perp$ b-axis). Solid arrows mark the AFM transition (T_N) and dashed arrows indicate yet another transition at T* (adapted from Ref. [Brüehl08]. b) and c) Temperature dependence of the relative change of the sound velocity at different magnetic fields (applied field parallel to b-axis in panel (b) and perpendicular to b-axis in panel (c)) in the vicinity of the AFM phase transition temperature.*

The first one is very sharp and located at T_N and the second one appears as a *kink-like* anomaly at slightly lower temperature T^*, as shown by solid arrows and dotted arrows in Fig. 4.11. With increasing magnetic fields, T_N and T^* shift to lower temperatures and become suppressed at fields above 10 T, consistent with the behavior of T_N obtained from sound velocity measurement in the same geometry, cf., Fig.4.11 (a) and (c). At present the microscopic mechanism of the second anomaly at $T^* < T_N$ is still unknown.
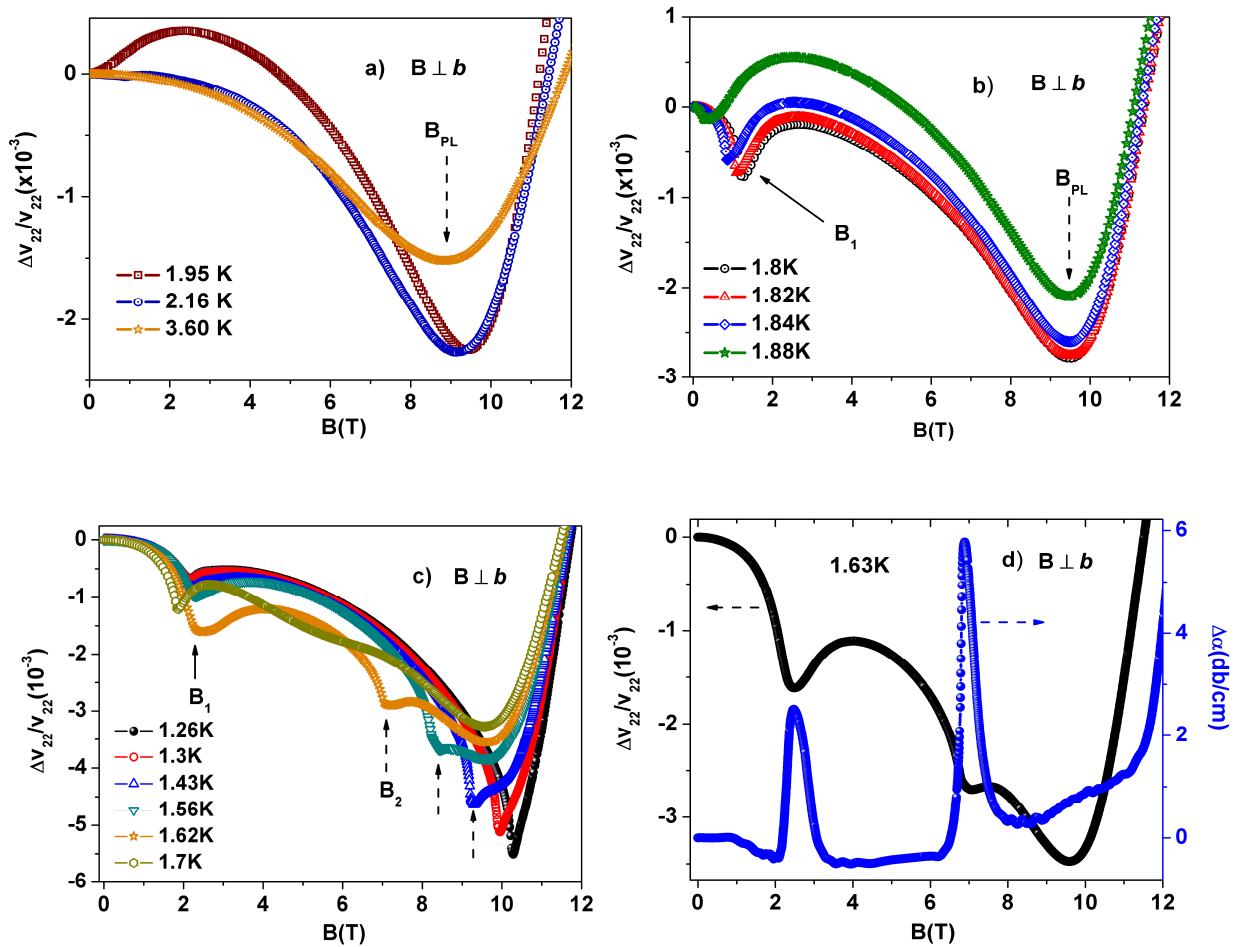
Figure 4.12 *Selection of data of $\Delta v_{22}/v_{22}$ as a function of magnetic field (B $\perp$ b-axis) at different temperatures in the range from 1.95 K to 3.6 K in panel (a), from 1.8 K to 1.88 K in panel (b) and from 1.26 K to 1.7 K in panel (c). Panel (d) exhibits the data of $\Delta v_{22}/v_{22}$ (left scale) and $\Delta\alpha$ (right scale) taken at 1.63 K. Solid arrows mark the AFM to SF (T < 1.6 K) or AFM to PM transition (T > 1.6 K) at B_1. Dashed arrows indicate the SF to PL (T < 1 K) or SF to PM (T > 1 K) transition at B_2. Field-induced plateau phase (B_{PL}) is pointed out by dotted vertical arrows*

Another interesting result comes from the temperature dependence of the sound velocity at zero fields. As displayed in Fig. 4.7(a), after the sharp anomaly at T_N, the data exhibit another pronounced softening of $c_{22}(T)$ when the system is cooled to very low temperatures ($T < 0.45$ K). The onset of this softening coincides with an abrupt increase of $\chi_{mol}(T)$. Note that this softening of the elastic constant is of comparable size to the one observed at T_N. This finding suggests the presence of another, most likely magnetic phase transition at temperatures below 0.45 K. The different behavior of $c_{22}(T)$ at the two phase transitions (at T_N and at 0.45 K) indicates that different coupling schemes between the strain and the corresponding order parameters are realized here.

Fig. 4.12 shows the isotherm of the relative sound velocity change of $c_{22}(B)$ as a function of magnetic field applied perpendicular to the b-axis. The field orientation was close to the setting employed in Ref. [Love70]. For this field orientation, the 1/3 magnetization plateau is reached above 10 T [Kikuchi05a]. Fig. 4.12(a) displays a selection of data taken outside the ordered phase, *i.e.*, from 1.95 K to 3.6 K. With increasing field, the data show a pronounced softening of the c_{22} mode representing the field-induced progressive canting of the monomers giving rise to paramagnetic-like behavior in the magnetization [Kikuchi05a]. Entering into the 1/3 plateau was marked by a well-defined anomaly around 10 T (B_L) as mentioned in *Sec. 4.4.2*.

Inside the low-temperature long-range-ordered phase, the ultrasound measurements display a more complex behavior. As exhibited in Fig. 4.12(b), (c) and (d), we find several distinct anomalies which become more pronounced and develop a fine structure with decreasing temperature. As already reported in chapter 2, the ultrasonic attenuation $\Delta\alpha$ changes abruptly or exhibits an anomaly, whereas the elastic constant exhibits an anomaly at the magnetic phase transition as one can see in the Fig. 4.12(d), an example of a measurement of $\Delta v/v$ and $\Delta\alpha$ as a function of magnetic field performed at 1.63 K. The first feature at around $B = 2$ T (B_1), shown in Fig. 4.12(b) and (c) by solid arrows, was assigned in Ref. [Love70] to the transition from the antiferromagnetic to the SF state (for $T < 1.6$ K) or the paramagnetic (PM) state (for $T > 1.6$ K), cf. Fig. 4.14(b). At the temperature 1.3 K $< T <$ 1.6 K, the second feature appears at the field between 2 T and 10 T (B_2) in Fig. 4.12(c), indicated by the dashed arrow, which is attributed to the transition from the SF state, either to the plateau state (PL) via the PM state ($T > 1$ K) or directly into PM state ($T < 1$ K). Upon decreasing temperature, this second feature becomes sharper and has the tendency of merging with the anomaly that characterizes the field-induced transition to the plateau state at low temperature. A precise mapping of the field *vs.* temperature phase diagrams from the various temperature- and field-

dependent measurements suggests that exiting from the AF ordered phase (for B // b-axis) or SF phase (for $B \perp b$-axis) merges with the entrance into the 1/3 ordered plateau phase at low temperatures, cf. Fig. 4.14 (a) and (b).
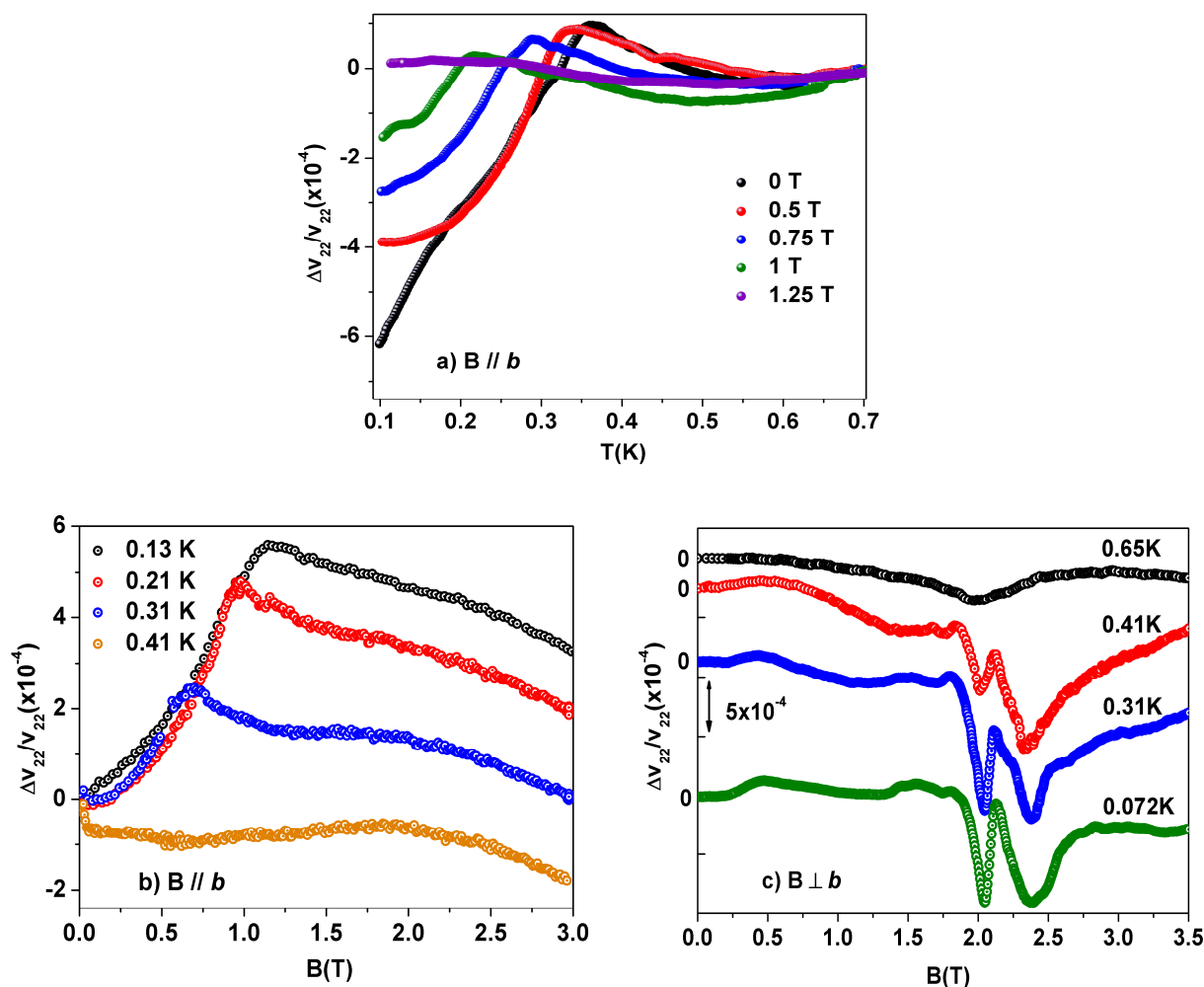
Figure 4.13 a) Temperature dependence of $\Delta v_{22}/v_{22}$ in various applied fields (B // b-axis). b) $\Delta v_{22}/v_{22}$ as a function of field (B $\perp$ b-axis) at various fixed temperatures. c) $\Delta v_{22}/v_{22}$ as a function of field at constant temperatures (B // b-axis).

In order to obtain more information on the very low-temperature region ($T < 0.5$ K), the field (temperature) dependence of v_{22} at various fixed temperatures (fields) has been determined and is displayed in Fig. 4.13. The temperature dependence of v_{22} at different applied fields B // b-axis is shown in Fig. 4.13(a). The onset temperature of the softening gradually shifts to lower temperature

with increasing field. No softening can be observed within the accessible temperature range $T \geq 0.08$ K for $B \geq 1.25$ T. These observations still remain valid when the magnetic field is applied perpendicular to b-axis (not shown here). Fig. 4.13 (b) displays a selection of field sweeps for B // b-axis measurements. A pronounced increase of v_{22} is observed at very low temperature of 0.13 K upon increasing the field. At a field of 1.15 T, this increase is abruptly terminated and c_{22} starts decreasing with further increasing field. The position of this kink in v_{22} is shifted to the lower fields with increasing temperatures. Above the temperature $T = 0.41$ K, however, this anomaly can no longer be discerned.
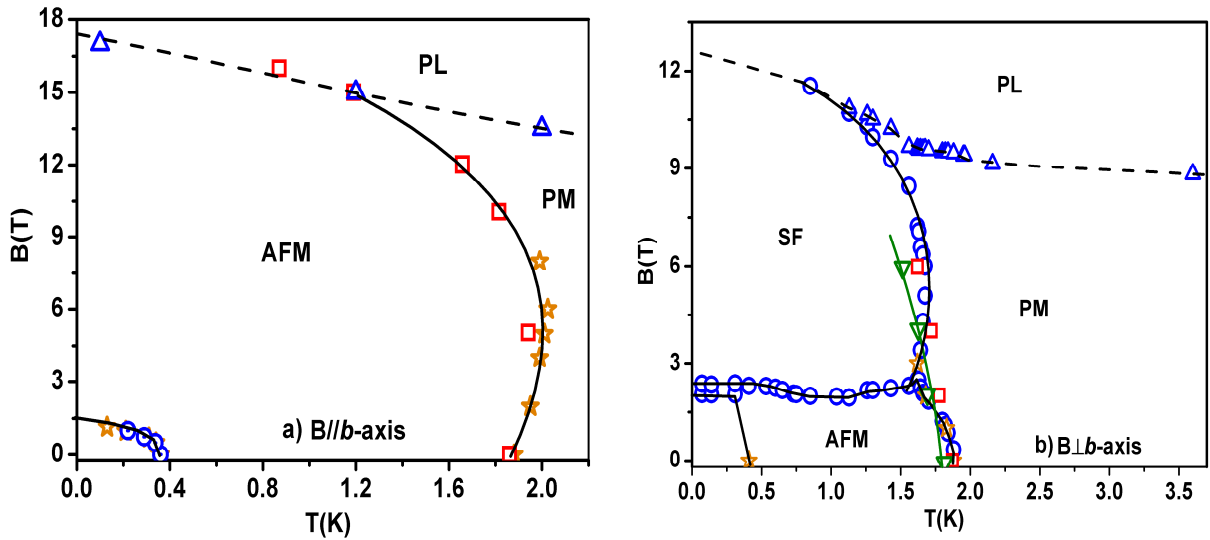
Figure 4.14 *B-T phase diagram for the field applied parallel (a) and perpendicular (b) to the b-axis. Phase boundaries (solid lines) are constructed from the anomalies of the temperature dependence of thermal expansion (open red squares, at T_N, and down green triangles, at T^*) sound velocity (open orange stars) and the field dependence of the sound velocity (open blue circles, at B_1 and B_2) measurements. The crossover-phase boundaries (broken lines) from AFM and PM (B // b) or SF and PM (B $\perp$ b) to the PL state are determined from the field dependence of the sound velocity and the thermal expansion [Wolff-Fabris09] at $B_{PL.}$*

Fig. 4.13(c) shows details of some selected low-field sweep data from 0.072 K to 0.65 K. At temperatures above 0.45 K, a single feature of the field-induced AFM to SF phase transition is observed around 2 T. For $T < 0.45$ K, however, the data reveal a splitting into two closely-spaced

features. Note that these features for $B \perp b$ occur in the same temperature region where the large softening was observed in $c_{22}(T)$, cf. Fig. 4.7(a), and have the same size as the elastic anomaly at the AFM phase transition. There is no doubt that these observations indicate the existence of an unknown phase boundary at very low temperatures. More detailed studies at very low temperatures should elucidate this phenomenon.

Finally we construct the detailed low-temperature B-T phase diagrams for $B \mathbin{/\mkern-5mu/} b$ and $B \perp b$, shown in Fig. 4.14(a) and (b), from the anomalies of temperature- and field-dependent of the sound velocity and thermal expansion measurements. The B-T phase diagram shows that the low temperature state of Azurite is more complex than was previously thought. These observations imply the action of further interactions such as anisotropic exchange interaction, Dzyaloshinskii-Moriya interactions or structural distortions leading to a change of the magnetic exchange coupling. These effects should be taken into account in a microscopic model that accounts for the low-temperature properties of this material.

5

THE QUASI-2D SPIN-1/2 HEISENGERG AFMs Cs$_2$CuCl$_4$ and Cs$_2$CuBr$_4$

This chapter presents the results of ultrasound measurements carried out on single crystals of the quasi-2D antiferromagnetic quantum magnets Cs$_2$CuCl$_4$ and Cs$_2$CuBr$_4$. Our aim is to study the interaction of the acoustic wave with the spin lattice at the field-induced phase transitions and the interplay of the spin-lattice interaction and the quantum-critical behavior in these low-dimensional spin systems.

5.1 Introduction

For more than a decade, the frustrated antiferromagnets Cs$_2$CuCl$_4$ and Cs$_2$CuBr$_4$ have been considered as experimental realizations of a frustrated triangular lattice [Coldea96, Tanaka02]. Of particular interest in these systems are the anomalous physical properties resulting from the interplay of strong quantum fluctuations and geometric frustration [Lee10, Sebastian06 and Batista07]. Both systems are characterized by a layered arrangement of Cu^{2+} ions in a triangular pattern parallel to the *bc*-plane [see Fig.5.1]. The two-dimensional character of the magnetic interactions between the spin-1/2 Cu^{2+} ions was confirmed by neutron-scattering and susceptibility measurements in both systems [Coldea03, Tsujii07] and was successfully modeled [Coldea03, Zheng05] by a two-dimensional Heisenberg Hamiltonian that contains a small anisotropic interaction term of the Dzyaloshinskii-Moriya (DM) type. In spite of their structural similarity, Cs$_2$CuCl$_4$ and Cs$_2$CuBr$_4$ have rather different magnetic behavior.

Cs$_2$CuCl$_4$ has attracted much attention due to its spin-liquid properties [Coldea02, Coldea01] and its field-induced quantum phase transition around B_s ~ 8.5 T, separating long-range antiferromagnetic order below T_N and $B \leq B_s$ from a fully-polarized ferromagnetic state at $B > B_s$. At a field $B = B_s$, the antiferromagnetic order is suppressed to $T_N = 0$, which constitutes a quantum-critical point (QCP). The B dependence of the field-induced AFM phase transition near the QCP can be described by a power-law and interpreted as BEC of magnons. Anomalous physical properties, even at finite temperatures, are expected to be observed around B_s as a consequence of the underlying quantum phase transition. A topic of high current interest for this compound is the

question concerning the interplay of spin-lattice interactions and quantum criticality, especially as to what extent a strong spin-phonon interaction may modify the quantum-critical behavior.

On the other hand, for Cs_2CuBr_4, quantum-fluctuation-assisted 1/3 and 2/3 magnetization plateaux were observed in magnetic fields around 14 T and 23 T at temperatures $T < T_N = 1.4$ K. Here, the field-induced incommensurate–commensurate transitions occur at both ends of the plateau [Ono03]. For Cs_2CuBr_4, we attempt to study the interaction of the acoustic wave with the spin lattice at the field-induced plateau phase transitions. Moreover, the observed BEC in Cs_2CuCl_4 and field-induced plateaux in Cs_2CuBr_4 reflect the dominant repulsive and kinetic energy of the magnetic excitations, respectively. For our study in these compounds, a first step will be to explore the effects of confinement of the motion of the Bosons to the underlying crystal lattice.

5.2 Crystal structure

Cs_2CuCl_4 and Cs_2CuBr_4 have the β-K_2SO_4-type crystal structure as shown in Fig. 5.1(a). The unit cell contains four Cu^{2+} surrounded by the tetrahedra of the chlorine atoms and arranged in the bc-plane.

a)   b)
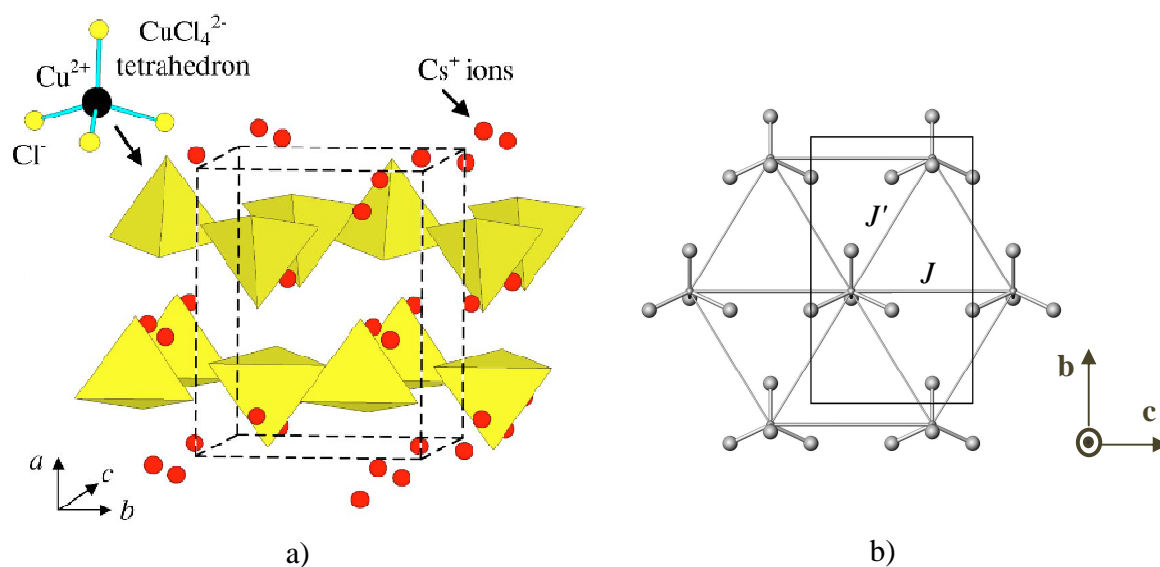
Figure 5.1 (a) Crystal structure of Cs₂Cu(Cl,Br)₄ showing the Cu(Cl,Br)₄ tetrahedra arranged in layers (bc-plane). (b) Magnetic exchange paths in the (bc) layer which form a two-dimensional anisotropic triangular lattice (reprinted from Ref. [Coldea03]).

The magnetic ions are Cu^{2+} carrying a spin 1/2 and forming a triangular arrangement with non-equivalent exchange couplings J and J' as indicated in Fig. 5.1(b). The adjacent bc-plane are separated from each other by Cs$^+$-ions.

The ratio J'/J controls the properties of the system. If $J'/J = 0$ the system can be regarded as an assembly of four decoupled spin chains passing through the unit cell, along the b-axis. If $J'/J = 1$ or $0 < J'/J < 1$ the system is fully frustrated or partially frustrated, respectively. Cs$_2$CuCl$_4$ and Cs$_2$CuBr$_4$ fall into the class of quasi-two-dimensional (quasi-2D) frustrated spin systems with $J'/J = 0.342$ and 0.74, respectively [Coldea02, Ono03]. More details about the crystal structure and its role on the magnetic properties will be discussed in chapter 6.

5.3 The quasi-2D quantum-spin system Cs$_2$CuCl$_4$

5.3.1 Magnetic properties and phase diagram

The Cs$_2$CuCl$_4$ system is a spin-1/2 AFM on a frustrated triangular lattice so that the quantum fluctuations are strong and also enhanced by the low dimensionality. Neutron scattering measurements on Cs$_2$CuCl$_4$ showed considerable dispersion in the bc-plane indicating a strong 2D character of the system [Coldea02]. These observations constrast with earlier studies [Coldea97], which proposed a quasi-1D picture based on estimates of the interchain couplings. Zero field measurements below $T_N = 0.6$ K showed magnetic ordering in the form of an incommensurate spiral due to the frustrated couplings, with the ordering wavevector Q = (0.5 + ε_0)b* and the incommensuration relative to Néel order $\varepsilon_0 = 0.03$. The incommensurate ordering wavevector and the excitation energies are strongly renormalized compared to their classical values, indicating large quantum fluctuations in the ground state [Coldea01]. The spin excitation spectrum measured by neutron scattering experiments shows extended excitation continua, and several theoretical approaches have been put forward to explain this observation in terms of fractional-spin excitations of a proximate spin-liquid state [Coldea02]. In fact, Cs$_2$CuCl$_4$ is one of the first quasi-2D spin-1/2 Heisenberg antiferromagnets where dominant excitation continua, characteristic of fractionalization of spin-1 spin waves into pairs of deconfined spin-1/2 spinons, were observed [Coldea03, Coldea01], instead of sharp spin-wave excitations.

Neutron scattering measurements [Coldea02] at high fields above the ferromagnetic saturation were used to determine the full spin Hamiltonian. It can be written as:

$$H = H_0 + H_{DM} + H_Z. \qquad (5.1)$$

The first term is the usual symmetric Heisenberg exchange Hamiltonian:

$$H_0 = \sum_R J S_R \cdot S_{R+\delta_1+\delta_2} + J'\left(S_R \cdot S_{R+\delta_1} + S_R \cdot S_{R+\delta_2}\right) + J'' S_R \cdot S_{R+\delta_3} \qquad (5.2)$$

where S_R represents the spin-1/2 operator at site R, δ_1 and δ_2 denote the in-plane nearest-neighbor vectors and δ_3 the out-of-plane nearest-neighbor vector connecting spins on adjacent layers, as shown in Fig 5.2. The main exchanges form a two-dimensional triangular lattice with spatially anisotropic couplings as shown in Fig. 5.1(b) with $J = 0.374(5)$ meV for the spin chains along the b-axis, $J'/J = 0.34$ for the zig-zag bonds between the chains in the bc-plane and the interlayer coupling was estimated to $J''/J = 0.045$.

The second term is the Dzyaloshinskii-Moriya (DM) Hamiltonian:

$$H_0 = \sum_R D S_R \times \left(S_{R+\delta_1} + S_{R+\delta_2}\right) \qquad (5.3)$$

where **D** is known as the DM vector. This spin exchange anisotropy [Radu07] is due to a significant spin-orbit coupling combined with sufficiently low crystal symmetry. The DM vector in Cs$_2$CuCl$_4$ is found to be **D** $= ((-1)^n D, 0, 0)$, along the zigzag bonds, with D $= 0.235$ K [Coldea03] (the factor $(-1)^n$ indicates that the DM vector changes direction from one plane to the other).
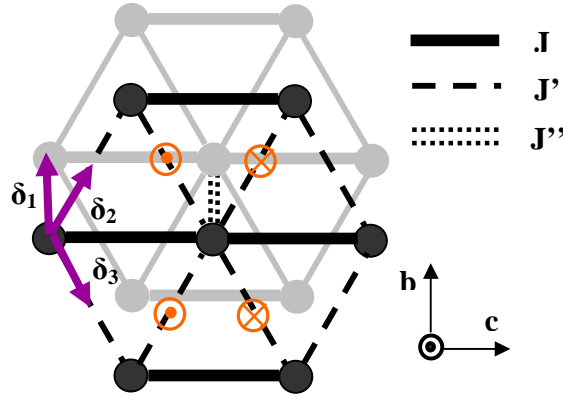

Figure 5.2 *Representation of two consecutive Cu planes showing their relative offset and the orientation of the exchange coupling constants J, J' and J''. The vectors δ_i, used to describe the Hamiltonian Eq. 5.2, are shown by the purple arrows, and the direction of the DM vector D of Eq. 5.3, by the orange symbols.*

Finally, the Zeeman Hamiltonian accounting for the energy of the spins in an applied magnetic field B, where g is the g-factor and μ_B, the Bohr magneton, is:

$$H_Z = -\sum_R g\mu_B B \cdot S_R \,.$$

An adaptation of the T vs B phase diagram of Tokiwa *et al.* [Tokiwa06] and T. Radu *et al.* [Radu05] is presented in Fig 5.3 for the field applied along the principal crystallographic *a*-axis. Open red diamonds, connected by the blue dashed line, indicate the maximum in the temperature dependence of the susceptibility curves that represent the crossover phase boundary between the spin liquid (SL) and the paramagnetic (PM) state. Black solid circles connected by the black solid line, are combining data points from bulk magnetization, specific heat [Tokiwa06] and neutron scattering [Coldea01] experiments reflecting the AFM phase boundary.
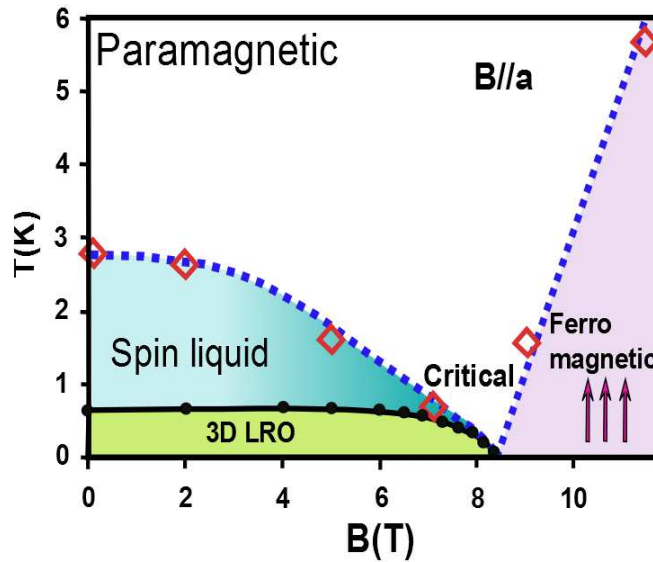
Figure 5.3 *Phase diagram of Cs$_2$CuCl$_4$ along the principal crystallographic a-axis. The lines connecting the data points are meant as a guide to the eyes (adapted from Ref. [Coldea03]).*

The magnetic susceptibility measurement shows that upon lowering the temperature, the spin system undergoes a crossover/transition at T_{max} from a paramagnet into a spin liquid where antiferromagnetic short-range correlations become non-negligible. It is found that T_{max} decreases as the magnetic field is increased and disappears before the saturation field B_s is reached, cf. Fig 5.3. This indicates that the short-range correlations are effectively suppressed by the application of a magnetic field. Note that the available experimental data points provide only an approximate curve

for the boundary between the paramagnet and the spin liquid phase (dashed line). More detailed data are needed to complete the phase diagram, especially close to the tri-critical point, where the spin-liquid phase, the ordered phase and the paramagnetic phase meet. Upon further lowering the temperature without applying field, the spin-liquid phase transits into a long-range ordered phase at the Néel temperature, $T_N = 0.62$ K. The spiral state in zero field is stable down to the lowest temperatures investigated ($T = 50$ mK) and thus is presumed to be the ground state of the system.

A global characteristic of the long-range ordered (LRO) region in the phase diagrams is that it shows a strong anisotropy depending on the direction of the applied magnetic field, as opposed to the more isotropic behavior, characteristic of the spin-liquid region. Indeed, for fields applied along the a-axis, only one phase, a spin-cone state, is stable up to the saturation field, while a cascade of phase transitions is seen for fields applied in the bc-plane (not shown here). Moreover, using the field along the a-axis to control the excitations, intensive studies by means of neutron scattering [Coldea01], specific heat [Radu05] and magnetocaloric [Radu07] measurements suggested that the field-induced magnetic phase transition for that particular field direction can be understood as a Bose-Einstein condensation of magnons. As the applied field approaching B_s, T_N is suppressed to $T_N = 0$, constituting a quantum critical point (QCP). At the QCP, quantum-critical fluctuations are expected to give rise to anomalous physical properties also at finite temperatures.

As stated in the introduction, with the aim to learn more about the interplay of spin-lattice interaction and quantum criticality, especially to what extent a strong spin-phonon interaction may modify the quantum-critical behavior, we have used ultrasonic measurements to explore the phase diagrams for B // a-axis by all three principal modes c_{11}, c_{22} and c_{33}.

5.3.2 Sample preparation

Large and high-quality single crystals of Cs_2CuCl_4, grown from aqueous solutions by an evaporation technique, see chapter 6 and Ref. [Krüger10] for details, were used for the experiments. Piezoelectric film transducers have been glued to the surfaces parallel to the *(bc)*, *(ac)* and *(ab)* crystallographic planes of the samples that respectively correspond to the longitudinal c_{11}, c_{22} and c_{33} acoustic modes as displayed in Fig 5.4(a).

The magnetic field was always applied along the a-axis so that the phase diagram shown in Fig. 5.3 applies. The sizes of the samples were about 4 x 4.5 x 5 mm^3. The arrangement of the sample in the sample holder is shown in Fig. 5.4(b). The measurements were performed at a

frequency of 75 MHz. The absolute value of the sound velocity at room temperature has been determined to $v_{11}(300K) = (2603 \pm 20)$ m/s which agrees well with the previously reported value in Ref. [Tylczyński92].
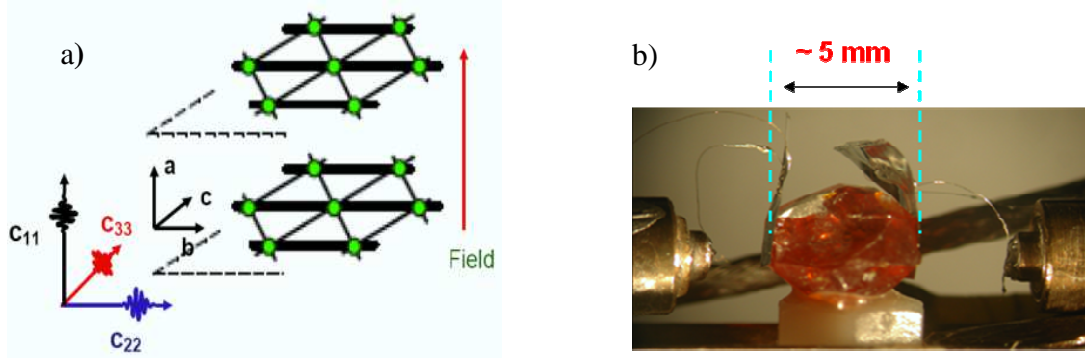

Figure 5.4 *a) Scheme indicating the propagation of the longitudinal modes with respect to the magnetic layers. The c_{11}, c_{22}, c_{33} respectively correspond to propagation along the a, b and c-axis, respectively. The magnetic field was applied along the a-axis in all three cases. b) Arrangement of the Cs_2CuCl_4 crystal with transducers in the sample holder.*

5.3.3 Results and discussion

a) Temperature dependence

Fig. 5.4 (a) presents the temperature dependence of the elastic constant $c_{11}(T)$ measured at zero field over the whole temperature range together with the elastic background obtained by applying Eq. 2.11. The elastic constant grows linearly with decreasing temperature and does not reveal any anomalies down to low temperatures.

At low temperature, the c_{11} mode reveals a broad maximum and a softening below about 7 K. In addition, the attenuation also shows a broad maximum at a temperature slightly higher than the one of c_{11}. This broad maximum is interpreted as a crossover from a paramagnetic to a spin-liquid state, with well developed short-range AFM spin-spin correlations [Coldea02], similar to the case of Azurite (see chapter 4). The position of this broad maximum changes only slightly when magnetic fields are applied. At higher fields the peak becomes broader. The broad maximum is probably still there even for $B > 4$ T but the location of the maximum, T_{max}, is difficult to determine because the high-temperature tail of the sharp AFM phase transition at lower temperatures overlaps with the low-

temperature tail of the broad peak. Therefore, from our measurements, it is hard to extract the evolution of this feature with magnetic field.
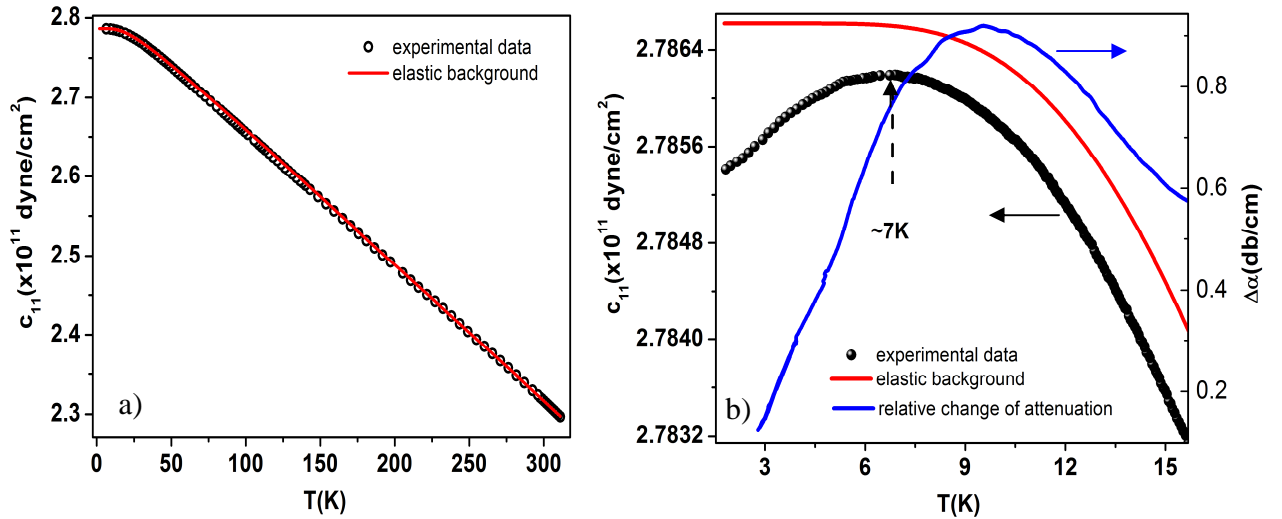

Figure 5.4 *a) Temperature dependence of the elastic constant for the acoustic c_{11} mode in zero field measured at 75 MHz with elastic background (red full curve) obtained by fitting with Eq. 2.11. b) The softening of the c_{11} at low temperatures (left axis) deviates from the elastic background. Relative change of the sound attenuation (blue curve) is shown in right axis.*

Upon further cooling the sound velocity shows a small kink at $T_N \sim 0.6$ K marked by a dashed arrow in Fig. 5.5(a), indicating the transition to 3D long-range magnetic order where the magnetic structure found by neutron diffraction is a spiral in the *bc*-plane [Coldea96]. This transition temperature is changed slightly in fields below 6 T (cf. Fig. 5.5(a)). However, it varies very strongly above 6 T. As shown in Fig. 5.5(b), with increasing field the *kink-like* anomaly in the sound velocity becomes more pronounced and changes to a *step-like* anomaly. This is accompanied by an increase in the size of the softening and a rapid shift of the position to lower temperatures. T_N is reduced dramatically, adopting $T_N = 0.2(2)$ K at 8.2 T, for example, nearly three times smaller than its value in zero field.

An extraordinary change occurs as the system approaches the QCP by increasing the field from 8.4 T to 8.5 T (see of Fig. 5.5(c)). In this fields regime, the sound velocity starts decreasing below the temperature around 0.2 K. No further evidences of the transition can be resolved from our data upon decreasing to the lowest temperature. In this tiny field change ($\Delta B/B < 1.3\%$), the softening is

gradually suppressed and disappears around the QCP. As seen in Fig 5.5(c), at 8.5 T, the sound velocity exhibits a monotonic increase linear in T down to the lowest temperature. With the applied fields of 9 T or 10 T, as the system enters the fully-polarized state, the temperature dependence of the sound velocity displays the typical variation that shows a very small change of elastic constants at very low temperature, as illustrated in Fig. 5.5(d).

Figure 5.5 *Temperature dependence of the relative change of the sound velocity for the acoustic c$_{11}$ mode at very low temperatures in various applied fields.*

Figure 5.6 shows the temperature dependence of the c_{22} (panel a) and c_{33} (panel b and c) modes. The same behavior as the c_{11} mode remains valid for the c_{22} and c_{33} modes at the applied fields below 8 T meaning that the sound velocity shows a softening and reveals a *kink-like* anomaly at the

AFM phase transition. With increasing the applied fields, the phase transition becomes more pronounced and changes from a *kink-like* to a *step-like* anomaly accompanied by an increase in the size of the softening. The difference occurs as the field approaches the QCP. Instead of being suppressed to a linear curve, the c_{22} and c_{33} keep showing the steep softening at the critical field. By increasing the applied field above B_s, the softening is gradually suppressed, similar with the observation in the c_{11} mode. Note that there is a small difference in the value of the critical field B_s and a difference in the size of the softening for the different modes. The former may be caused by the difference of the *g*-factor and the miss-alignment of the applied field direction to the crystal-axis. The latter one concerns the magneto-elastic couplings, to be discussed in more detail below.

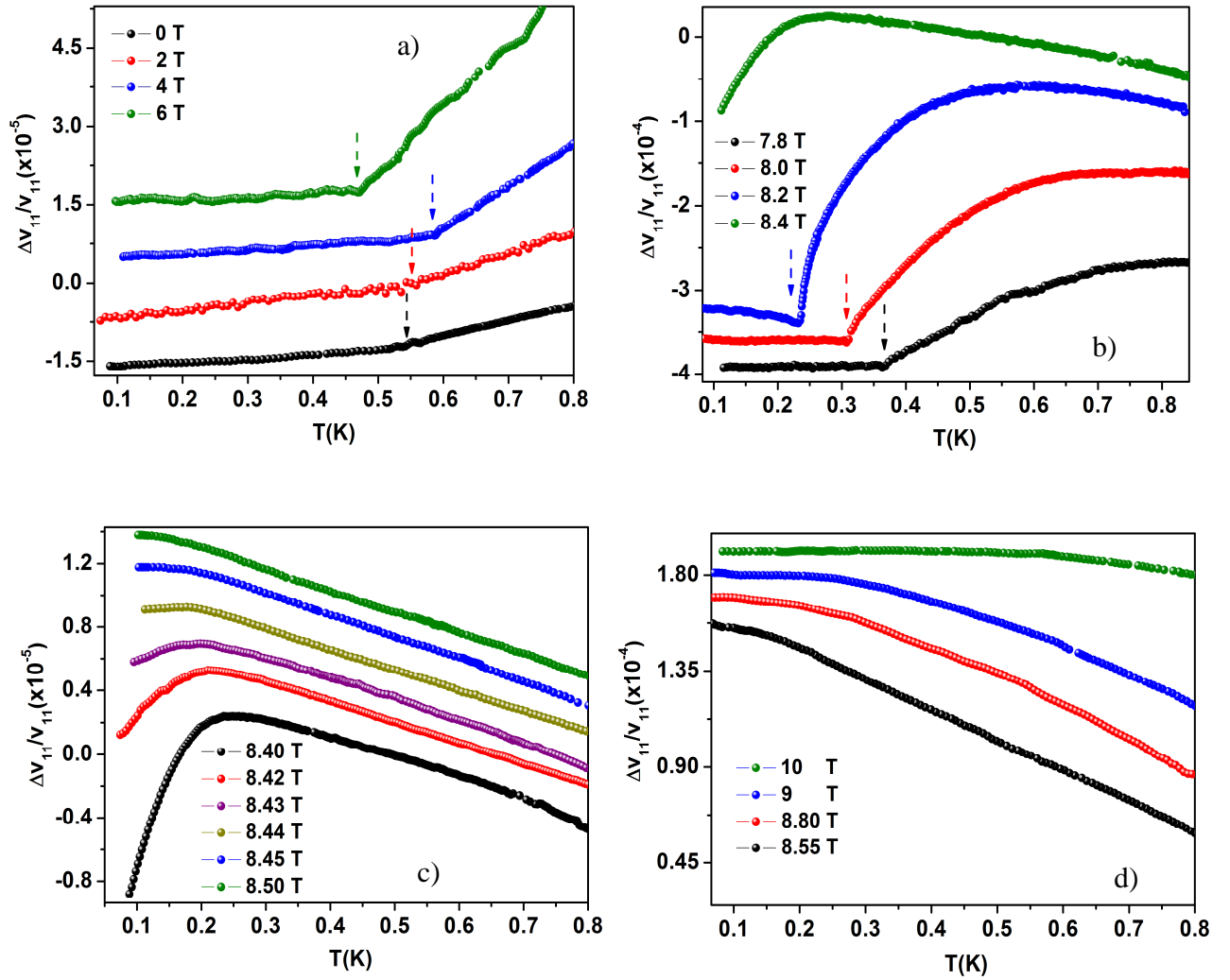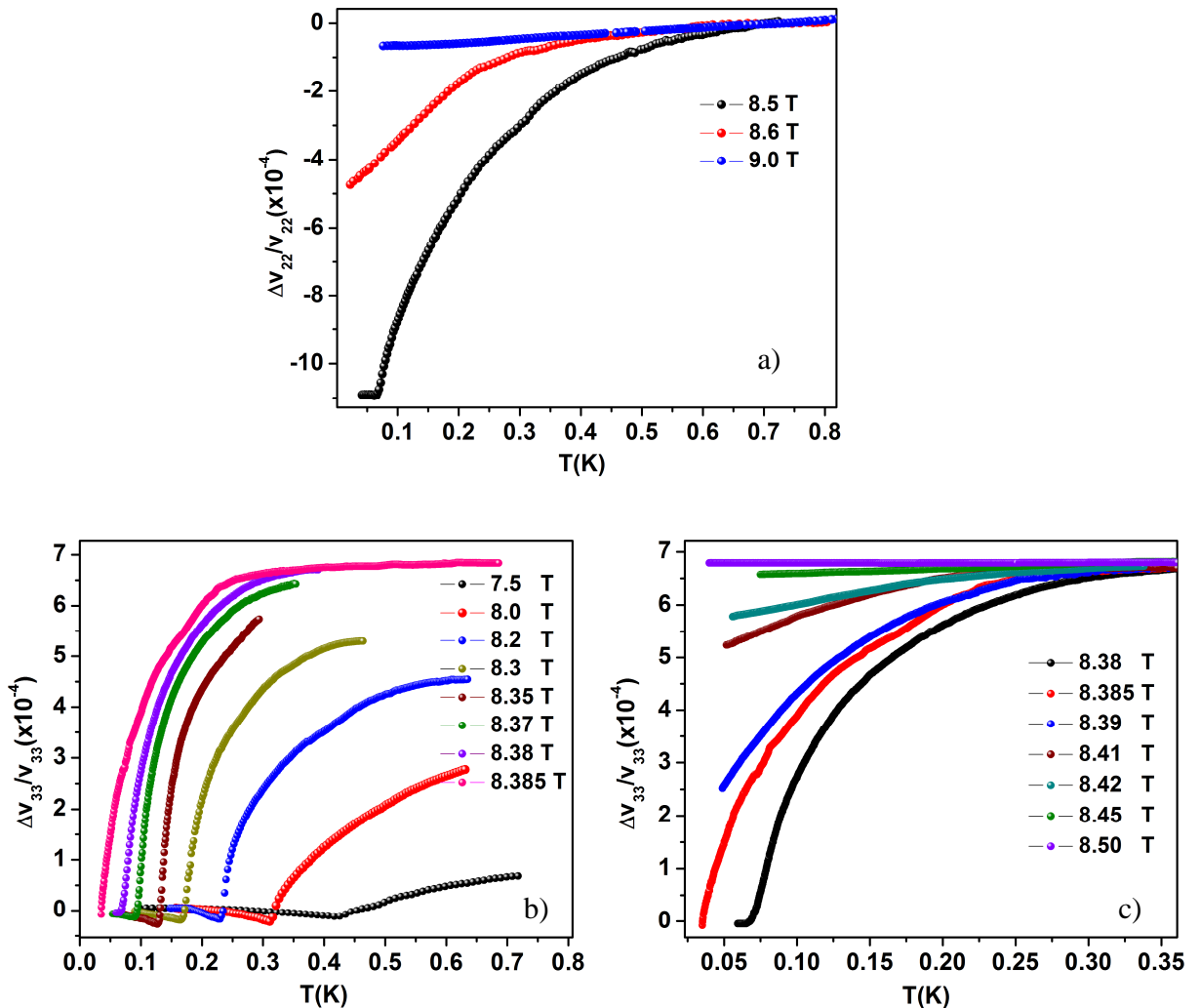***Figure 5.6*** *Temperature dependence of the relative change of the sound velocity at very low temperatures in various applied fields for the c_{22} mode (panel a) and the c_{33} mode (panel b and c).*

b) Field dependence

Fig. 5.7 presents the magnetic field dependences of the acoustic characteristics of the c_{11} mode, measured at various constant temperatures ranging from above to below T_{max} (the characteristic temperature which marks the formation of the spin-liquid state). Fig 5.7 (a) shows the field dependence of the relative change of the sound velocity. The common feature of the curves is that the sound velocity exhibits a hardening of the lattice stiffness with increasing field. At temperatures above T_{max}, the sound velocity gradually increases with increasing field even when the applied field reaches the saturation B_s. Below T_{max}, anomalies develop in the vicinity of the saturation field (cf. inset of Fig. 5.8 a) and, as the system enters the fully-polarized state, the sound velocity almost does not change with increasing field. The sound attenuation, shown in Fig. 5.7 (b), displays a broad feature around B_s at $T > T_{max}$ developing into a pronounced anomaly when the temperature decreases to below T_{max}, consistent with the position of the anomaly observed in the sound velocity. This anomaly shifts to higher field with decreasing the temperature, as illustrated by the dashed-line in Fig. 5.7(b).
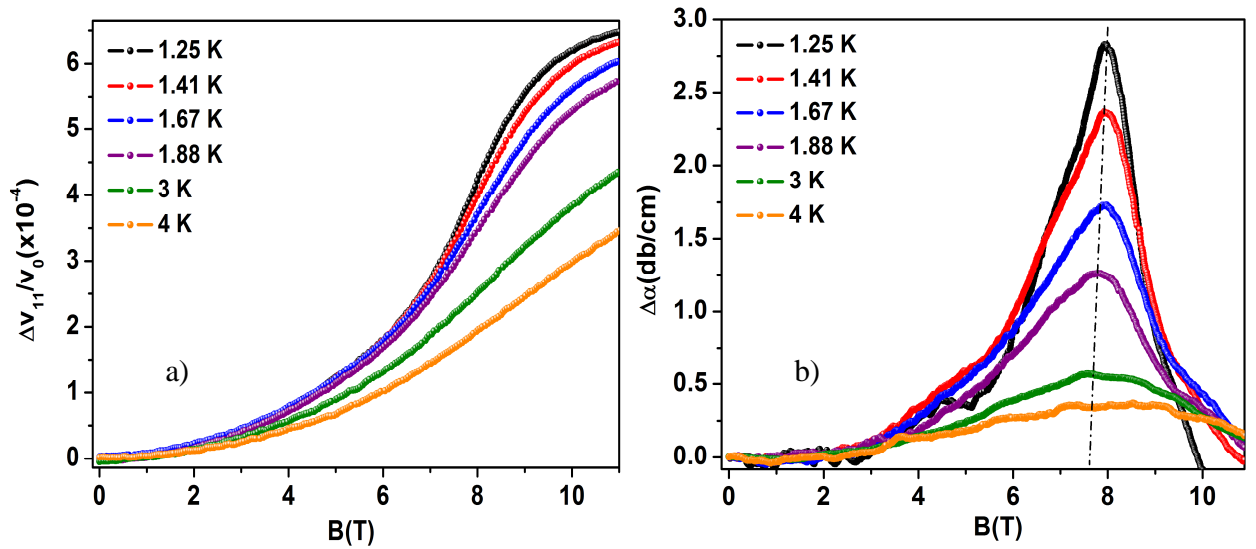
Figure 5.7 *Field dependence of the relative change of the sound velocity (panel a) and sound attenuation (panel b) of the c$_{11}$ mode at various constant temperatures in the spin-liquid phase.*

Fig. 5.8 shows some selected data of the magnetic field dependence of the relative change of the sound attenuation (main panel) and sound velocity (inset) for the c_{11} (panel a), c_{22} (panel b) and c_{33} (panel c) mode for the temperature regimes just above and below T_N. As pointed out above, the

82

sound attenuation shows a broad anomaly when the field crosses B_s, consistent with the anomaly observed in the sound velocity. Both anomalies become more pronounced and develop a fine structure on decreasing temperature. The shape of the attenuation curves change dramatically when the temperature decreases to below T_N (inside the ordered state). The attenuation stays nearly constant in the low field regime. As the field passes through the AFM boundary, the attenuation abruptly rises up exhibiting a steep and sharp anomaly. Its position now is strongly temperature dependent. The change in the shape of this anomaly can be considered to be the point at which the crossover/transition of the system from a 2D spin-liquid to a 3D long-range ordered state happens.
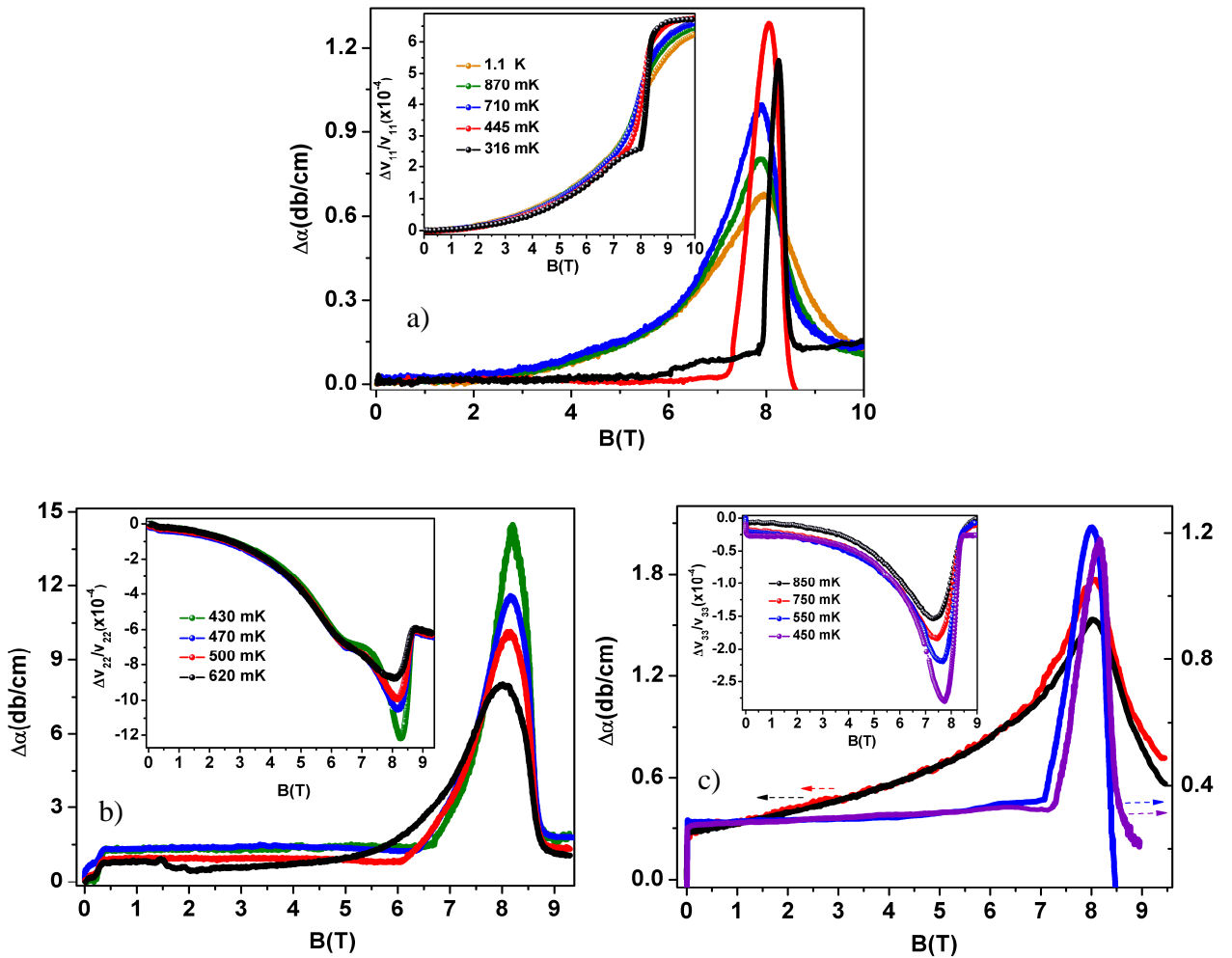

Figure 5.8 *Field dependence of the relative change of the sound attenuation (main panels) and the sound velocity (insets) at various constant temperatures above and below T_N of the c_{11} (panel a), c_{22} (panel b) and c_{33} (panel c) modes.*

As already introduced in Chapter 2, in magnetic insulators, the coupling between a sound wave and the magnetic system is usually of exchange-striction type. The magnetoelastic coupling constants are proportional to the strain derivative of the magnetic exchange couplings.

Figure 5.9 displays representative field-induced changes of the sound velocity at around 0.12 K of all three longitudinal modes c_{11}, c_{22} and c_{33} which modulate three magnetic exchange coupling J'', J and J', respectively. The c_{22} mode which modulates the dominant magnetic coupling constant J along the b-axis, exhibits the largest softening (indicated by the length of the blue arrow) at B_s. This softening is twice as large as the one denoted c_{33} (red arrow) and nearly seven times larger than the c_{11} mode (black arrow). On the other hand, as expected, the corresponding attenuation coefficient of the c_{22} mode also shows the largest anomaly at B_s (not shown here). The attenuation coefficients for the two other modes are about one order of magnitude smaller, cf. Fig. 5.11. This result consistent with quasi-two dimensional magnetic interactions in Cs₂CuCl₄.
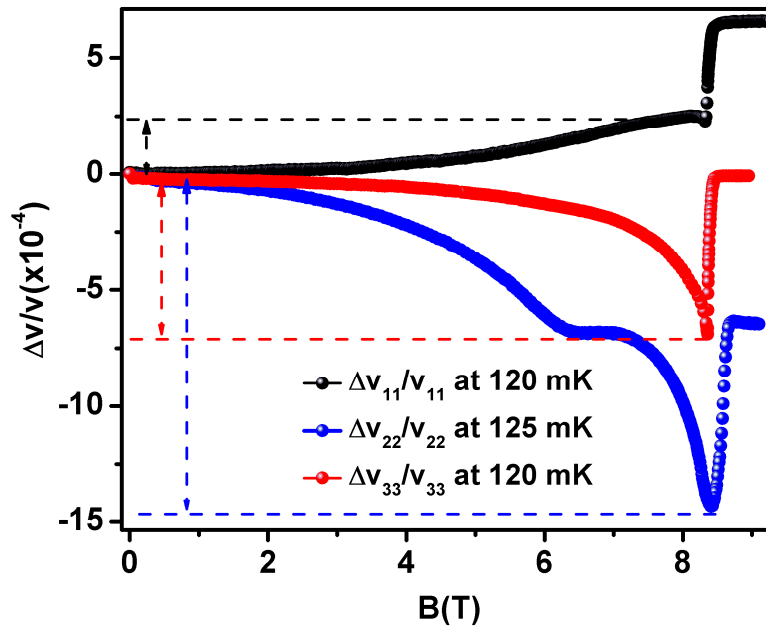
Figure 5.9 *Field dependence of the relative change of the sound velocity of the c_{11}, c_{22} and c_{33} modes at about 120 mK.*

The observed results of the acoustic behavior are surprising as the system is deep inside the AFM long-range ordered state. For all three modes, we find a pronounced double-peak structure at B_s (cf. Fig. 5.10 and 5.11). One of the peaks is strongly temperature dependent and coincides with $T_N(B)$, whereas the second one is broader and located at slightly higher fields.

As an example, Fig. 5.10 presents the data of the c_{33} mode measured at 130 mK. Panel (a) shows the relative change of the sound velocity (right-axis) and the corresponding change of the sound attenuation (left-axis). In the vicinity of B_s, we observe a softening with increasing field in the sound velocity. This is followed by a steep increase at B_s and a further hardening for $B > B_s$. The latter feature, coinciding with the B-range where the broad attenuation peak occurs, is characterized by a reduced slope, where $\Delta v_{33}/v_{33}$ varies almost linearly with B. In the field-induced ferromagnetic state at $B > B_s$, the sound velocity is nearly field independent.
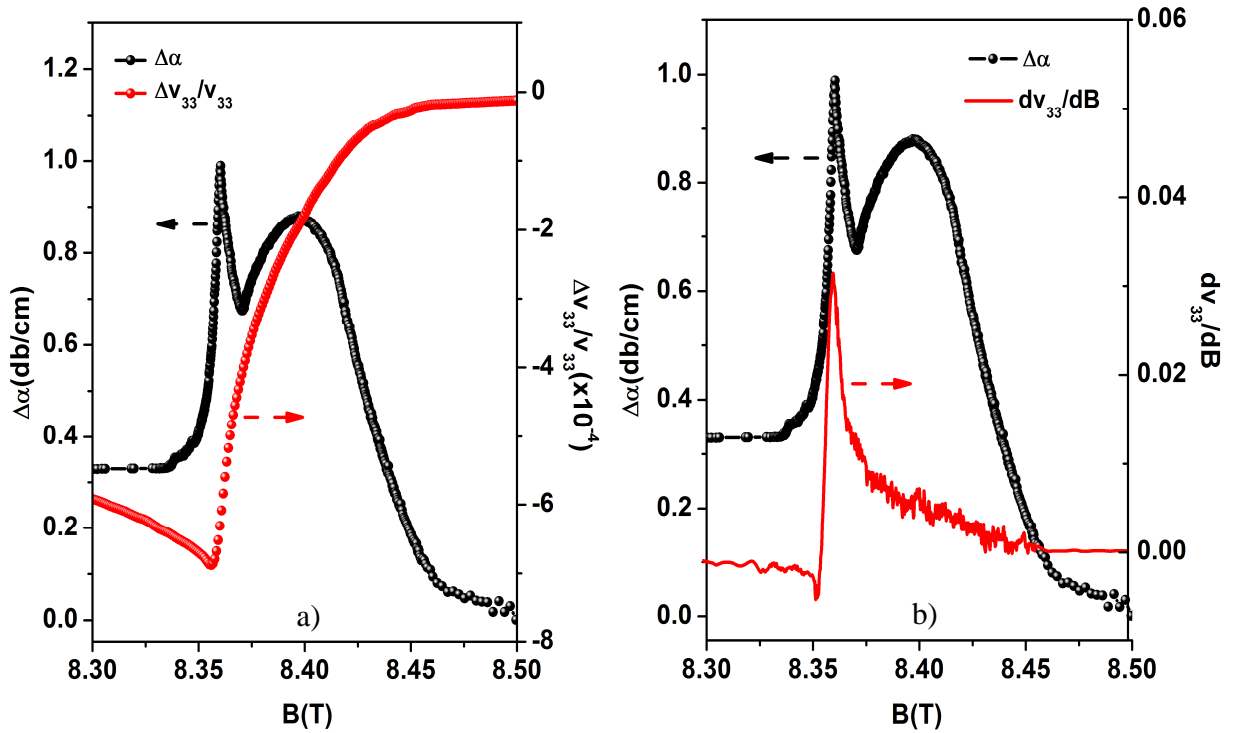
Figure 5.10 *Field dependence of the relative change of sound attenuation (left-axis) plotted together with the sound velocity (panel a) and the derivative of the sound velocity with respect to the magnetic field (right-axis, panel b) at 130 mK of the c_{33} mode.*

Panel (b) of Fig.5.10 shows the attenuation peak of the c_{33} mode (left-axis) at 130 mK together with the field derivative of the sound velocity (right-axis). In this representation, the double-peak anomaly in the elastic constant becomes even more obvious. While the steep rise of the sound velocity at B_s, i.e. the maximum in dv_{33}/dB, coincides with the sharp attenuation peak, dv_{33}/dB is only weakly field dependent at the second-round attenuation peak until the system reaches the fully-polarized state above B_s. These observations also stay valid for the other two modes c_{11} and c_{22}.
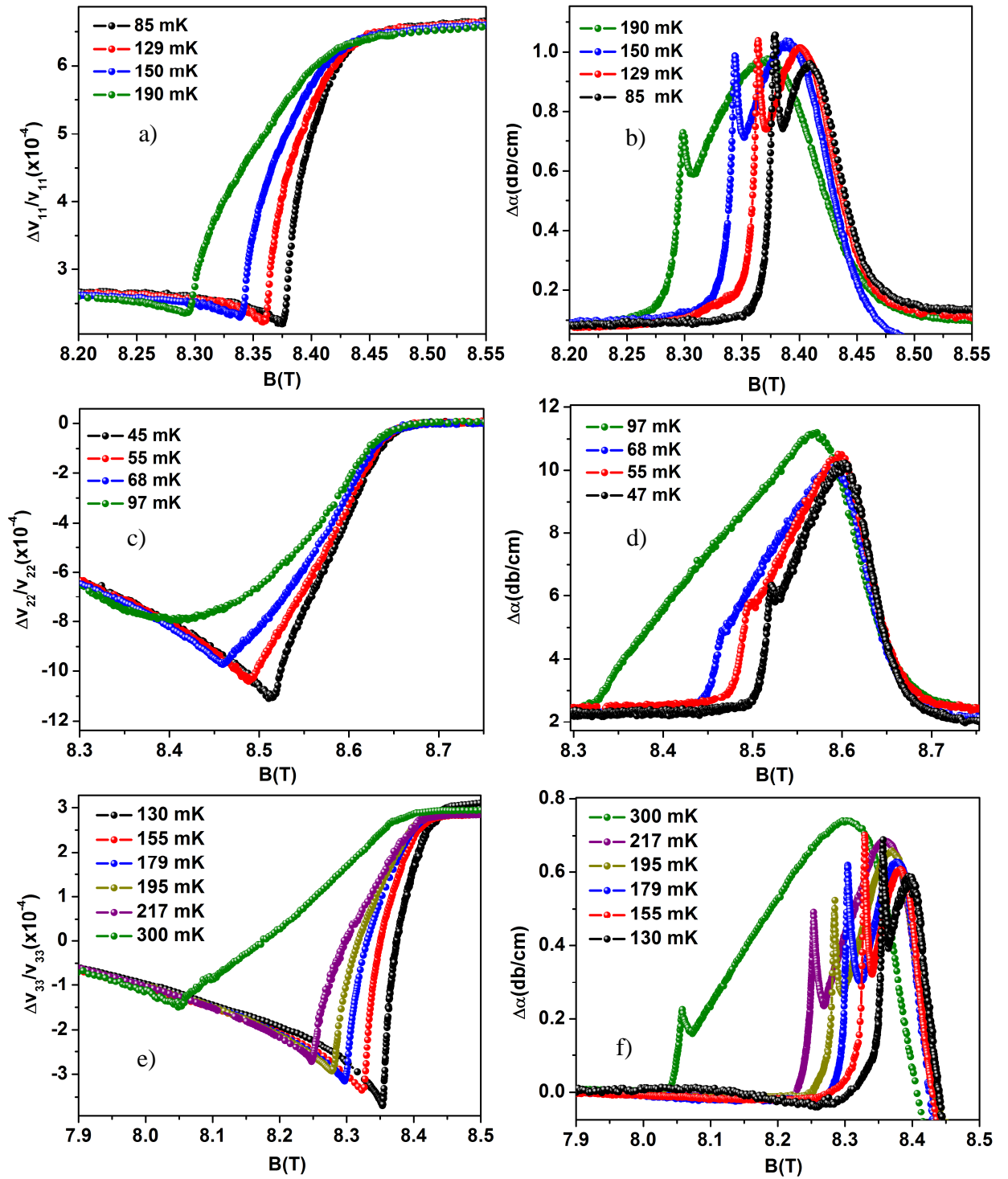
Figure 5.11 *The field dependence of the sound velocity (left panel) and the sound attenuation (right panel) at various temperatures deep inside the 3D AFM long-range ordered state. The first, second and third row corresponds to c$_{11}$ (panel a and b), c$_{22}$ (panel c and d) and c$_{33}$ (panel e and f) modes, respectively.*

The evolution of acoustic anomalies in the temperature regime, deep inside the 3D AFM long-range-ordered state, is shown in Fig. 5.11. The sound velocity (left panels) and the corresponding sound attenuation (right panels) of the c_{11}, c_{22} and c_{33} modes are presented in the first, second and third row, respectively. With decreasing temperature, the overall width of the attenuation anomaly gradually becomes narrower. The sharp peak that coincides with T_N, cf. Fig. 5.10, becomes more pronounced and shifts to higher fields albeit without any significant broadening. The growth in size upon cooling suggests that the peak reflects the contribution of critical fluctuations of the underlying quantum phase transition. This behavior contrasts with the phenomenology of the broad attenuation peak which significantly narrows and becomes reduced in size. The sound velocity also behaves in the same manner meaning that, the size of the softening, the temperature of which coincides with T_N, also increases upon cooling. The phase transition to the fully-polarized state becomes more and more steep with decreasing temperature.
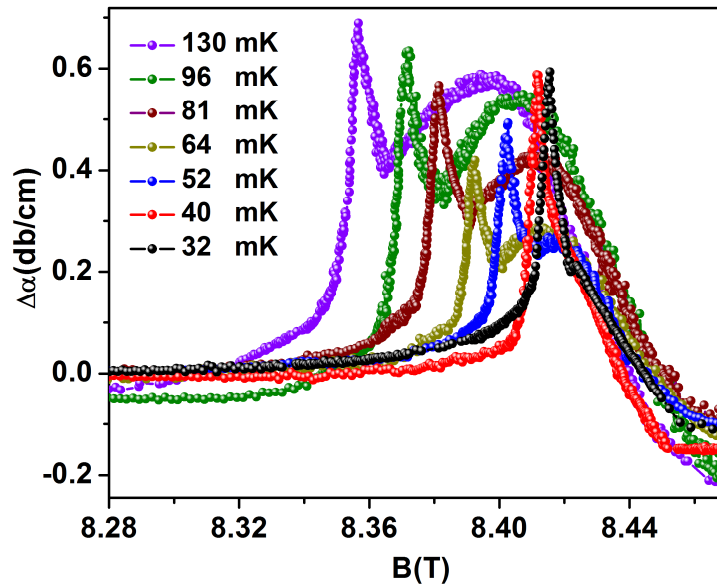
Figure 5.12 *The evolution of the sound attenuation with temperature deep inside the 3D long-range AFM ordered state.*

The question now is: how does this double-peak structure of the attenuation change as the system approaches the QCP. Figure 5.12 exhibits the field dependence of the ultrasonic attenuation for the c_{33} mode in the temperature range 0.032 K $\leq T \leq$ 0.13 K. As can be clearly seen, at 32 mK - the lowest temperature of our c_{33} measurements - the broad anomaly is almost totally suppressed and merges to the sharp one. It manifests itself as only a small shoulder on the high-field side of the

sharp attenuation peak. We suggest that the broad anomaly is a manifestation of the material's spin-liquid features, which precede the long-range antiferromagnetic order upon cooling [Coldea03].

c) Theoretical calculation

A theoretical study to obtain a microscopic description of the acoustic behavior of Cs$_2$CuCl$_4$ has been conducted in collaboration with Prof. Kopietz's group. It is based on the usual spin-wave expansion around the classical ground state of a Heisenberg model on an anisotropic triangular lattice with Dzyaloshinskii–Moriya interactions. The starting Hamiltonian has the form:

$$\tilde{H} = \frac{1}{2}\sum_{ij}\left[J_{ij}\cdot S_i \cdot S_j + D_{ij}\cdot\left(S_i \times S_j\right)\right] - \sum_i H\cdot S_i$$

where $J_{ij} > 0$ are antiferromagnetic exchange interactions, $\boldsymbol{D}_{ij} = -\boldsymbol{D}_{ji}$ are the antisymmetric Dzyaloshinskii-Moriya interactions, and H is an external magnetic field (see Ref. [Kreisel11] for details).

The change in the elastic constants and the ultrasound attenuation in the low-temperature regime where Cs$_2$CuCl$_4$ exhibits long-range magnetic order has been calculated. To add the relevant phonons to the Hamiltonian given above, the exchange interactions J_{ij} have been assumed to depend on the actual positions $r_i = R_i + X_i$ of the ions (where R_i are the sites of the Bravais lattice) which led to an expansion of J_{ij} in powers of the difference vectors $X_{ij} = X_i - X_j$,

$$J_{ij} = J(R_{ij}) + \left(X_{ij}\cdot\nabla_r\right)J(r)/_{r=R_{ij}} + \frac{1}{2}\left(X_{ij}\cdot\nabla_r\right)^2 J(r)/_{r=R_{ij}} + ...$$

Quantization of the phonon coordinates X_i leads to a rather complicated magnon-phonon interaction which has been treated using conventional diagrammatic many-body methods [Kreisel11].

A comparison of the results of these calculations for the change in the sound velocity (which is proportional to the shift in the corresponding elastic constant) with the experimental data of the c_{22} and c_{33} modes that were measured at 52 and 48 mK, respectively, is shown in Fig. 5.13 (a). From the inset, it is obvious that in the weak-field limit $B \leq 2.5$ T, where the calculations applied for the change of the sound velocity are expected to be most accurate, theory and experiment agree nicely. The deviations in the higher field are attributed to the breakdown of the theoretical approach that does not take into account the higher-order fluctuation corrections and other types of excitations.

These are likely to play a role in the vicinity of the critical magnetic field where the magnetic order vanishes.

Fig. 5.13 (b) shows the comparison of the theoretical calculations for the attenuation of the c_{22} and c_{33} phonon modes with the experimental data of the relative change of the attenuation $\Delta\alpha$. For fields in the range $H \leq 0.8H_c$, the measured attenuation is rather small, while one observes a strong enhancement for $H \rightarrow H_c$. The overall shape of the data is reproduced rather well by the theoretical curves, especially as it gives a satisfactory description of the strong enhancement of the attenuation in the vicinity of the critical field, cf. Fig. 5.13(b).
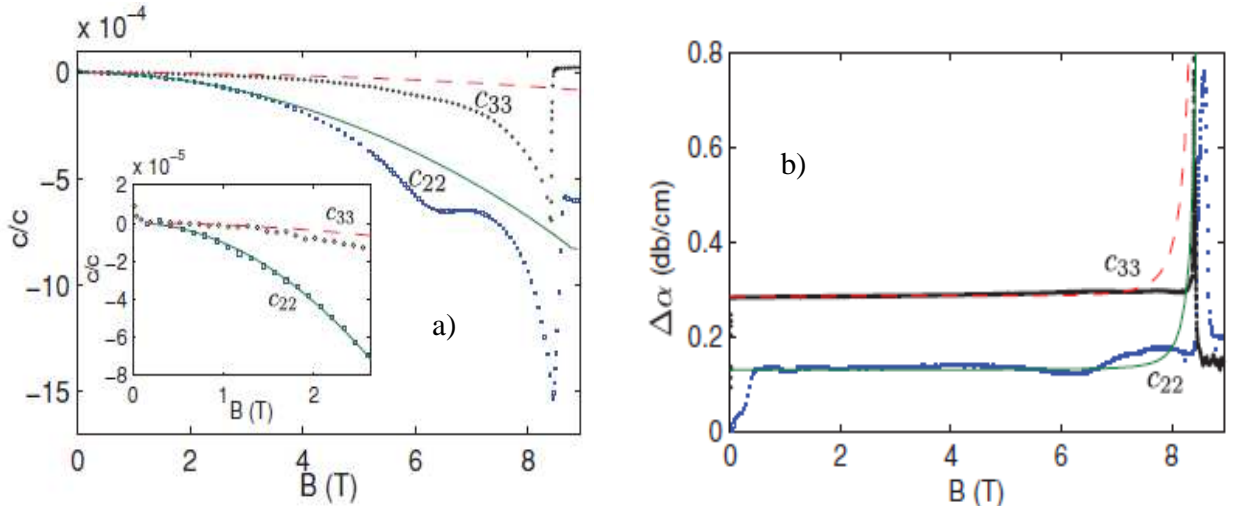
Figure 5.13 *a) Field dependence of the sound velocity of the c$_{22}$ (green dots) and the c$_{33}$ (black dots) modes in Cs$_2$CuCl$_4$ measured at T = 52 and 48 mK, respectively, plotted together with theoretical results (blue solid and red-dashed line). b) Corresponding attenuation of the c$_{22}$ (green dots) and c$_{33}$ (black dots) modes which have been compared to theoretical calculations (blue-solid and red-dashed lines) with the parameters obtained from the fit to the velocity change (reprinted from Ref. [Kreisel11]).*

d) Phase diagram and Bose-Einstein Condensation

The B vs T phase diagram of Cs$_2$CuCl$_4$ for the field B // a-axis obtained from our ultrasound experiments is presented in Fig. 5.14. The phase diagram was constructed from anomalies of the sound attenuation as a function of field and temperature. The green and blue points indicate the data

taken from the c_{11} and c_{33} modes, respectively. The filled squares are the data from temperature dependence of the attenuation while at the same time the filled triangles and filled stars are, respectively, the sharp and broad peaks (or single round peak) of the attenuation seen in field-dependent measurements.

The phase boundary represented by filled squares and filled triangles, connected by a red solid line as a guide to the eyes, presents the field dependence of the antiferromagnetic phase transition temperature. It is in very good agreement with $T_N(B)$, obtained from specific heat and magnetocaloric measurements shown in Fig.5.3. The boundary reveals that above 8 T, T_N decreases strongly so that the end point of this phase boundary marks the QCP ($T_N \rightarrow 0$ as B $\rightarrow B_c$).
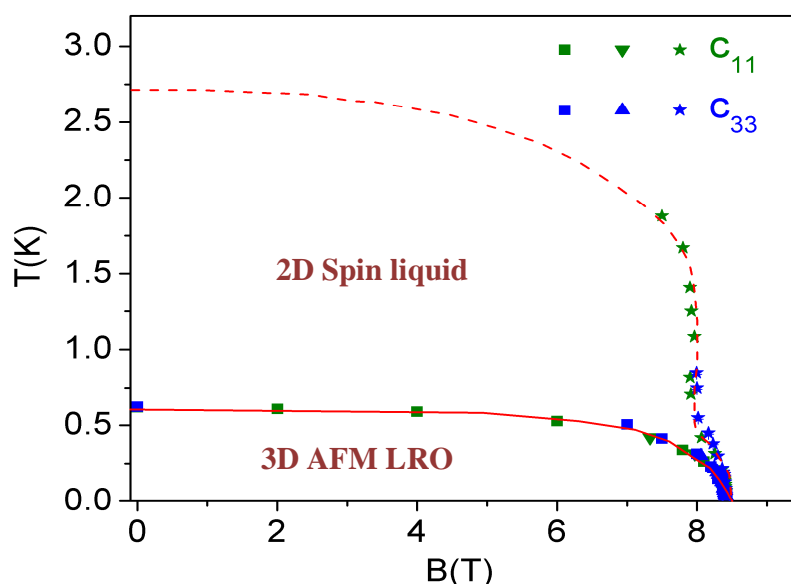
Figure 5.14 *B-T phase diagram for B // a-axis constructed from the attenuation anomalies of temperature and field dependent measurements. Solid and dashed lines are guides for the eyes.*

Another "phase boundary" as crossover line denoted by filled stars is related to the transit from the 2D spin liquid to the paramagnetic state, as discussed above. This boundary is built up initially from the position of the single round peak in the attenuation in field-dependent measurements in the spin-liquid state regime (0.62 < *T* < 3 K) followed by the broad anomaly obtained from measurements inside the 3D AFM long-range ordered state at temperatures below *T* < 0.6 K. This "phase boundary" also ends at the QCP, cf. Fig. 5.14. Note that the 2D spin-liquid crossover boundary displayed in Fig. 5.3 was constructed by using T_{max} of magnetic susceptibility data, valid

only for to $T \sim 0.6$ K and $B \sim 8$ T due to the lack of experimental data. Consequently, we stress that our data reveal, for the first time, the spin-liquid crossover boundary in the very low temperature regime, near the QCP, and completes the phase diagram for B//a-axis of Cs₂CuCl₄.
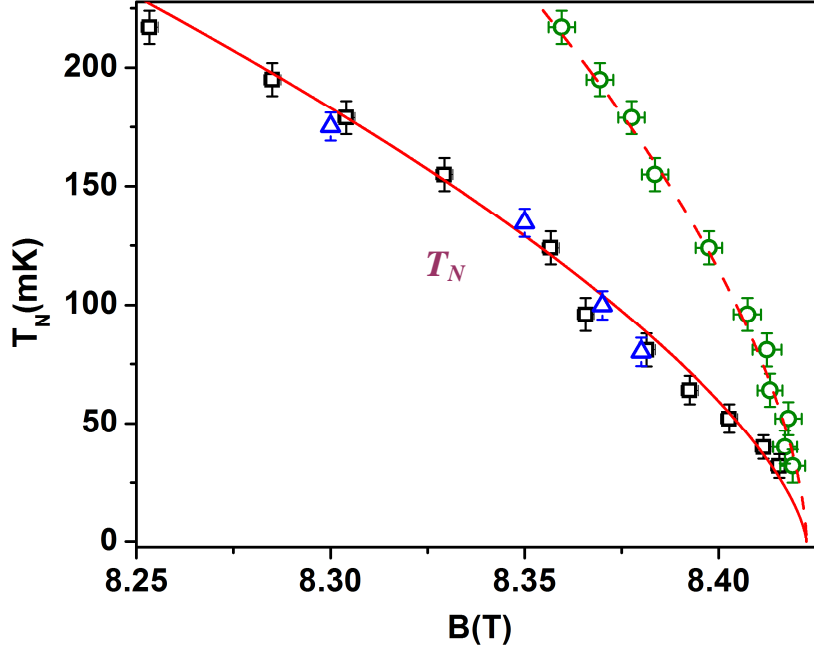
Figure 5.15 *B-T phase diagram around the QCP of Cs₂CuCl₄ for B//a-axis. Open triangulars are taken from the temperature dependence of the sound attenuation. Open squares and open circles are the positions of the sharp and broad, respectively, of the attenuation from field-dependent measurements. Solid and dashed lines represent the power-law fitting curve.*

As mentioned in the Introduction, the field-induced AFM phase transition, as the system approaches the QCP, can be understood as a magnon BEC. From the position of the field-induced phase transition, the critical exponent Φ can be determined:

$$T_c \sim (B_c - B)^{1/\Phi}.$$

Theoretically, for a 3D Bose gas, a universal value $\Phi_{BEC} = 3/2$ has been predicted [Giamarchi99, Nohadani04] coinciding with the result of a mean-field treatment [Nikuni00]. Recently, the specific heat and the magnetocaloric measurements [Radu05, Radu07] around the QCP have been used to extract the critical exponent, giving a value of 1.55. This value is close to the theoretical prediction. However it has to be stressed that the value of the critical exponent is very sensitive to the choice of

B_c. Just a small difference of B_c can lead to a large change in the value of Φ. Moreover, the fitting formula shown above contains two free parameters, B_c and Φ, which can be determined from the fit to the experimental data. As a result, there have been some controversies over the procedure to simultaneously define exactly these two free parameters. Our aim is to check again the validity of the BEC description applied to the Cs$_2$CuCl$_4$ near the QCP using our ultrasound measured data.

The crucial point in the fitting process is to define the critical field B_c and afterwards to conduct the fitting to obtain the critical exponent. In our case, there is an advantage, as the discussion above shows that the two phase boundaries, the AFM and crossover SL states, end at the critical field B_s when $T \rightarrow 0$. We assume that these phase boundaries can be described by a power-law function but with different values of the critical exponent Φ. We need to find out B_c that simultaneously gives the smallest error in the fittings for the two data sets. So we let the B_c vary from $B_{c1} = 8.4$ T to $B_{c2} = 8.5$ T with a step widths of 0.001 T, perform a non-liner least-squares fitting for each B_{ci} and choose the B_{ci} that gives the smallest confidence bounds of parameters and highest coefficient of determination (R-square). Note that for a more thorough test, it is important to perform the fitting procedure in a narrow field window close to B_c where the theoretical predictions are valid.

The best fit with our experimental data of the c_{33} mode presented in Fig 5.15 reveals $B_c =$ 8.422(1) T and the critical exponent of 1.47(1) and 1.67(1) for the AFM and SL phase boundary, respectively. The value $\Phi = 1.47$ is in very good agreement with $\Phi = 1.5$ predicted theoretically for 3D BEC of magnons and with the published results in Ref. [Radu07]. The meaning of the power law field dependence of the SL "phase-boundary" with a critical exponent of 1.67 is still unclear.

5.4 The quasi-2D quantum-spin system Cs$_2$CuBr$_4$

5.4.1 Magnetic properties and phase diagram

Extensive experimental works [Ono03, Ono04, Fortune09, Tsujii07] have been performed on Cs$_2$CuBr$_4$ revealing a rich magnetic phase diagram of this system. At zero field, thermodynamic measurements show antiferromagnetic order at 1.43 K [Ono03]. For the field orientation along each of the three crystallographic axes, the ordering temperature gradually decreases as the applied field is increased. The saturation field is about 30 T.

Elastic neutron scattering has found that in the ordered phase, spins lie approximately in the *bc*-plane and form an incommensurate helical structure which is characterized by a wave vector Q$_0$ = (0,

0.575, 0) [Ono04]. For a classical spin model, the ordering vector is given by $cos(\pi Q_0) = -J'/2J$. Using $Q_0 = 0.575$, the authors obtained $J'/J = 0.467$ exceeding the value of 0.176 found by similar means for the isostructural compound Cs_2CuCl_4. Due to the spin-1/2, the quantum corrections of the helical pitch are significant in the present system, and thus, the value of J_1/J_2 obtained from the classical spin model is different from the real value when $J' \neq J_2$. Numerical calculations including quantum fluctuation effects have been performed with Q_0 as a function of $J'/(J' +J)$ giving the value of $J'/J = 0.37$ and 0.74 for Cs_2CuCl_4 and Cs_2CuBr_4, respectively, indicating that Cs_2CuBr_4 is more frustrated than Cs_2CuCl_4.
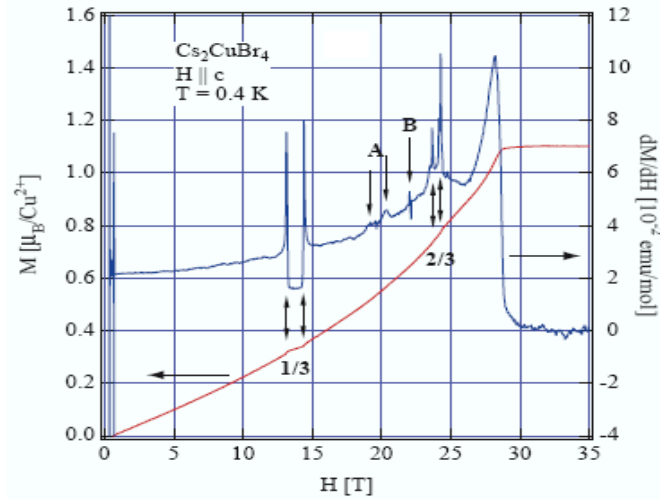
Figure 5.16 *Magnetization curves and dM/dH vs H of Cs₂CuBr₄ measured at T = 0.4 K for H//c-axis. Arrows denote critical fields [Ono03].*

The Hamiltonian for Cs_2CuBr_4 is given by:

$$H = J \sum_{<i,j>} S_i \cdot S_j + J' \sum_{<i,k>} S_i \cdot S_k .$$

Here $J = 11$ K for the nearest-neighbor coupling along the b-axis and $J' = 8.3$ K for weaker nearest-neighbor coupling within the bc- plane. Not included in the Hamiltonian are two small perturbations expected to be present: an antiferromagnetic interlayer coupling that causes the spins to order at 1.4 K in zero field, and an anisotropic super-exchange interaction (Dzyaloshinskii- Moriya type) that causes the spins to lie along the plane of the triangular lattice at zero field.

Figure 5.16 shows the magnetization curve and *dM/dH* vs *H* measured at *T* = 0.4 K for *H//c*-axis. A notable feature is that the magnetization curve has a plateau at approximately one-third of the saturation magnetization M_s. This is more clearly recognized in *dM/dH* vs *H* shown in Fig. 5.16. The 1/3-magnetization-plateau was also observed for *H//b*-axis, while no plateau was observed for *H//a*-axis. Because the 1/3-magnetization-plateau in Cs₂CuBr₄ is clearly observed for two different field directions, the plateau cannot be explained in terms of the classical model. Thus, the conclusion is that the magnetization plateau arises from quantum effects. The Dzyaloshinsky-Moriya (DM) interaction with the **D** vector, perpendicular to the triangular lattice, should be responsible for the absence of the magnetization plateau for *H//a*.

In addition, *dM/dH* in Fig. 5.16, exhibits an additional sharp double-peak structure around *H* = 23 T, where the magnetization is approximately 2/3M_s. This is indicative of the second tiny plateau at 2/3M_s. This additional sharp double-peak structure in *dM/dH* was also observed for *H//b*-axis. The magnetization processes for *H//c*- and *b*-axis almost coincide when normalized by the *g* factor. This means that spin-spin interactions are almost isotropic in the triangular-lattice plane. Magnetocaloric and specific heat measurements have been used to construct the *B-T* phase diagram of Cs₂CuBr₄. A cascade of magnetic-field-induced quantum phase transitions has been observed below the saturation field for *H//b*-axis and *H//c*-axis.
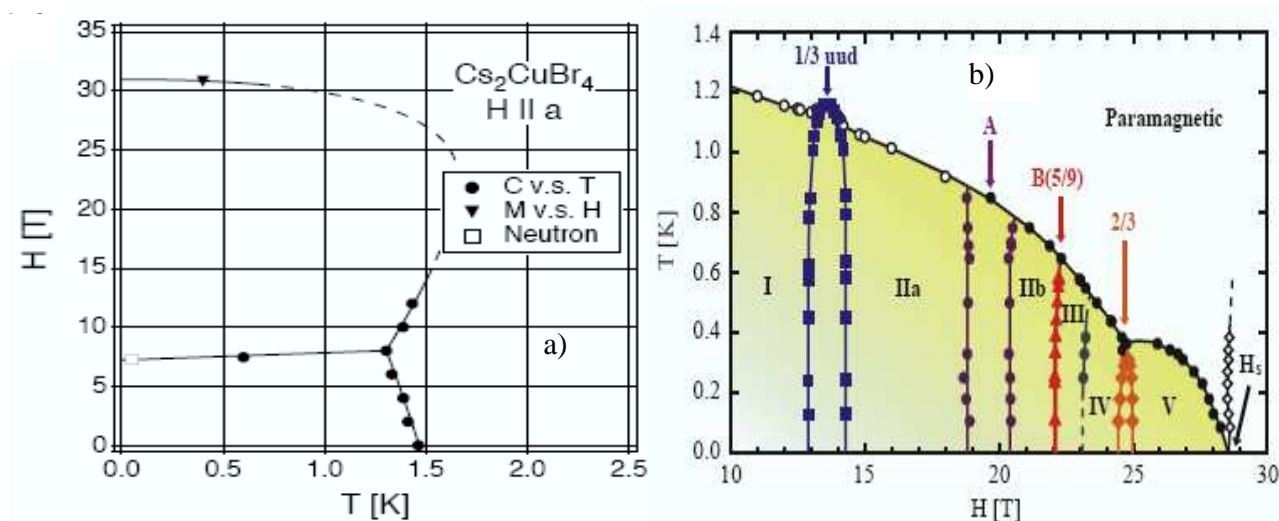
Figure 5.17 *Magnetic phase diagram deduced from various measurements for B//a-axis (a) and B//c-axis (b) [Ono03, Fortune09]*

Fig. 5.17 (a) and (b) show the phase diagram for *H//a*-axis and *H//c*-axis, respectively. For *H//c*, in addition to the 1/3 and 2/3 plateau phases, many quantum phases have been observed. The phase transitions to the A phase and the transitions to the very narrow B phase can also be observed as small peaks in *dM/dH* shown in Fig. 5.16. These successive quantum phase transitions should be attributed to the spatially anisotropic triangular lattice and the Dzyaloshinsky-Moriya interaction with the **D** vector perpendicular to the triangular lattice [Nohadani04, Fortune09, Morosin61], but an overall explanation is still missing.

5.4.2 Results and discussion

a) Temperature dependence

Fig. 5.18 presents the temperature dependence of the elastic constant $c_{11}(T)$ measured at zero field. Fig. 5.18 (a) shows the data over the whole temperature range together with the elastic background obtained by applying the Eq. 2.11.
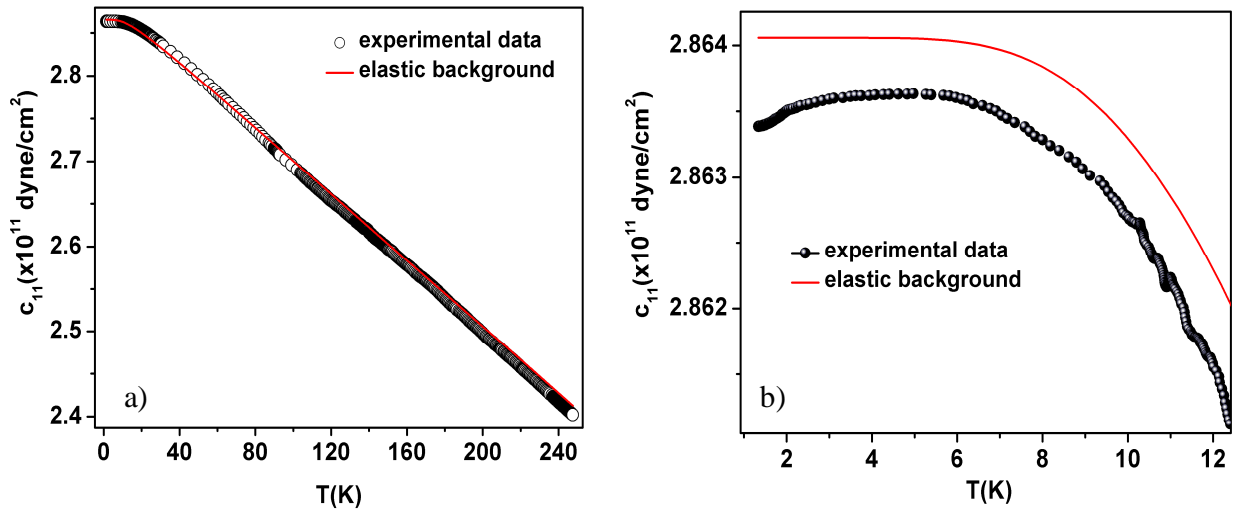
Figure 5.18 *a) Temperature dependence of the elastic constant for the acoustic c_{11} mode in zero field measured at 50 MHz with elastic background (red line). b) Low-temperature part showing the softening of c_{11} which deviates from the elastic background (red line) at low temperature.*

The elastic constant grows linearly with decreasing temperature and does not reveal any distinct anomaly in the temperature range investigated. On decreasing the temperature to below about 6 K, it shows a slight softening, as seen in Fig 5.18 (b). At 1.4 K, no clear evidence of a phase transition is

observed when the system enters the 3D long-range magnetically ordered state which may be due to the small magneto-elastic coupling of the spin-lattice with the sound wave along the *a*-direction.

b) Field dependence

We have also performed pulsed magnetic field experiments on Cs_2CuBr_4 in order to study the acoustic behavior in the region of the magnetization plateau. The change of sound velocity c_{11} mode as a function of magnetic fields up to 50 T applied along the crystallographic *a*-axis (panel a) and *b*-axis (panel b) at temperatures of 1.5, 1.9 and 4.2 K are shown in Fig. 5.19. Unfortunately, the lowest achievable temperature of 1.5 K, we could reach in this experiment was still in the paramagnetic region of the system (cf, Fig. 5.17). The results exhibit a continuous softening of the sound velocity upon increasing the field up to saturation without any pronounced resolvable anomaly.
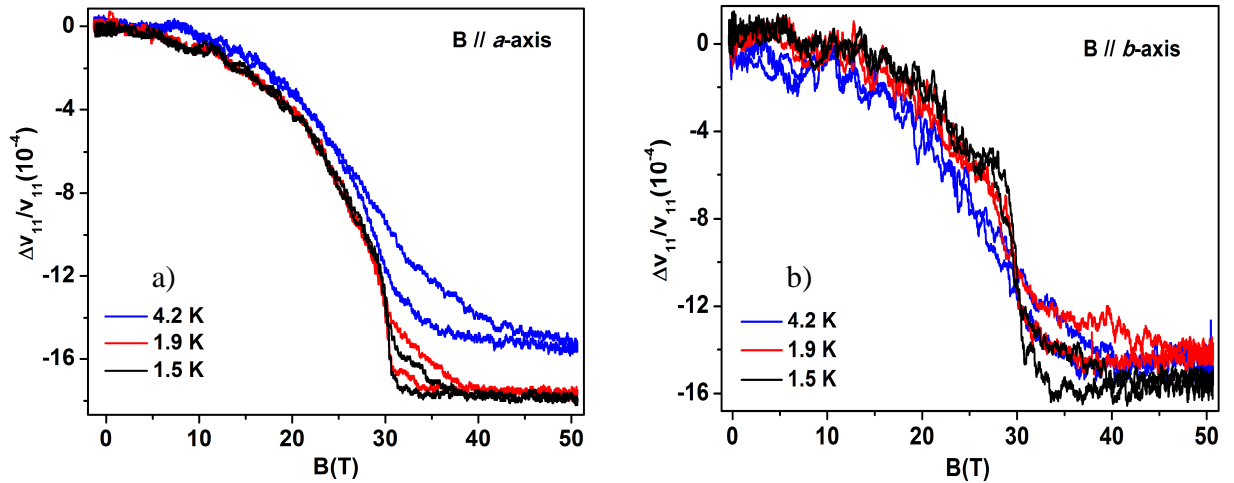
Figure 5.19 *Field dependence of the sound velocity for the c_{11} mode in Cs_2CuBr_4 measured in pulsed magnetic fields at various constant temperatures. The applied fields are along the a-axis (panel a) and the b-axis (panel b).*

The sizes of the softening are comparable, regardless of the applied field direction indicating an isotropy in the magneto-elastic coupling in the high-temperature range (i.e., the spin system in the paramagnetic state). On the other hand, we can say that the thermal fluctuations at high temperatures destroy the low-dimensional nature of the system. At about 32 T, the *step-like* phase transition from the paramagnetic to the fully polarized state is observed. The phase transition anomaly is steeper and sharper at lower temperature.

<div align="center">

6

THE FRUSTRATED QUANTUM ANTIFERROMAGNET Cs$_2$CuCl$_{4-x}$Br$_x$

</div>

This chapter presents a systematic study of the crystal growth, structure and magnetic properties of the Cs$_2$CuCl$_{4-x}$Br$_x$ ($0 \leq x \leq 4$) mixed system, which includes the two known end-member compounds Cs$_2$CuCl$_4$ and Cs$_2$CuBr$_4$. The first objective was to provide a thermally stable single crystal over the whole concentration range of the mixed system of the same type of structure. The second one, the magnetic study, was conducted by comparative measurements of the magnetic susceptibility $\chi(T)$ that reveals three distinct magnetic regimes separated by critical concentrations $x_{c1} = 1$ and $x_{c2} = 2$. This unusual magnetic behavior can be explained by considering the structural peculiarities of the materials, especially the distorted Cu-halide tetrahedra, which support a site-selective replacement of Cl$^-$ by Br$^-$ ions.

6.1 Introduction

As mentioned in chapter 5, the frustrated layered antiferromagnets Cs$_2$CuCl$_4$ and Cs$_2$CuBr$_4$ have recently attracted a lot of interest because of their unconventional magnetic properties [Coldea03, Tanaka02]. Both compounds have been classified as two-dimensional spin systems, with an underlying anisotropic triangular lattice of spin-1/2 Cu^{2+} ions, cf. Fig 5.1. Although being iso-structural, these compounds display rather different magnetic properties.

In Cs$_2$CuCl$_4$, besides the attraction due to the spin fractionalization and the spin-liquid state, the field-induced quantum phase transition at the QCP B_s has been also intensively studied. The analogy of the critical properties to that of a Bose-Einstein condensation has been pointed out [Radu05] suggesting that it is the delocalization of magnetic triplet excitations, which governs the physics in Cs$_2$CuCl$_4$ near B_s [Coldea03]. A different situation is encountered for the related Cs$_2$CuBr$_4$ compound where the Cl ions have been replaced by Br. This system undergoes a Néel ordering at T_N = 1.4 K at zero field. For applied fields parallel to the *b*- and *c*-axis, two plateaus at approximately one-third and two-thirds of the saturation magnetization have been observed [Tanaka02] indicating that here, as a consequence of frustration, the repulsive interaction dominates, giving rise to the localization of the triplet excitations. The difference in the magnetic behavior of these two iso-structural compounds originates from their unequal degree of frustration that is determined by the

<div align="center">

99

</div>

ratio J'/J between the interchain-exchange coupling J' and the dominant intrachain-exchange coupling J. Although Cs_2CuBr_4 and Cs_2CuCl_4, the field dependent magnetic properties of which reflecting dominant repulsive and kinetic energy of the magnetic excitations, respectively, have been studied to some extent, no investigation exists on the interesting crossover regime. These two border cases thus motivate the study of the magnetic properties of the solid solution $Cs_2CuCl_{4-x}Br_x$, in which by a continuous replacement of Cl^- by Br^-, the frustration effects are expected to become increasingly important.

6.2 Review on the crystal structure of Cs_2CuCl_4 and Cs_2CuBr_4

The crystal structure of Cs_2CuCl_4 and Cs_2CuBr_4 at ambient conditions was determined by several authors as orthorhombic with space group *Pnma* [Morosin61, Bailleul91]and McGinnety72]. The unit cell, cf. Fig. 5.1(a) and Fig 6.1, consists of four flattened $[Cu(Cl/Br)_4]^{2-}$ tetrahedra and eight Cesium atoms. Thus, the unit cell contains four $Cs_2Cu(Cl/Br)_4$ entities. Tetrahedra, with the same orientation, form linear chains in the *b*-axis direction, as illustrated in Fig. 5.1(b). These chains stack together along the *c*-axis direction, displaced by *b*/2 with respect to each other and with each tetrahedron orientation reversed, thus forming a planar triangular pattern. The tetrahedra are well-isolated from each other as they do not share any common coordination element. For example, the shortest Cl-Cl distance between two adjacent tetrahedra is along the *b*-axis and amounts to 3.634 Å, significantly larger than the covalent radius of chlorine. All other distances between Cl atoms belonging to adjacent tetrahedra are even longer. Finally, adjacent planes are separated from each other by Cs^+-ions, cf. Fig 5.2, resulting in a quasi-two-dimensional (quasi-2D) spin S = ½ arrangement.

Table 6.1 *Bond lengths of the flattened Cu-halide tetrahedron in Cs_2CuCl_4 and Cs_2CuBr_4 taken from Refs. [Morosin61] and [Bailleul91] together with the ratio of bond length to covalent radius.*

	Cu-Cl bond length [Å]	Bond length / Covalent radius			Cu-Br bond length [Å]	Bond length / Covalent radius
Cl 1	2.244	0.959		Br 1	2.385	0.946
Cl 2	2.235	0.956		Br 2	2.362	0.937
Cl 3	2.220	0.940		Br 3	2.342	0.931
Cl 3	2.220	0.940		Br 3	2.342	0.931

An important structural feature, shared by both compounds, originates from the local Cu environment. As a consequence of the flattened Cu-halide tetrahedron, the bond lengths are significantly different. There is a longest Cu-halide bond, Cu-Cl1/Br1, and two equivalent shortest Cu-Cl3/Br3 bonds, cf. inset of Fig. 6.1 and Table I for structural data taken from Refs. [Morosin61] and [Bailleul91].
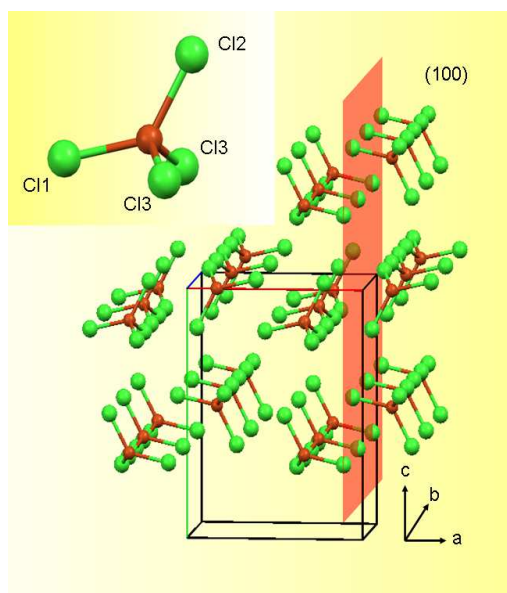
Figure 6.1 *View of the crystal structure of Cs$_2$CuCl$_4$ with a tilt of 6° along the a-axis and rotated - 6° around the c-axis of the orthorhombic structure of Cs$_2$CuCl$_4$. Cs atoms are omitted for clarity. The longest Cu-Cl1 bonds are pointing along the a-direction perpendicular to the magnetic layers which are parallel to the (100)-plane shown in red. Inset: Strongly flattened Cu-Cl tetrahedra with the three inequivalent Cl bonds. The bond lengths are listed in Table I [Cong11].*

The tetrahedra are oriented such that the long Cu-Cl1/Br1 bonds point along the interlayer *a*-axis. As a result, this bond is involved in mediating the interlayer exchange *J''*. In contrast, the Cu-Cl3/Br3 bonds are located within the *bc*-plane and are oriented along the *b*-axis, where adjacent Cu-halide tetrahedra have the shortest distance. This suggests that, as a consequence, the Cu-Cl3/Br3 bonds are involved in mediating the dominant magnetic interaction *J*. The exchange interactions of Cs$_2$CuCl$_4$ and Cs$_2$CuBr$_4$ have been determined from measurements of the magnon dispersion in the saturated ferromagnetic phase with the magnetic fields applied along the *a*-axis [Coldea02] and the

neutron scattering experiments [Ono04], respectively. These ratios of exchange couplings are shown in Table 6.II indicating that Cs_2CuCl_4 is less frustrated and more one-dimensional than Cs_2CuBr_4.

Table 5.2: *Ratios of exchange coupling interactions in Cs_2CuCl_4 and Cs_2CuBr_4 taken from Refs. [Coldea02] and [Ono04].*

	Cs_2CuCl_4		Cs_2CuBr_4
J'/J	0.34		0.74
J''/J	0.1		0.1
D/J	0.1		0.05

6.3 Magnetic susceptibility of Cs_2CuCl_4 and Cs_2CuBr_4

Early characterization of Cs_2CuCl_4 by susceptibility measurements has been carried out on polycrystal samples by Carlin *et al.* [Carlin85] and on single crystals by Sharnoff *et al.* [Sharnoff65] A more recent susceptibility and bulk magnetization study by Tokiwa *et al.* [Tokiwa06], triggered by recent neutron scattering results [Zheng05], give a more complete picture of the magnetic behavior of the sample. The temperature dependence of the uniform susceptibility is presented in Fig. 6.2(a) at low fields (H = 0.1 T) for the three principal crystallographic directions [Tokiwa06]. At high temperature ($T > 20$ K), the material is in the paramagnetic phase and the susceptibility, $\chi(T)$, follows a Curie-Weiss law of the form:

$$\chi_i(T) = \frac{C_i}{T - \Theta_W} \text{ with } C_i = \frac{N_A g_i^2 \mu_B^2 S(S+1)}{3k_B} \quad (6.1)$$

Fits to the experimental data give a negative Curie-Weiss temperature of Θ_W = -4.0 (0.2) K, indicating that the principal couplings are antiferromagnetic, and values of the g-factor g_a = 2.27, g_b = 2.11 and g_c = 2.36, consistent with ESR measurements [Sharnoff65]. For $T > T_{max}$, the high-temperature series expansion calculations of the susceptibility using a 2D spin-1/2 Hamiltonian on an anisotropic triangular lattice [Tokiwa06], the black curve in Fig. 6.2(b), is found to be in good agreement with the experimental data when the exchange couplings are set to J'/J = 1/3 and J = 4.35 K. In contrast, the data depart significantly from the expected Bonner-Fisher curve [Bonner64], dotted-black curve, for one-dimensional chains (J' = 0), due to the weak spin frustration leading to

the reduction of the magnetic susceptibility for Cs$_2$CuCl$_4$. Lowering the temperature, a broad maximum occurs around T_{max} = 2.8 K, indicating the development of short-range antiferromagnetic spin-spin correlations. Upon further cooling, a clear kink appears at T_N = 0.62 K observed along the b- and c-axis reflecting the transition into a long-range ordered (LRO) phase.
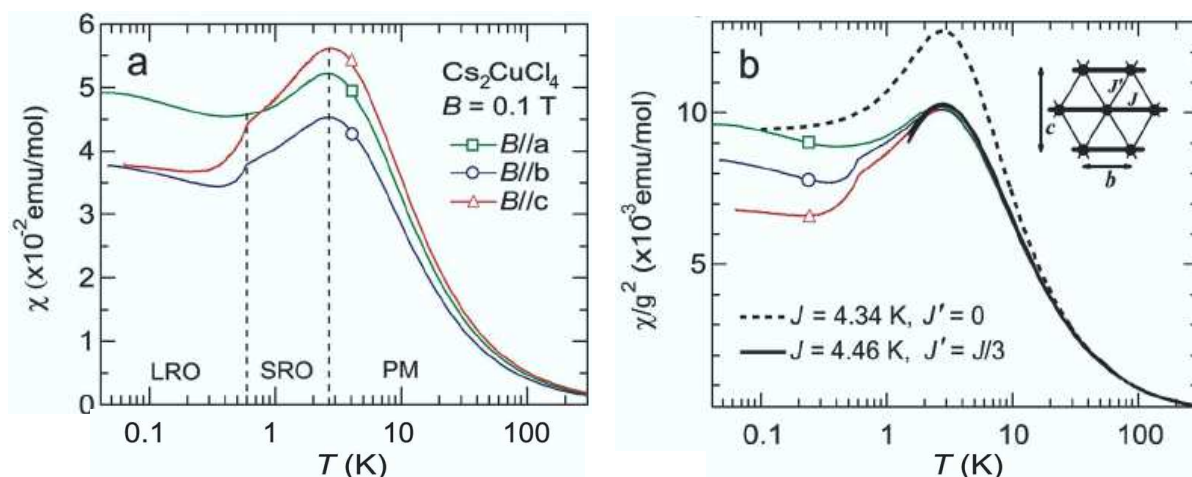
Figure 6.2 (a) Temperature dependence of the susceptibility of Cs$_2$CuCl$_4$ along the three principal crystallographic axes at H = 0.1 T. (b) Comparison between the susceptibility divided by g^2 and calculations for a 2D HAF on an anisotropic triangular lattice (reprinted from Ref. [Tokiwa06]).
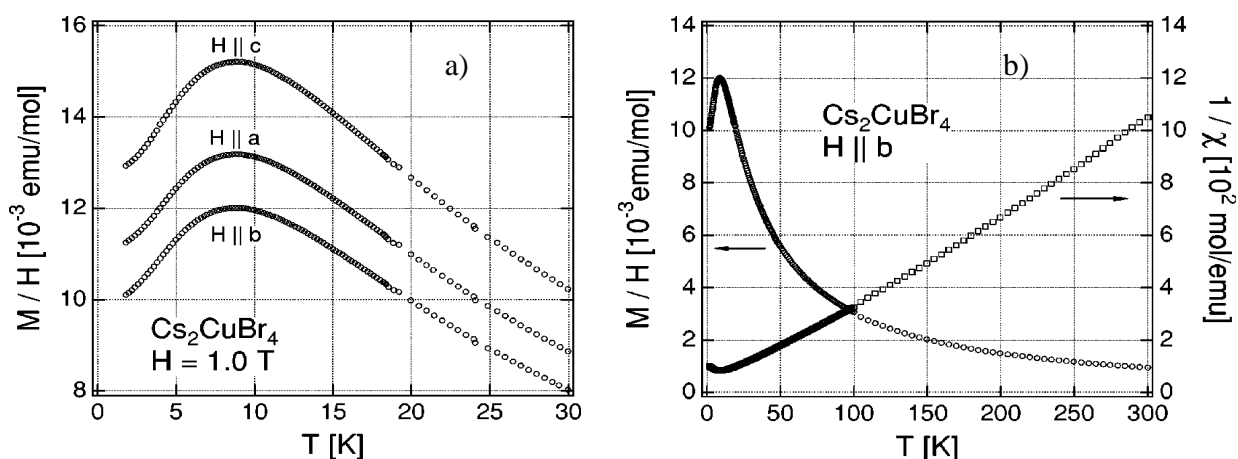

Figure 6.3 (a) Low-temperature magnetic susceptibilities of Cs$_2$CuBr$_4$ for H = 0.1 T parallel to the principal crystallographic axes. (b) Magnetic susceptibility and inverse susceptibility as a function of temperature for H//b-axis (reprinted from Ref. [Ono03])

Fig. 6.3(a) shows the low-temperature part of the magnetic susceptibility, $\chi(T)$, of Cs$_2$CuBr$_4$ as a function of temperature measured at $H = 1.0$ T for the three principal crystallographic axes. As expected, with decreasing temperature the susceptibility increases rapidly and shows a broad maximum at $T_{max} = 9$ K [Ono03], a characteristic of the low-dimensional antiferromagnetic spin system, similar to the behavior observed in Cs$_2$CuCl$_4$. The value of T_{max} in this compound is about three times larger than the one obtained in Cs$_2$CuCl$_4$. This reflects the larger exchange interactions in Cs$_2$CuBr$_4$ compared to those in the Cs$_2$CuCl$_4$. The inverse susceptibility also obeys a Curie-Weiss law. The Curie-Weiss temperature of Cs$_2$CuBr$_4$ has a value of $\Theta_W = -18.4\ (0.2)$ K [Cong11] obtained by performing a linear fit to the high-temperature experimental data indicating a stronger antiferromagnetic coupling compared with Cs$_2$CuCl$_4$

6.4 Crystal growth and thermal stability

The mixed system Cs$_2$CuCl$_{4-x}$Br$_x$ has proved to be a very rich system with several structural variants that can be realized depending on the growth conditions. By growing the crystals from aqueous solution, cf. Ref. [Krüger10] for details, the growth temperature is the crucial parameter for the selection of the crystalline phase that is formed for a given composition. There is a competition between tetragonal and orthorhombic phases and between those with and without incorporated crystal water.

If the growth of Cs$_2$CuCl$_{4-x}$Br$_x$ takes place at room temperature (~ 300 K), the orthorhombic structure type of Cs$_2$CuCl$_4$ and Cs$_2$CuBr$_4$ is left for an intermediate concentration range ($1 < x < 2$) and a new tetragonal phase is formed with the space group I4/mmm [Krüger10]. For growth temperatures of at least 350 K, the orthorhombic structure of the end members of the mixed-crystal series is preserved over the whole composition range. These crystals are highly hygroscopic and show significant degradation when they are stored for a long time at room temperature without sufficient protection against humidity. Even if in such crystals no foreign phases are found by diffraction experiments at room temperature, they may still content a considerable amount of the tetragonal phase that can be observed in low-temperature experiments and are severely damaged (cracks) when brought back to room temperature. However no stability problems are encountered with the orthorhombic phase even at very low temperatures, if the crystals are heated shortly to about 450 K prior to use in such experiments. As an example, the Fig. 6.4 shows the magnetization (main panels) and magnetic susceptibility (insets) of the sample Cs$_2$CuCl$_{2.8}$Br$_{1.2}$. Panel (a) shows the

data of the sample, grown at 300 K adopting tetragonal structure, exhibiting the typical magnetic behavior of the tetragonal-phase sample in which the saturated magnetization, *M(B)*, can be reached by quite small fields of ~ 1 T, and the magnetic susceptibility, *χ(T)*, has an anomaly around 11 K indicating the long-range anfiferromagnetic ordering transition. Panel (b) and (c) show the data of the orthorhombic-structure samples grown at 350 K.
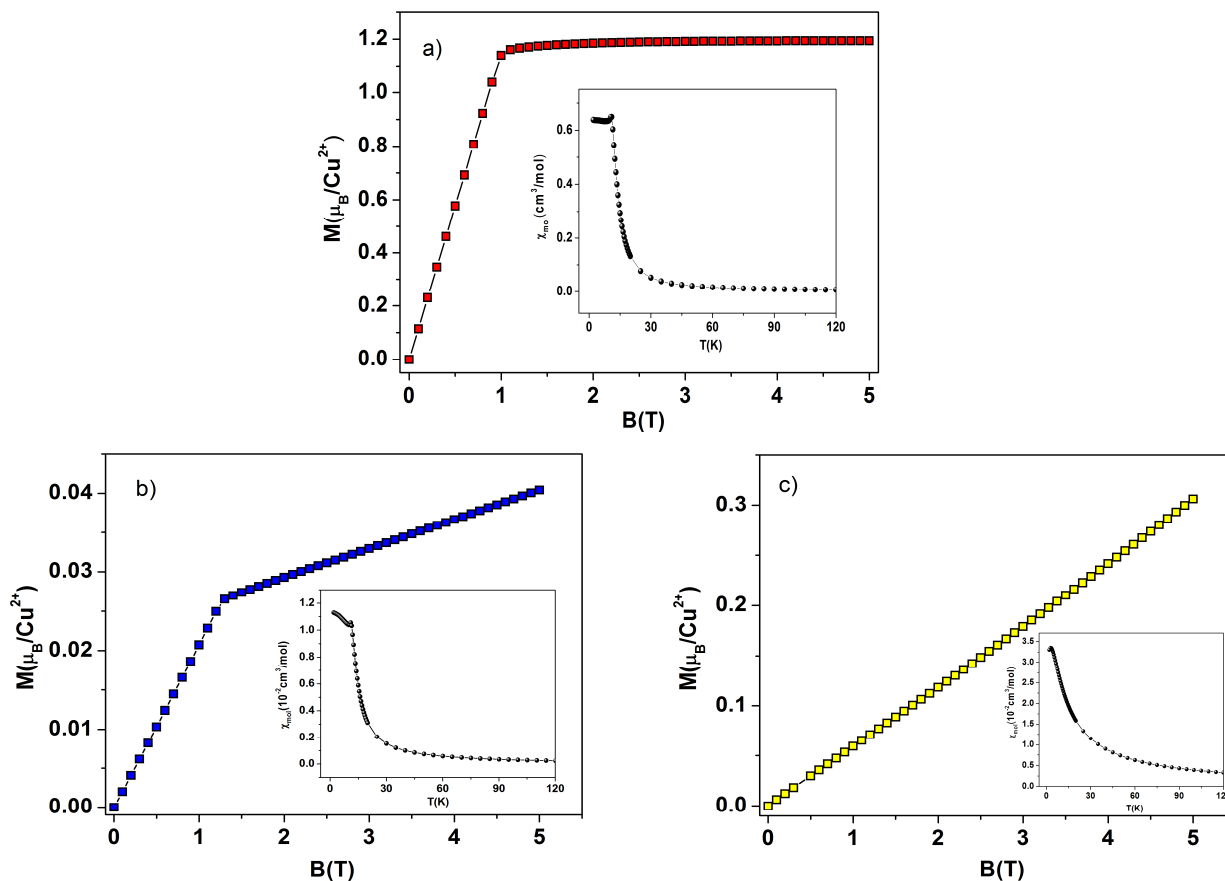
Figure 6.4 *Magnetization (main panels) and magnetic susceptibility (insets) of Cs$_2$CuCl$_{2.8}$Br$_{1.2}$. a) Sample grown at 300 K and of tetragonal structure. b) and c) Sample with orthorhombic structure grown at 350 K without and with post-heated treatment, respectively.*

The data shown in panel (b) are of the sample that has no post-heated treatment before performing the measurements. The magnetization curve exhibits a change of its slope at the field around ~ 1.5 T and an anomaly is observed in *χ(T)* at about ~ 13 K, indicating the transition into an AFM state. These results are evidence for the existence of small amounts of the tetragonal phase in this sample. Meanwhile when this sample was post-heated at 450 K for 30 minutes, the data (shown

in panel (c)) show the typical behavior of the orthorhombic sample, as for the two border compounds, which shows a monotic increase of *M(B)* and a broad maximum in *χ(T)*. Thus, in our studies, large (100-1000 mm^3) and high-quality crystals with pure orthorhombic structure were carefully selected before doing the experiments, especially for the samples in the intermediate concentration range (1 < x < 2).

6.5 Magnetic properties of $Cs_2CuCl_{4-x}Br_x$

Fig. 6.5 shows a compilation of the results of the molar susceptibility $\chi_{mol}(T)$ taken at a field of 0.1 T of the $Cs_2CuCl_{4-x}Br_x$ (0 < *x* < 4) mixed system for temperatures 2 K ≤ *T* ≤ 20 K [Cong11]. The figure also includes the susceptibility data for the border cases Cs_2CuCl_4 (left panel, full dark green circles) and Cs_2CuBr_4 (right panel, black full squares), which are in accordance with literature results [Tokiwa06, Ono03].
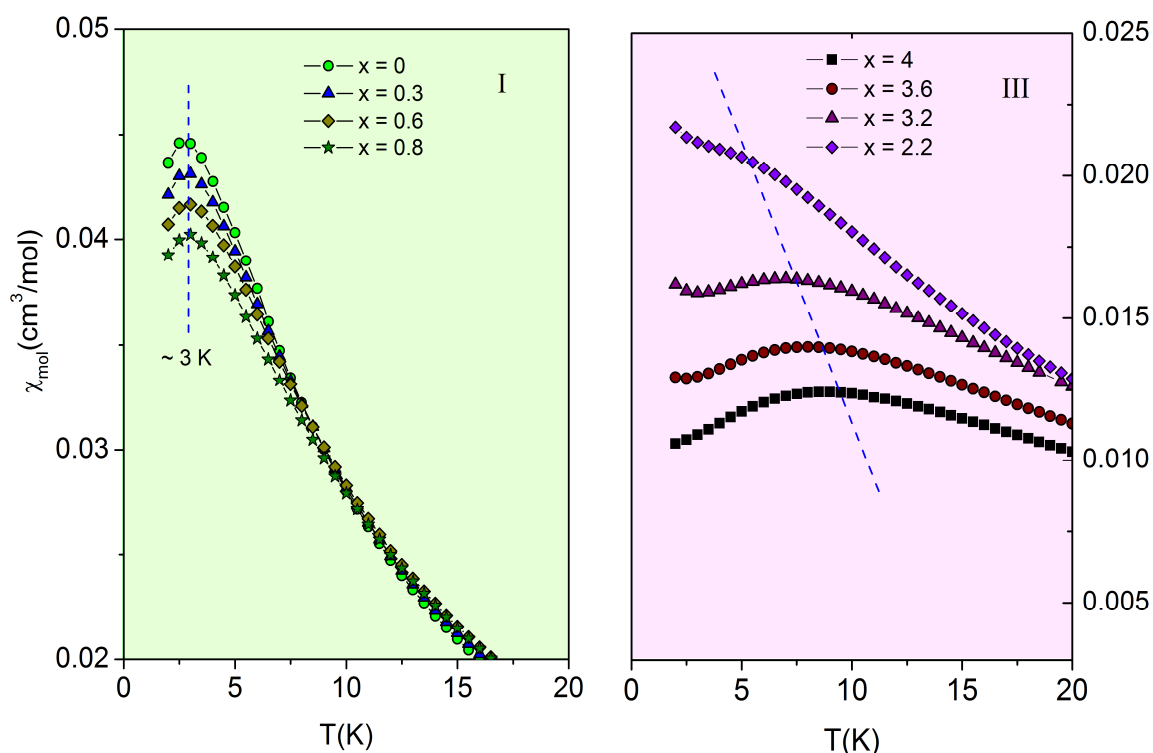
Figure 6.5 *Overview of the molar magnetic susceptibility of the mixed system $Cs_2CuCl_{4-x}Br_x$ (0 ≤ x ≤4) for selected Br concentrations measured at 0.1 T. Left panel: Cl-rich side regime I: x = 0 to x = 0.8, right panel: Br-rich side regime III: x =2.2 to x = 4. The broken blue line is a guide to the eye indicating T_{max}.*

The susceptibility curves of these two compounds reveal a continuous increase with decreasing temperature and a maximum at T_{max} = (2.79 ± 0.15) K for Cs$_2$CuCl$_4$ and (8.75 ± 0.1) K for Cs$_2$CuBr$_4$, which is distinctly broader for the latter compound. The maximum reflects the low-dimensional magnetic character of both materials in the temperature range under investigation. The left and right panel of Fig 6.5 exhibit data for the Cl-rich side, i.e. 0 ≤ x ≤ 1, and Br-rich side, i.e. 2 ≤ x ≤ 4, which will be labelled as regime I and regime III, respectively, in the following.
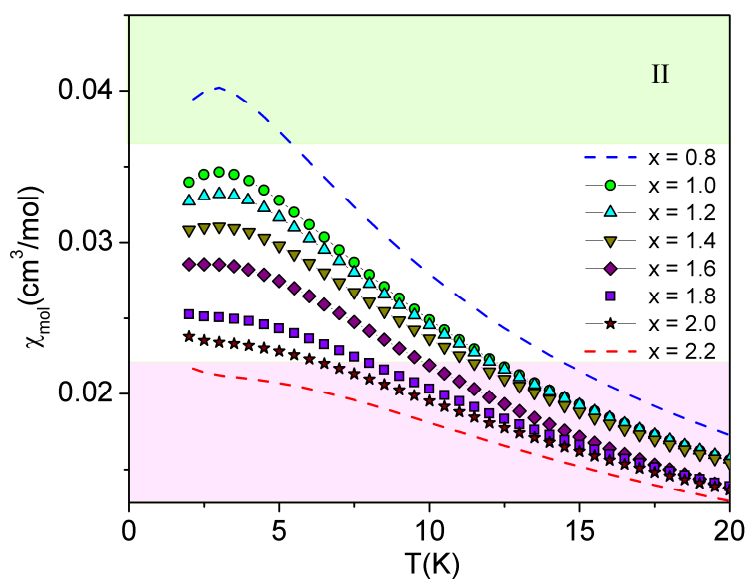
Figure 6.6 *χ$_{mol}$(T) in regime II for various Br concentrations x = 1.0 (full green circles) to x = 2.0 (full stars) in steps of x = 0.2. The blue and red broken lines show the χ$_{mol}$(T) data of x = 0.8 in regime I and x = 2.2 in regime III, respectively.*

The Fig. 6.6 displays the data of regime II in which the Br concentration x varies from 1 to 2. The data are taken in steps of x = 0.2. The Br concentration x = 0.8 in regime I and x = 2.2 in regime III are shown as dotted lines to indicate the change of the magnetic properties in between the two regimes.

The position of the susceptibility maximum and its height, T_{max} and $\chi_{mol}(T_{max})$, respectively, can be considered as a parameterization of the data, as seen in Fig. 6.5 and Fig. 6.6, also summarized and displayed in Fig. 6.7. It shows that there is no continuous evolution of the magnetic properties with increasing the Br concentration from x = 0 to 4. Rather, three distinct concentration regimes can be identified.

In regime I, $\chi_{mol}(T)$ has a temperature dependence which is very similar to that of the pure chlorine system x = 0. In fact, for the $Cs_2CuCl_{3.2}Br_{0.8}$, T_{max} of (3.03 ± 0.12) K is very close to the T_{max} of the x = 0 compound within the experimental uncertainties. With $\chi_{mol}(T_{max}) = 0.041$ cm^3/mol for x = 0.8, the value is reduced by slightly more than 10% compared to the pure chlorine (x = 0) system. This reduction of $\chi_{mol}(T_{max})$ is significantly larger than the experimental error bars.
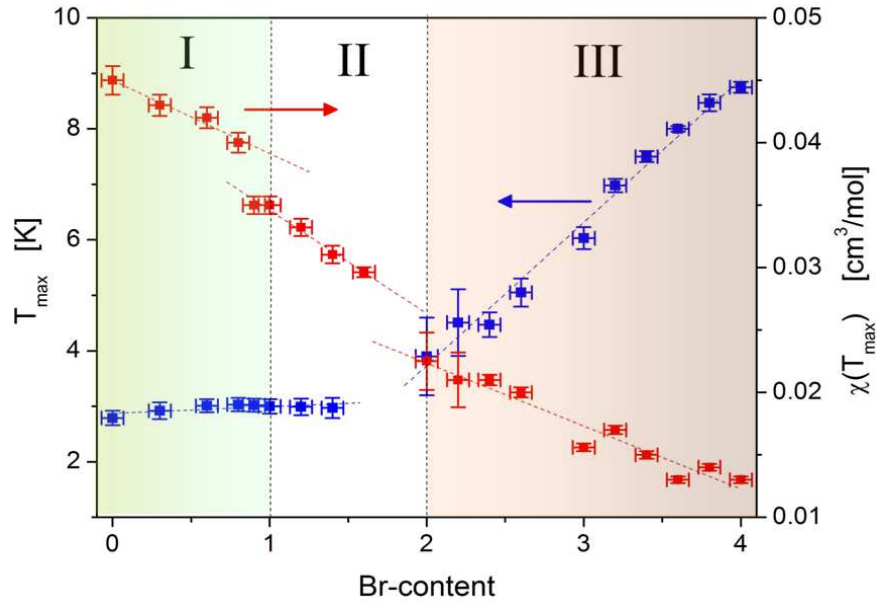
Figure 6.7: *T_{max} (blue solid squares, left axis) and $\chi_{mol}(T_{max})$ (red solid squares, right axis) as a function of the Br content x for all samples under investigation. The vertical dotted lines indicate the critical concentrations $x_{c1} = 1$ and $x_{c2} = 2$ separating the regimes I, II and III. The broken lines are linear fits to the experimental data in the three regimes.*

On the other hand, for the Br-rich side, regime III, a change of the Br-content by the same amount of $\Delta x = 0.8$ has a much stronger effect on T_{max} and $\chi_{mol}(T_{max})$. When considering $Cs_2CuCl_{0.8}Br_{3.2}$ (purple full up-turn triangles in Fig. 6.5), for example, the data reveal a pronounced shift of T_{max} to (6.92 ± 0.1) K accompanied by a strong increase of $\chi_{mol}(T_{max})$ by about 33% compared to the pure bromine system x = 4. Note that susceptibility data for the Br-rich side, i.e., 3.6 $\leq$ x $\leq$ 4.0, were also reported in Ref. [Ono05] for *B // c*-axis. We stress, however, that their data deviate from the results shown here with respect to the low-temperature upturn and its dependence on the Br concentration. These deviations might be the result of the entirely different preparation route applied in Ref. [Ono05] to synthesize the mixed systems. The difference of the value of $\chi(T_{max})$

is due to the g-factor anisotropy. Besides that, a peculiarity of the data for x = 3.2 in regime III is an upturn below about 3 K which grows with decreasing x and can be followed up to the border to regime II. Further experiments, in particular magnetic measurements at lower temperatures, have to clarify the origin of this feature.

Within the regime I and III, some variations in the magnetic properties with x become noticeable in the high-temperature tail of the susceptibility, i.e., for temperatures 10 K (~ 2J) $\leq T \leq$ 300 K. Here the data can be well described by a Curie-Weiss-type susceptibility $\chi_{cw} = C \cdot (T - \Theta_W)^{-1}$, with C the Curie constant and Θ_W the Weiss temperature, ranging from Θ_W = (-3.46 $\pm$ 0.1) K (x = 0) to Θ_W = (-5.71 $\pm$ 0.15) K (x = 0.8) in the regime I and from Θ_W = -18.4 K (x = 4) to Θ_W = -9.8 K (x = 1.9) in regime III.

In the regime II, the $\chi_{mol}(T_{max})$ decreases more rapidly with x compared to the reduction revealed in the regimes I and III, cf. also Fig. 6.7. In addition, the data suggest a discontinuous change of $\chi_{mol}(T_{max})$ upon entering regime I. A less clear situation is encountered at the border to regime III. With decreasing the Br-content to about half way of the whole Br-Cl concentration range in $Cs_2CuCl_{1.8}Br_{2.2}$ (purple squares in Fig. 6.6), the characteristics of the Br-rich materials (regime III) are nearly preserved. The shift of T_{max} to lower temperatures is accompanied by a further increase of $\chi_{mol}(T_{max})$. Note, that the broad maximum in the susceptibility is difficult to follow with increasing Br concentration due to the increase of the $\chi_{mol}(T)$ below 4 K. As a consequence, significantly enlarged error bars have to be accepted rendering the boundary between regime II and III less well defined.

The three distinct magnetic regimes in the $Cs_2CuCl_{4-x}Br_x$ (0 $\leq$ x $\leq$ 4) mixed system become obvious from Fig. 6.7, where the values for T_{max} (blue solid squares) and $\chi_{mol}(T_{max})$ (red solid squares) are shown as a function of the Br content x for all crystals investigated. On the chlorine-rich side in regime I and up to x slightly larger than 1.4, T_{max} is nearly independent of the Br-concentration, while $\chi_{mol}(T_{max})$ reveals a distinct reduction with x. The fact that the characteristic temperature T_{max} stays nearly constant indicates that the Br substitution in this concentration range leaves the quasi-2D magnetic fluctuations, caused by in-plane interactions, practically unaffected. At the same time, the significant reduction in $\chi_{mol}(T_{max})$ with increasing x demonstrates that the magnetic coupling between the layers is substantially modified. This is consistent with the results of *ab initio* calculations for the Cs_2CuCl_4, as shown in Fig. 6.8, where the influence of the strength of the interlayer coupling J'' on the magnetic properties was investigated [Foyevtsova09]. The authors

found a decrease in $\chi_{mol}(T_{max})$ with increasing J'' without any shift of T_{max}. In contrast, for the Br-rich side (regime III), the strong decrease of T_{max} by approximately a factor of 2 on decreasing x from 4 to 2 clearly signals the suppression of the 2D-magnetic correlations.
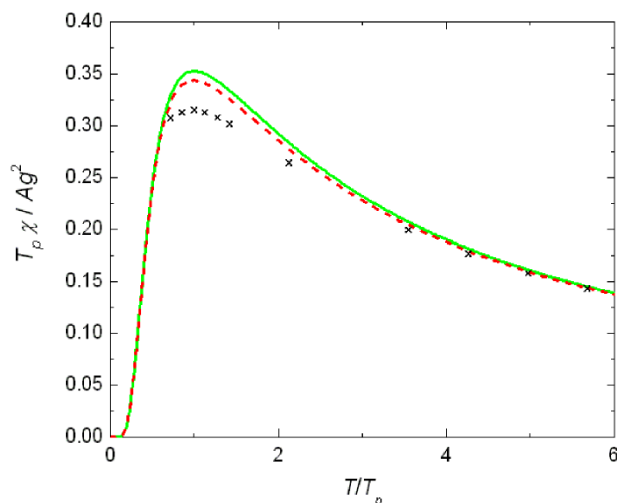
Figure 6.8 *Magnetic susceptibility of Cs_2CuCl_4 as a function of temperature in units of T_{max}. Green solid line: DFT-based model with only J_1 and J_2. Red dashed line: DFT-based model with J_1, J_2 and J_3. Crosses: experimental data (reprinted from Ref. [Foyevtsova09].*

6.6 Model

The magnetic properties of the $Cs_2CuCl_{4-x}Br_x$ ($0 \leq x \leq 4$) mixed systems and the corresponding three distinct magnetic regimes can be understood using the following model which considers structural features of the Cu-halide tetrahedra embedded in the orthorhombic crystal structure.

Upon replacing the Cl^- ions by Br^- on the chlorine-rich side (the regime I), the Cu-Cl1 bonds will be almost exclusively affected, as they exhibit the largest bond length and the Br^- ions are considerably bigger than the Cl^- ions. Since the Cu-Cl1 bonds point along the interlayer *a*-axis of the orthorhombic structure, they mediate the magnetic exchange J'' between the layers. Thus, starting from the pure Cs_2CuCl_4 compound, the progressive substitution of the Cl1 atoms by Br will be accompanied by an increase of J'', consistent with the decrease of the magnetic susceptibility at its maximum. This site-selective replacement of the Cl1 ions in regime I, which for a hypothetically ideal system would be completed at a concentration $x_{c1} = 1$, also explains that T_{max} is constant on the

chlorine-rich side of the phase diagram. The 2D magnetic correlations, probed by T_{max}, involve the Cl2/Cl3 atoms, the occupation factors of which remain (practically) unaffected for the Br substitutions in regime I for $x \leq x_{c1}$. It should be mentioned that due to entropic reason, the site-selective substitution will not be perfect, resulting in a finite disorder in the occupancy of the halide positions.

A quite different situation is encountered on the Br-rich side. Starting from the border case Cs_2CuBr_4 and substituting Br^- by the smaller Cl^- will predominantly affect the two equivalent Br3 positions with the shortest bond length. As a consequence, the intralayer coupling constants J and J', i.e., the 2D magnetic correlations, will be reduced. This mechanism explains the strong reduction of T_{max} as a function of Br content observed in the susceptibility measurement.

6.6.1 Supporting result

In addition, density-functional theory (DFT) calculations were carried out to estimate the preferential position of the Br atoms in the mixed ($x = 1$) compound Cs_2CuCl_3Br. The calculations were performed with the full potential local orbital code (FPLO, version 9.00-34) [Koepernik99] using the experimental lattice parameters and atom positions [Krüger10] as input. The local-density approximation (LDA) in the parametrization of Perdew and Wang [Perdew92] as well as the generalized gradient approximation (GGA) [Perdew92] were used to ensure that our conclusions do not depend on the choice of the functional approximation used. The calculations were performed in the scalar relativistic approximation with 216 **k** points in the full Brillouin zone.

The results show a clear preference for the substitution of Cl1 atoms by Br on the Cl-rich side: The occupation of Cl1 position in Cs_2CuCl_3Br yields the lowest total energy, whereas the energy of a structure where Br is substituted for Cl2 (Cl3) is about 222 (247) meV/Br higher in energy in the LDA calculations. In the GGA calculations, the corresponding energy differences are 244 (274) meV/Br, showing only a weak dependence on the choice of the functional. These calculations indicate that the sterical aspects, i.e., ionic radii and corresponding bond lengths, covered by the above simple model, are of crucial importance for stabilizing the structure in the $Cs_2CuCl_{4-x}Br_x$ ($0 \leq x \leq 4$) mixed system. The reason for that lies in the peculiarity of the Cu-halide tetrahedron, which forms a stable, discrete structural unit, typically found in aqueous solutions, and which is also only weakly bonded in the orthorhombic crystal structure of the $Cs_2CuCl_{4-x}Br_x$ ($0 \leq x \leq 4$) mixed system.
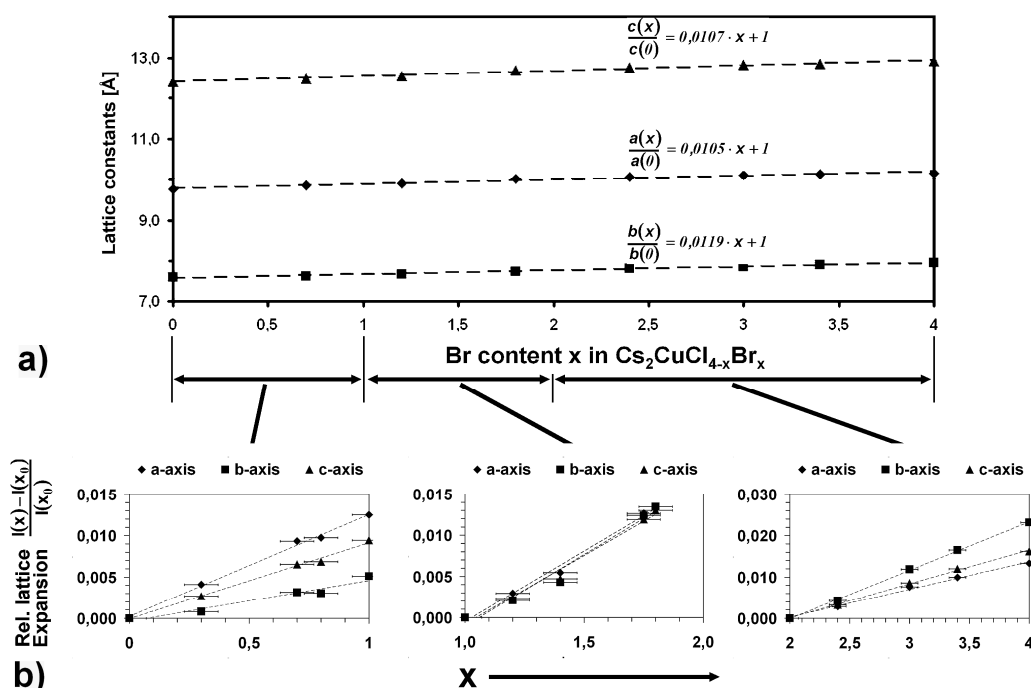
Figure 6.9 *Expansion of lattice constants with increasing Br-content: (a) Overview: Nearly linear expansion, indicating mainly that the crystalline structure is unaltered within the whole composition range. (b) The detailed view reveals specific expansion anisotropies for different composition ranges (reprinted from Ref. [Krüger10]).*

Another independent proof of this model based on the distribution of bond lengths inside the flattened Cu-halide tetrahedron is given by the relative length changes $[l(x) − l(x_0)]/l(x_0)$ of the lattice constants as a function of Br content. Here, $l(x)$ and $l(x_0)$ are the lattice constants of a mixed compound with concentration x and Cs_2CuCl_4 (x = 0), respectively. As shown in Fig 6.9, $[l(x) − l(x_0)]/l(x_0)$ is isotropic in the concentration range $1 \leq x \leq 2$ (regime II) and anisotropic in the regimes I and III. With increasing x for $0 \leq x \leq 1$, the relative expansion of the a-axis is largest, consistent with a predominant substitution of the Cl1 positions by Br whereas on the Br-rich side $2 \leq x \leq 4$, the Cl doping on the two Br3 positions leads to the strongest reduction of the b axis.

<div align="center">

7

CONCLUSIONS AND OUTLOOK

</div>

In this thesis, ultrasound was used as the main experimental technique to perform a comprehensive study on the acoustic characteristics of some low-dimensional spin systems in a wide range of temperature (30 mK$< T <$ 300 K) and magnetic field (DC field: B $\leq$ 12 T and pulsed fields up to 35 T). We have conducted experimentally a thorough investigation about the acoustic and magnetic properties of two classes of materials placing special emphasis on the effect of a nearby quantum phase transition induced by a magnetic field: (1) the quasi-1D frustrated diamond chain compound Azurite; (2) The quasi-2D quantum spin systems Cs_2CuCl_4, Cs2CuBr$_4$ and the mixed system $Cs_2CuCl_xBr_{4-x}$.

7.1 The quasi-1D frustrated diamond chain compound Azurite

Thorough elastic and magneto-acoustic investigations of the c_{22} mode of a single crystal of the distorted diamond chain compound Azurite have been presented. We have observed clear signatures of the dominant magnetic energy scales involved and disclose two pronounced anomalies at ~ 20 K and ~ 5 K in the temperature dependences of the sound velocity and thermal expansion measurements. These results are consistent with the ones obtained from magnetic susceptibility and specific heat measurements. At the transition into the antiferromagnetic (AFM) long-range ordered state, T_N ~ 1.88 K, we observed a huge anomaly in the sound velocity ($\Delta v/v$ ~ 0.1%) and thermal expansion ($\beta(T)$ ~ $600 \cdot 10^{-6}$ K^{-1}) that indicates a sizable structural distortion accompanying the occurrence of long-range AFM order. Inside the long-range AFM-ordered state, we also observed a huge softening of the c_{22} mode (up to 1% at 0.85 K) as a function of applied magnetic field indicating a strong magneto-elastic interaction in the AFM-ordered state.

Based on these results, we have estimated of the strain dependence of the dominant magnetic exchange coupling by analyzing the temperature dependence of the elastic constant that reveals a considerable dimer-dimer coupling constant and a large strain dependence of the singlet-triplet gap. Moreover, the pressure dependence of the magnetic susceptibility was investigated up to 6.2 kbar using a SQUID magnetometer. The results are in agreement with the value of the strain dependence

<div align="center">

113

</div>

indicating the significant role of strain interactions in this compound. From these results, we emphasize that Azurite can be well described by a 1D diamond chain system at temperatures above 2 K [Jeschke11]. However, a strong magneto-elastic coupling must be taken into account in the "full model" Hamiltonian for describing the low-temperature region, including the 3D long-range AFM order.

Further, we have presented a detailed investigation of the critical behavior of the sound velocity and ultrasonic attenuation in the vicinity of T_N. The results show that the attenuation shift obeys a power law both above and below T_N with a critical exponent of about 1.12 and 5.22, respectively. The value obtained above T_N is close to the theoretical expectation of $\eta \sim 1$ for the isotropic Heisenberg antiferromagnet but the extraordinary large value obtained below T_N is not clear at present. The critical contribution of the sound velocity shows the same critical exponent of -0.056 both above and below T_N is indicative of a 3D isotropic Heisenberg antiferromagnet.

. In an applied magnetic field, the critical velocity changes exhibit a uniform behavior for various fields, indicating a similar nature of the critical contribution when crossing from the paramagnetic to the antiferromagnetic or to the spin-flop state.

The measurements at low temperature show a complex magnetic structure of Azurite. Based on these measurements, detailed low-temperature B-T phase diagrams were mapped which comprise two additional new phase boundaries of unknown origin at low temperature ($T < T_N$). One is just below the AFM ordering transition, and the other one is at very low temperature ($T < 0.5$ K) which is likely to be of magnetic origin. So, further investigations are needed in order to clarify this issue.

7.2 The quasi-2D quantum spin systems Cs_2CuCl_4 and Cs_2CuBr_4

We have conducted thorough magneto-acoustic investigations of Cs_2CuCl_4 for all three modes c_{11}, c_{22} and c_{33} with the magnetic field applied along the crystallographic a-axis.

In the field-dependent measurements, we observed a change of the shape of the attenuation curves from a broad feature to a sharp anomaly which is attributed to driving the system from a spin liquid to long-range AFM order. Moreover, field-dependent measurements around B_s display two distinct anomalies which are particularly clearly pronounced in the sound attenuation. While the first one is very sharp and strongly temperature dependent, the other one is distinctly broader and located at slightly higher fields. These features have been tentatively attributed to the transition into long-range AFM order and the preceding spin-liquid state. These two anomalies in the sound attenuation

$\alpha(B)$ merge up as $T \rightarrow 0$. These pronounced acoustic anomalies indicate a particularly strong spin-lattice interaction in this material, a quantitative understanding of the interplay of spin-lattice interaction and quantum criticality is still missing.

Our experimental data, again, indicate that in Cs_2CuCl_4, the field dependence of the critical temperature $T_c(B) \sim (B_c - B)^{1/\Phi}$ yields a critical field $B_c = 8.422$ T and is well described by $\Phi = 1.47$. This is in very good agreement with the exponent expected in the mean-field approximation and the result published previously. This finding again supports the notion of a BEC of magnons in Cs_2CuCl_4.

Theoretical calculations were performed by our collaborator and were used to compare with experimental results for the magnetic field dependence of the elastic constants and the ultrasonic attenuation in the AFM ordered state. The results for the magnetic field dependence of the elastic constants agree quite well with the experimental data, in particular in the low-field regime $B \leq 2.5$ T, where the approach is expected to be most accurate. The theoretical results for the ultrasonic attenuation reproduce the strong enhancement observed close to the critical magnetic field, although this approach is likely to break down in the vicinity of the quantum-critical point. The investigation of magnon-phonon interactions in the immediate vicinity of the quantum-critical point and in the other phases of Cs_2CuCl_4 such as the spin-liquid phase or the ferromagnetic phase is left for future work.

Based on the temperature and field-dependent measurements, we constructed, in details, the *B-T* phase diagram of Cs_2CuCl_4 for the field applied along the *a*-axis that agreed with the one obtained from specific heat and magnetocaloric data. The phase diagram reveals the low-temperature crossover phase boundary of the spin liquid that has been missing up to now.

Pulse-field measurements also have been performed in Cs_2CuBr_4 in order to study the acoustic behavior in the region of the magnetization plateau. Unfortunately the available temperature range of the study was confined to the paramagnetic state ($T > 1.5$ K) and could not be extended to the region where the plateaux exist. The results show a gradual softening of $c_{11}(B)$ on increasing the field and display a *step-like* phase transition when the field reaches the saturation, regardless of the applied field direction.

In Ref. [Ono07], T. Ono reported an attempt to perform ultrasound measurements in high pulsed magnetic fields but without success due to cracks in the sample. Our measurements have proved that

the high-quality samples, provided by Prof. Assmus and his team, can survive at low temperatures and high fields. In future, we are going to carry out measurements at low temperatures and high DC magnetic fields in collaboration with the High Field Laboratory in Dresden.

7.3 The mixed system $Cs_2CuCl_xBr_{4-x}$

The mixed crystal series $Cs_2CuCl_{4-x}Br_x$ were successfully synthesized by growing from aqueous solutions and were magnetically characterized in the present work. We have performed magnetic susceptibility measurements on the whole range of single crystals of the mixed system in the orthorhombic phase. By following characteristic features of the susceptibility, including the position of the broad maximum at T_{max} and the height of the maximum $\chi_{mol}(T_{max})$, three distinct magnetic regimes have been identified. These regimes are separated by critical concentrations around $x_{c1} = 1$ and $x_{c2} = 2$. The main magnetic characteristics of the systems and the existence of two critical concentrations could be explained by a model which considers the structural peculiarities of the Cu-halide tetrahedra and the way these building blocks are arranged in the crystal structure.

According to this model, the substitution of the smaller Cl$^-$ ions by the larger Br$^-$ ions in the distorted Cu-halide tetrahedron enforces a site-selective occupation. This mechanism provides a natural explanation for the two critical concentrations: While at $x_{c1} = 1$, (practically) all the Cl1 positions are occupied by Br, the two equivalent Br3 atoms are displaced by Cl atoms at $x_{c2} = 2$. Thus our results suggest that $Cs_2CuCl_3Br_1$ and $Cs_2CuCl_2Br_2$ mark particularly interesting mixed systems with a well-ordered local Cu environment providing a suitable basis for studying the interplay between strong frustration and quantum criticality.

In the near future, one target is to explore the low-temperature magnetic properties, especially the evolution of the Néel temperature as a function of concentration x, by performing high-resolution ac-susceptibility measurements for $T < 2$ K on the various $Cs_2CuCl_{4-x}Br_x$ single crystals. Due to the increase of the degree of frustration for the Br-rich materials, we expect a sizable suppression of T_N. We expect that due to strong frustration around x_{c2}, $Cs_2CuCl_2Br_2$ should show long-range antiferromagnetic order at T_N below that of the pure Cl (x = 0) system ($T_N = 0.62$ K), and would represent an interesting target material for studying the interplay of strong magnetic frustration and quantum criticality.

In addition, the question arises to which extent the system becomes more 3D in character on the Cl-rich side. This could be answered by studying the field dependence of T_N through $\chi(T,B)$

measurements, in order to determine the *B-T* phase diagrams and to identify the nearby QCP. Of particular interest will be the compounds with $x_{c1} = 1$ and $x_{c2} = 2$. In order to fully characterize the criticality and to study the effects of frustration and dimensionality on the quantum-critical behavior, it is necessary to employ various measurements such as magnetocaloric effect, specific heat, thermal expansion and ultrasound in the millikevin temperature range in combination with theoretical studies such as *ab*-initio and DRMG calculations.

7.4 In summary

We have conducted detailed studies of acoustic behavior and magnetic properties on some low-dimensional spin systems. Our obtained results bring new insight into the thermodynamical properties, especially at the field-induced quantum phase transitions and at the QCP. The comparison of our data with other experimental results shows that we were able to reproduce and improve their quality. In exploring different compounds, e.g., 1D, 2D or a mixed solution of quantum spin systems, besides being in the agreement with current results, many of our results point out new directions for further studies in both theoretical and experimental field.

BIBLIOGRAPHY

.

[Anderson73]   P.W. Anderson, *Mater. Res. Bull.* **8**, 153 (1973).

[Aeppli97]   G. Aeppli, T. E. Mason, S. M. Hayden, H. A. Mook, and J. Kulda, *Science* **278**, 14321435 (1997).

[Aimo09]   F. Aimo, S. Krämer, M. Klanjšek, M. Horvatić, C. Berthier, and H. Kikuchi, *Phys. Rev. Lett.* **102**, 127205 (2009).

[Bethe31]   H. Bethe, *Z. Physik* **71**, 205 (1931).

[Bonner64]   J. C. Bonner and M. E. Fisher, *Phys. Rev.* **135**, A640 (1964).

[Bennett67]   H. S. Bennett and E. Pytte, *Phys. Rev.* **155**, 553 (1967).

[Bennett69a]   H. S. Bennett, *Phys.Rev.* **181**, 978 (1969).

[Bennett69b]   H. S. Bennett, *Phys. Rev.* **185**, 801 (1969).

[Bailleul91]   S. Bailleul, D. Svoronos, P. Porcher, A. Tomas, *Comptes Rendus* **313**, 1149 (1991).

[Blundell01]   S. Blundell. *Magnetism in Condensed Matter*. Oxford University Press, 2001.

[Belokoneva01]   E. L. Belokoneva *et al.*, *Phys. Chem. Miner.* **28**, 498 (2001).

[Bramwell01]   S. T. Bramwell, M. J. P., and Gingras, *Science* **294**, 1495 (2001).

[Brück03]   E. Brück, O. Tegus, X. W. Li, F. R. de Boer and K. H. J. Buschow, *Phys. Rev. B* **327**, 431 (2003).

[Batista07]   C. D. Batista, J. Schmalian, N. Kawashima, P. Sengupta, S. E. Sebastian, N. Harrison, M. Jaime, I. R. Fisher, *Phys. Rev. Lett.* **98**, 257201 (2007).

[Brüehl08]   A. Bruehl, *PhD thesis* (2008), University of Frankfurt.

[Carlin85]   R.L. Carlin, R. Burriel, F. Palacio, R.A. CArlin, S.F. Keij, and D.W. Carnegier, *J. Appl. Phys.* **57**, 3351 (1985).

[Capriotti99]   L. Capriotti, A. E. Trumper, and S. Sorella, *Phys. Rev. Lett.* **82**, 3899 (1999).

[Coldea96]   R. Coldea, D. A. Tennant, R. A. Cowley, D. F. McMorrow, B. Dorner, and Z. Tylczynski, *J. Phys. Condens. Matter* **8**, 7473 (1996).

[Coldea97]   R. Coldea, D.A. Tennant, R.A. Cowley, D.F McMorrow, B. Dorner, and Z. Tylczynski.*Phys. Rev. Lett.* **79,** 151 (1997).

Bibliography

[Coldea01]	R. Coldea, D. A. Tennant, A. M. Tsvelik, and Z. Tylczynski, *Phys. Rev. Lett.* **86**, 1335 (2001).
[Coldea02]	R. Coldea, D. A. Tennant, K. Habicht, P. Smeibidl, C.Wolters, and Z. Tylczynski, *Phys. Rev. Lett.* **88**, 137203 (2002).
[Coldea03]	R. Coldea, D.A. Tennant, and Z. Tylczynski, *Phys. Rev. B* **68**, 34424 (2003).
[Chalker07]	J. T. Chalker, *Highly Frustrated Magnetism* (2007), Lecture notes for Trieste Summer School, August 2007.
[Castelnovo08]	C. Castelnovo, R.Moessner, and S. L. Sondhi, *Nature* **45**, 42 (2008).
[Cong11]	P. T. Cong, B. Wolf, M. de Souza, N. Krüger, A. A. Haghighirad, S. Gottlieb-Schoenmeyer, F. Ritter, W. Assmus, I. Opahle, K. Foyevtsova, H. O. Jeschke, R. Valenti, L. Wiehl, and M. Lang, *Phys. Rev. B* **83,** 064425 (2011).
[Drung96]	D. Drung, H. Weinstock, Editor, *SQUID Sensors: Fundamentals, Fabrication and Application*, Kluwer, Dordrecht (1996).
[Enss05]	C. Enss, S. Hunklinger, *Low-temperature physics,* Springer, Berlin, 2005.
[Farnell09]	G. J. J. Farnell, R. Zinke, J. Schulenburg and J. Richter, *J. Phys.: Condens. Matter* **21**, 406002 (2009).
[Fortune09]	N. A. Fortune, S. T. Hannahs, Y. Yoshida, T. E. Sherline, T. Ono, H. Tanaka, and Y. Takano, *Phys. Rev. Lett.* **102,** 257201 (2009).
[Foyevtsova09]	K. Foyevtsova, Y. Z. Zhang, H. O. Jeschke, and R. Valenti*, J. Phys.: Conf. Ser.* **145**, 012038 (2009).
[Gattow58]	G. Gattow and J. Zemann, *Acta Crystallogr.* **11**, 866 (1958).
[Giamarchi99]	T. Giamarchi and A. M. Tsvelik, *Phys. Rev. B* **59**, 11398 (1999).
[Giamarchi08]	T. Giamarchi, Ch. Rüuegg and O. Tchernyshyov, *Nature Physics* **4**, 893 (2008).
[Greedan01]	J. E. Greedan, *J. Mater. Chem.* **11**, 37 (2001).
[Gershoni06]	D. Gershoni, *Nature Materials* **5**, 255 (2006).
[Gu06]	B. Gu and G. Su, *Phys. Rev. Lett.* **97**, 089701 (2006).
[Gu07]	B. Gu and G. Su, *Phys. Rev. Lett.* **75**, 174437 (2007).
[Gibson10]	M. C. R. Gibson, K. C. Rule, A. U. B. Wolter, J. -U. Hoffmann, O. Prokhnenko, D. A. Tennant, S. Gerischer, M. Kraken, F. J. Litterst, S. Süllow,

J. Schreuer, H. Luetkens, A. Brühl, B. Wolf, M. Lang, *Phys. Rev. B.* **81,** 140406(R) (2010).

[Heisenberg28]   W. Heisenberg, *Zeit. Phys.* **49,** 619 (1928).

[Honecker01]   A. Honecker and A. Läuchli, *Phys. Rev. B* **63**, 174407 (2001).

[Heidarian05]   D. Heidarian and K. Damle, *Phys. Rev. Lett.* **95**, 127206 (2005).

[Hida05]   K. Hida and I. Affleck, *J. Phys. Soc. Jpn.* **74**, 1849 (2005).

[Ising25]   E. Ising, *Z. Physik* **31**, 253 (1925).

[Ikushima71]   A. Ikushima and R. Feigelson, *J. Phys. Chem. Solids* **32**, 417 (1971).

[Jeschke11]   H. Jeschke, I. Opahle, H. Kandpal, R. Valentí, H. Das, T. Saha-Dasgupta, O. Janson, H. Rosner, A. Brühl, B. Wolf, M. Lang, J. Richter, S. Hu, X. Wang, R. Peters, T. Pruschke, A. Honecker, *Phys. Rev. Lett.* **106,** 217201 (2011).

[Kawaski68]   K. Kawaski, *Phvs. Left.* **26A**, 543 (1968).

[Kadanoff69]   L. P. Kadanoff, *J. Phys. Soc. Japp. Suppl.* **26***, 122* (1969).

[Kawasaki70]   K. Kawasaki and A. Ikushima, *Phys. Rev. B* **1**, 3143 (1970).

[Keimer91]   B. Keimer, R. J. Birgeneau, A. Cassanho, Y. Endoh, R. W. Erwin, M. A. Kastner, and G. Shirane, *Phys. Rev. Lett.* **67**, 19301933 (1991).

[Koepernik99]   K. Koepernik and H. Eschrig, *Phys. Rev. B* **59**, 1743 (1999).

[Kikuchi05a]   H. Kikuchi, Y. Fujii, M. Chiba, S. Mitsudo, T. Idehara, T. Tonegawa, K. Okamoto, T. Sakai, T. Kuwai, and H. Ohta , *Phys. Rev. Lett.* **94**, 227201 (2005).

[Kikuchi05b]   H. Kikuchi, Y. Fujii, M. Chiba, S. Mitsudo, T. Idehara, T. Tonegawa, K. Okamoto, T. Sakai, T.o Kuwai, K. Kindo, A. Matsuo, W. Higemoto, K. Nishiyama, M. Horvatić and C. Bertheir, *J. Phys. Soc. Jpn. Suppl.* ***159, 1*** (2005).

[Kittel05]   C. Kittel, *Introduction to Solid State Physics*, *8th Edition* (2005).

[Krämer06]   Conference presentation, *Low Energy Excitation in Solid* 2006 (LEES06).

[Kang09]   J. Kang, C. Lee, R K Kremer and M-H Whangbo, *J. Phys. Condens. Matter* **21**, 392201 (2009).

[Krüger10]   N. Krüger, S. Belz, F. Schassau, A. A. Haghighirad, P. T. Cong, B. Wolf, S. Gottlieb-Schoenmeyer, F. Ritter, W. Assmus, *Cryst. Growth Design* **10**, 4456 (2010).

Bibliography

[Kreisel11]	A. Kreisel, P. Kopietz, P. T. Cong, B. Wolf, and M. Lang, *Phys. Rev. B.* **84**, 024414 (2011).
[Landau59]	L. D. Landau and E. M. Lifshitz, *Theory of Elasticity,* (Pergamon Press Ltd., 1959).
[Love70]	N. D. Love, T. K. Duncan, P. T. Bailey and H. Forstat, Phys. Lett. **33A,** 290 (1970).
[Lüther75]	A. Luther and I. Peschel, *Phys. Rev. B* **12**, 3908 (1975).
[Lhuillier02]	C. Lhuillier and G. Misguich, *Lect. Notes Phys.* **595**,161-190 (2002).
[Lüthi68]	B. Lüthi and R.J. Pollina, *Phys. Rev.* **167**, 488 (1968).
[Lüthi69]	B. Lüthi and R.J. Pollina, *Phys. Rev. Lett.* **22**, 717 (1969).
[Lüthi70]	B. Lüthi, T. J. Moran and R. J. Pollina, *J. Phys. Chem. Solids* **31,** 1741 (1970).
[Lüthi94]	B. Lüthi, G. Bruls, P. Thalmeier, B.Wolf, D. Finsterbusch, and I. Kouroudis, *J. Low Temp. Phys.* **95**, 257 (1994).
[Lüthi05]	B. Lüthi, *Physical Acoustics in the Solid State*, (Springer, 2005).
[Lang06]	M. Lang, A. Brühl, V. Pashchenko, K. Removic-Langer, Y. Tsui, U. Tutsch,B. Wolf, T. Kretz, W. Lerner, M. Wagner and J. Schreuer, *J. Phys. Conf. Ser.* **51**, 1 (2006).
[Lee10]	S. B. Lee, Kaul R K, L. Balents, *Nature Phys.* **6**, 702 (2010).
[Mriano09]	Data are supplied from Mriano de Souza, University of Frankfurt.
[Matsubara56]	T. Matsubara and H. Matsuda, *Prog. Theor. Phys.* **16**, 569 (1956).
[Morosin61]	B. Morosin, E. C. Lingafelter, *J. Phys. Chem.* **65**, 50 (1961).
[Mermin66]	N. D. Mermin and H. Wagner, *Phys. Rev. Lett.* **17**,1133 (1966).
[McGinnety72]	J. A. McGinnety, *J. Am. Chem. Soc.* **94**, 8406, (1972).
[Manousakis91]	E. Manousakis, *Rev. Mod. Phys.* **63,** 1 (1991).
[Misguich01]	G. Misguich and C. Lhuillier, *Lecture notes of the Cargese summer school on "Trends in high magnetic field science"*, (2001).
[Moessner01]	Moessner, *Can. J. Phys.* **79**, 1283 (2001).
[Misguich04]	G. Misguich and C. Lhuillier, *Frustrated Spin Systems*, World-Scientific (2004).
[Mikeska04]	H,-J. Mikeska and A. K. Kolezhuk, *Lecture Notes in Physics* **64** (2004).

Bibliography

[Mikeska08]   H,-J. Mikeska and C. Luckmann, *Phys. Rev. B* **77**, 054405 (2008).

[Melko05]   R. G. Melko, A. Paramekanti, A. A. Burkov, A. Vishwanath, D. N. Sheng, and L. Balents, *Phys. Rev. Lett.* **95**, 127207 (2005).

[Nikuni00]   T. Nikuni, M. Oshikawa, A. Oosawa, H. Tanaka, *Phys. Rev. Lett.* **84**, 5868 (2000).

[Nohadani04]   O. Nohadani *et al.*, *Phys. Rev. B* **69**, 220402(R) (2004).

[Okamoto99]   K. Okamoto, T. Tonegawa, Y. Takahashi and M. Kaburagi, *J. Phys.: Condens. Matter* **11,** 10485 (1999).

[Okamoto03]   K. Okamoto, T. Tonegawa and M. Kaburagi, *J. Phys.: Condens. Matter* **15,** 5979 (2003).

[Oosawa99]   A. Oosawa, M. Ishii, and H. Tanaka, *J. Phys. Condens. Matter* **11**, 265 (1999).

[Ong04]   N. P. Ong and R. J. Cava, *Science* **305**, 52 (2004).

[Ono03]   T. Ono, H. Tanaka, H. Aruga Katori, F. Ishikawa, H.Mitamura, and T. Goto, *Phys. Rev. B* **67**, 104431 (2003).

[Ono04]   T. Ono, H. Tanaka, O. Kolomiyets, H. Mitamura, T. Goto, K. Nakajima, A. Oosawa, Y. Koike, K. Kakurai, J. Klenke, P. Smeibidle and M. Meißner, *J. Phys. Condens. Matter* **16**, S773 (2004).

[Ono05]   T. Ono, H. Tanaka, T. Nakagomi, O. Kolomiyets, H. Mitamura, F. Ishikawa, T. Goto, K. Nakajima, A. Oosawa, Y. Koike, K. Kakurai, J. Klenke, P. Smeibidle, M. Meißner, and H. A. Katori, *J. Phys. Soc. Jpn., Suppl.* **74**, 135 (2005).

[Ono07]   T. Ono, research report, *National high magnetic field laboratory* (2007).

[Okubo05]   S. Okubo, A. Taketani, H. Ohta, T. Kunimoto, Y. Inagaki, T. Saito, M. Azuma, M. Takano and H. Kikuchi, *Prog. Theo. Phys. Suppl.* **159,** 11 (2005).

[Lang11]   Theortical study found that in the system which have strong magneto-elastic coupling at phase transition will show a significant deviation of critical behavior as T $\rightarrow$ T_N (private communication with Prof. Lang in group meeting).

[Pott83]   R. Pott and R. Schefzyk, *J. Phys. E* **16**, 444 (1983).

[Perdew92]   J. P. Perdew and Y. Wang, *Phys. Rev. B* **45**, 13244 (1992).

[Pelissetto02]   A. Pelissetto and E. Vicarib, *Phys. Rep.* **368**, 549 (2002)

[Pobell07]   F. Pobell, *Matter and Methods at Low Temperatures*, (Springer, 2007).

Bibliography

[Rice02]	T. M. Rice, *Lect. Notes Phys.* **595**,139 (2002).
[Rüegg03]	Ch. Rüegg, N. Cavadini, A. Furrer, H.-U. Güdel, K. Krämer, H. Mutka, A. Wildes, K. Habicht, P. Vorderwisch, *Nature* **423**, 62 (2003).
[Richter04]	J. Richter, J. Schulenburg, and A. Honecker, *Quantum Magnetism, Lecture Notes in Physics* Vol. 645, Chap. 2, p. 85, Springer, 2004.
[Radu05]	T. Radu, H. Wilhelm, V. Yushankhai, D. Kovrizhin, R. Coldea, Z. Tylczynski, T. Lühmann, and F. Steglich, *Phys. Rev. Lett.* **95**, 127202 (2005).
[Radu07]	T. Radu, Y. Tokiwa, R. Coldea, P. Gegenwart, Z. Tylczynski and F. Steglich, *Sci. Technol. Adv. Mater.* **8,** 406 (2007).
[Rule08]	K. C. Rule, A. U. B. Wolter, S. Süllow, D. A. Tennant, A. Brühl, S. Köhler, B. Wolf, M. Lang, and J. Schreuer, *Phys. Rev. Lett.* **100**, 117202 (2008).
[Sharnoff65]	M. Sharnoff, *J. Chem. Phys.* **42**, 3383 (1965).
[Stern65]	H. Stern, *J. Phys. Chem. Solids* **26**, 153 (1965).
[Schiltz74]	R. J. Schiltz and J. F. Smith, *J. Appl. Phys.* **45**, 4681 (1974).
[Sorensen93]	E. Sorensen and I. Affeck, *Phys. Rev. Lett.* **71**, 1633 (1993).
[Sachdev99]	S. Sachdev, *Quantum Phase Transitions, Cambridge University Press* (1999).
[Shiramura97]	W. Shiramura, K. Takatsu, H. Tanaka, K. Kamishima, M. Takahashi, H. Mitamura, and T. Goto, *J. Phys. Soc. Jpn.* **66**, 1900 (1997).
[Schröder00]	A. Schröder, G. Aeppli, R. Coldea, M. Adams, O. Stockert, H.v. Löhneysen, E. Bucher, R. Ramazashvili and P. Coleman, *Nature* **407**, 351355 (2000).
[Sebastian06]	S. E, Sebastian, N. Harrison, C. D. Batista, L. Balicas, M. Jaime, P. A. Sharma, N. Kawashima, I. R. Fisher, *Nature* **441**, 617 (2006).
[Sherman03]	E. Ya. Sherman, P. Lemmens, B. Busse, A. Oosawa, and H. Tanaka, *Phys. Rev. Lett.* **91**, 057201 (2003).
[Sakai09]	T. Sakai, K. Okamoto and T. Tonegawa, *J. Phys.: Conf. Ser.* **145** 012065 (2009).
[Sytcheva10]	A. Sytcheva , O. Chiatti, J. Wosnitza, S. Zherlitsyn , A. A. Zvyagin, R. Coldea and Z. Tylczynski, *J. Low Temp. Phys.* **159,** 109 (2010).
[Tani66]	K. Tani and H. Mori, *Phys. Lett.* **19**, 627 (1966).
[Toulouse77]	G. Toulouse, Commun. *Phys.* **2**, 115 (1977).

Bibliography

[Tylczyński92]   Z. Tylczyński, P. Piskunowicz, A. N. Nasyrov, A. D. Karaev, Kh. T. Shodiev, G. Gulamov, *Phys. Stat. Sol.* **133,** 33 (1992).

[Takano00]   K. Takano, K. Kubo, and H. Sakamoto, *J. Phys.: Condens. Matter* **8**, 6405 (1996).

[Tonegawa00]   T. Tonegawa, K. Okamoto, T. Hikihara, Y. Takahashi, and M. Kaburagi, *J. Phys. Soc. Jpn.* **69**, 332 (2000).

[Tonegawa01]   T. Tonegawa, K. Okamoto, T. Hikihara, Y. Takahashi and M. Kaburagi, *J. Phys. Chem. Solids* **62,** 125 (2001).

[Tanaka02]   H. Tanaka, T. Ono, H. Aruga Katori, H. Mitamura, F. Ishikawa, and T. Goto, *Prog. Theor. Phys. Suppl.* **145**, 101 (2002).

[Tegus02]   O. Tegus, E. Brück, K. H. J. Buschow and F. R. de Boer, *Nature* **415**, 150 (2002).

[Tokiwa06]   Y. Tokiwa, T. Radu, R. Coldea, H. Wilhelm, Z. Tylczynski, and F. Steglich, *Phys. Rev. B* **73**, 134414 (2006).

[Tsujii07]   H. Tsujii, C. R. Rotundu, T. Ono, H. Tanaka, B. Andraka, K. Ingersent, and Y. Takano, *Phys. Rev. B* **76**, 060406(R) (2007).

[Varshny70]   Y.P. Varshny, *Phys. Rev. B* **2**, 3952 (1970).

[Villain80]   J. Villain, R. Bidaux, J. Carton, and R. Conte, J. Physique (Paris) **41**, 1263 (1980).

[Vojta03]   M. Vojta, *Rep. Prog. Phys.* **66**, 2069 (2003).

[Wessel05]   S. Wessel and M. Troyer, *Phys. Rev. Lett.* **95**, 127205 (2005).

[Wolf00]   B. Wolf, S. Schmidt, H. Schwenk, S. Zherlitsyn, and B. Lüthi, *J. Appl. Phys.* **87**, 7055 (2000).

[Wolf01a]   B. Wolf, S. Zherlitsyn, S. Schmidt, B. Lüthi, H. Kageyama, and Y. Ueda, *Phys. Rev. Lett.* **86,** 4847 (2001)**.**

[Wolf01b]   B. Wolf, B. Lüthi, S. Schmidt, H. Schwenk, M. Sieling, S. Zherlitsyn, I. Kouroudis, *Physica B* **294,** 612 (2001).

[Wolff-Fabris09]   F. Wolff-Fabris, S. Francoual, V. Zapf, M. Jaime, B. Scott, S. Tozer, S. Hannahs, T. Murphy and A. Lacerda, *J. Phys. Conf. Ser.* **150**, 042030 (2009).

[Wolf11]   B. Wolf, Y. Tsui, D. Jaiswal-Nagar, U. Tutsch, A. Honecker, K. Remović-Langer, G. Hofmann, A. Prokofiev, W. Assmus, G. Donath and M. Lang, *Proc. Natl. Acad. Sci. USA* **108(17)** 6862 (2011).

[Zigan72]   F. Zigan and H. D. Schuster, *Z. Kristallogr.* **135**, 416 (1972).

[Zherlitsyn00]   S. Zherlitsyn, S. Schmidt, B. Wolf, H. Schwenk, B. Lüthi, H. Kageyama, K. Onizuka, Y. Ueda, and K. Ueda, *Phys. Rev. B* **62**, R6097 (2000).

[Zherlitsyn10]   S. Zherlitsyn, O. Chiatti, A. Sytcheva, J. Wosnitza, S. Bhattacharjee, R. Moessner, M. Zhitomirsky, P. Lemmens, V. Tsurkan and A. Loidl, *J. Low Temp. Phys.* **159**, 134 (2010).

[Zhitomirsky03] M. E. Zhitomirsky, *Phys. Rev. B* **67**, 104421 (2003).

[Zheng05]   W. Zheng, R. R. P. Singh, R. H. McKenzie, and R. Coldea, *Phys. Rev. B* **71**, 134422 (2005).

Acknowledgements

I am thankful that my time at Frankfurt has been immeasurably enriched by unforgettable friends and colleagues, whom I shall always cherish.

First of all, I would like to extend my biggest gratitude to Prof. Michael Lang for offering me the opportunity and the means to perform this exciting project in his research group. I am grateful to him for always being available for consultations, encouragement and constant interest over the last four years. The discussions with him were highly motivating and inspiring. His passionate research attitude impressed me very much which I someday hope to attain.

Next, I would like to give my most sincere thanks to my second advisor, PD. Dr. Bernd Wolf who directly instruct me during my PhD work. I am deeply indebted to him. Everything I know about the ultrasound and low-temperature technique was taught by him. His friendly personality, patient instruction, constant advice, suggestions, data interpretation, discussions, etc, were crucial for the realization of this investigation and for my professional formation.

This thesis would not have been completed without the numerous collaborators with whom I worked extensively through my research work.

- Good crystals were essential to my experiments. Therefore I would like to thank Prof. Wolf Assmus and his team: Natalija Krüger, Sebastian Belz, Franz Ritter and Amir Haghighirad for proving such wonderful $Cs_2CuCl_xBr_{4-x}$ crystals, as well as their help in cutting and orientating the samples. They also provided many useful discussions. Many thanks to Yulia B. Borozdina and Martin Baumgarten for providing the purely excellent organic spin-1/2 dimers compound.

- Our experimental works were strongly benefited through a rich interaction and cooperation with theoretical researchers: Andreas Kreisel, Kateryna Foyevtsova, Prof. Peter Kopietz and Prof. Roser Valentí, who performed theoretical calculation for analyzing and describing our experimental data that play a crucial role in our investigation. Many thanks to them, not only for these fundamental contributions but also for their enthusiasm, friendly attitude and patience for explaining to us their results and conclusions.

I own a lot to my colleagues, who provide our group with a pleasant environment for working. Special thanks to Rudra Sekhar Manna, Deepshikha Jaiswal-Nagar, Sebastian Köhler and Georg Hofmann for everything - for laughter, sharing, cheering and teasing... for being friends. Many thanks to my office mate, Dr.Ulrich Tutsch, for his patience and many interesting discussions. I also give thanks to Mr. Thomas Dübel, Friedhelm Isselbächer, Dr. Andreas Brühl, Dr. Katarina Removic-Langer, Dr. Mariano de Souza, Daniel Hofmann, Christian Balz, Friedrich Freund, Frank Schnelle, Stephan Knöner, Elena Gati, Lucas Hinz, Lars Postulka, Ammar Naji for their support during the time working in laboratory.

Our group consumed a huge quantity of cryogen but thanks to the work of Mr. Siegfried Rapphahn we never ran out. Besides that, low-temperature experiments are very demanding on the mechanical and electronic support, so I must thank all the people in the electronic and mechanical workshops, for their help in keeping the equipment running smoothly.

To Carolyne Agnew, who is not only an excellent secretary but also a nice and kind person, thank for helping me in preparing official documents and organizing the workshop, proofreading my paper and thesis, for interesting discussions and for all care and support she gave me in all aspects during my time in Frankfurt.

I wish to send my collective thanks to all my friends and my football team in Frankfurt. With them I've shared many nice and memorable moments, from a simple chat to a tournament football match, a summer grill or a fun party. Special thanks go to my closest friends: Hoang lun, Truc gia, Tri beo, Huong, chi Muoi, Duong, Lan, Nhung, Giang thu who have always stood by me during the joyful moments and difficult times.

Finally, with all my love, I dedicate this thesis as thanks to my family. My parent, my aunts (Nguyen Thi Anh Dao and Pham Thi Hop), my brother (Pham Thanh Trung) and my sister (Pham Yen Anh) who have never stopped encouraging, loving me and sacrificing for me. My wife, Vuong Thu Giang has supported and loved me throughout these many years. I thank my son Pham Duc Minh (cu Tit). He inspires my hopes for the future.

This work was completed in the frame of project SFB/Tr 49.

CURRICULUM *VITAE*

.

PERSONAL INFORMATION

First name: THANH CONG

Family name: PHAM

Date of birth: 05th April, 1981

Place of birth: Hanoi, Vietnam

Nationality: Vietnamese

EDUCATION AND ACADEMICS DEGREES

1999 - 2003   **Bachelor of Physics**

College of Science, Vietnam National University Hanoi (VNU)

Bachelor thesis supervised by Prof. Dr. Bach Thanh Cong

2003 - 2005   **Master of Physics**

College of Science, Vietnam National University Hanoi (VNU)

Master thesis supervised by Prof. Dr. Bach Thanh Cong

2005 - 2006   **Researcher**

Department of Physics

College of Science, Vietnam National University Hanoi (VNU)

2006 - 2007   **Researcher**

Department of Physics

College of Science, National Taiwan University (NTU)

2008 - 20012   **PhD student**

Physikalisches Institut, Johann Wolfgang Goethe-Universität

Doctor thesis supervised by PD. Dr. Bernd Wolf and Prof. Dr. Michael Lang

List of Publications Resulting during PhD Time

1. Y.B. Borozdina, E. Mostovich, V. Enkelmann, U. Tutsch, B. Wolf, **P. T. Cong**, M. Lang, G. Zoppellaro and M. Baumgarten
'Synthesis and Physical Characterization of Interacting Networks of Purely Organic Spin-1/2 Dimers' Submitted (2012).

2. B. Wolf, **P. T. Cong**, N. Krüger, F. Ritter, W. Assmus and M. Lang
'Ultrasonic investigations near the B-induced quantum critical point of the triangular-lattice antiferromagnet Cs_2CuCl_4' J. Phys.: Conf. Ser. - accepted (2011).

3. M. Lang, B. Wolf, A. Honecker, Y. Tsui, D. Jaiswal-Nagar, U. Tutsch, G. Hofmann, A. Prokofiev, **P.T. Cong**, N. Krüger, F. Ritter, W. Assmus
'Magnetic cooling through quantum criticality' J. Phys.: Conf. Ser. - accepted (2011).

4. Andreas Kreisel, Peter Kopietz, **Pham Thanh Cong**, Bernd Wolf, Michael Lang
'Elastic constants and ultrasonic attenuation in the cone state of the frustrated antiferromagnet Cs_2CuCl_4' Phys. Rev. B **84**, 024414 (2011).

5. **P. T. Cong**, B. Wolf, M. de Souza, N. Krueger, A. A. Haghighirad, S. Gottlieb- Schoenmeyer, F. Ritter, W. Assmus, I. Opahle, K. Foyevtsova, H. O. Jeschke, R. Valenti, L. Wiehl, M. Lang
'Distinct magnetic regimes through site-selective atom substitution in the frustrated quantum antiferromagnet $Cs_2CuCl_{4-x}Br_x$' Phys. Rev. B **83,** 064425 (2011).

6. Ngoc Hien Phan, Ivan Halasz, Ingo Opahle, Edith Alig, Lothar Fink, Jan W. Bats, **Pham Thanh Cong**, Hans-Wolfram Lerner, Biprajit Sarkar, Bernd Wolf, Harald O. Jeschke, Michael Lang, Roser Valentí, Robert Dinnebier and Matthias Wagner
'Thermally induced crystal-to-crystal transformations accompanied by changes in the magnetic properties of a Cu^{II}-p-hydroquinonate polymer' Cryst. Eng. Comm. **13**, 391 (2011).

7. N. Kruger, S. Belz, F. Schossau, A. A. Haghighirad, **P. T. Cong**, B. Wolf, S. Gottlieb-Schoenmeyer, F. Ritter, and W. Assmus
'Stable Phases of the $Cs_2CuCl_{4-x}Br_x$ Mixed Systems' Cryst. Growth Des. **10**, 4456 (2010).

8. F. Schröder, B. Winkler, E. Haussühl, **P.T. Cong**, B. Wolf, M. Avalos-Borja, M. Quilichini and B. Hennion

'*Low-temperature structural phase transition in deuterated and protonated lithium acetate dihydrate*' J. Chem. Thermodynamics **42**, 957 (2010).

9. **P. T. Cong**, B. Wolf, U. Tutsch, K. Remović-Langer, J. Schreuer, S. Süllow and M Lang

'*Ultrasonic investigation on the distorted diamond chain compound Azurite*' J. Phys.: Conf. Ser. **200,** 012226 (2010).

10. B Wolf, **P T Cong**, K Remović-Langer, Y D Borozdina, E Mostovich, M Baumgarten and M Lang

'*Coupled spin S = 1/2 dimer systems based on nitronyl-nitroxide biradicals*' J. Phys.: Conf. Ser. **200,** 012225 (2010).

11. Bach Thanh Cong, Pham Huong Thao and **Pham Thanh Cong**

'*Theory for long range magnetic order in nanometer films*' J. Phys.: Conf. Ser. **200,** 072020 (2010).

Talks and Posters Presented in Conferences and Workshops during PhD Time

1) '*Search for coupled S = 1/2 dimer systems in a new class of Nitronyl-nitroxides biradicals*' German spring meeting (Deutsche Physikalische Gesellschaft) - Berlin, Germany (25th - 29th February, 2008).

2) '*Quantum spin systems based on Nitronyl-nitroxid biradicals*' Annual retreat SFB/TR 49 - Waldthausen, Mainz (25th - 26th September, 2008).

3) '*Coupled spin S = 1 /2 dimer-systems based on Nitronyl-nitroxide biradicals*' German spring meeting (Deutsche Physikalische Gesellschaft) - Dresden, Germany (22th - 27th March, 2009).

4) '*Ultrasonic investigations on the 1D diamond chain compound Azurite*' German spring meeting (Deutsche Physikalische Gesellschaft) - Dresden, Germany (22th - 27th March, 2009).

5) *'Exploring the quasi 2d-antiferromagnet Cs_2CuCl_4 by ultrasonic investigations'* The 9th International Conference on Research in High Magnetic Fields (RHMF 2009) - Dresden, Germany (22th - 25th July, 2009).

6) *'Ultrasonic investigations on the distorted diamond chain compound Azurite'* - International Conference on Magnetism (ICM) - Karlsruhe, Germany (26th - 31st July, 2009).

7) *'Exploring the quasi 2d-antiferromagnet Cs_2CuCl_4 by ultrasonic investigations'* Annual Retreat SFB/TR 49 - Akademie Gesundes Leben, Oberursel (24th -25th September, 2009).

8) *'Elastic anomalies at the field-induced quantum-critical point in the quasi 2D-antiferromagnet Cs_2CuCl_4'* SFB International Symposium on "Novel states in correlated condensed matter – from model systems to real materials" - Berlin, Germany (2nd - 4th March, 2010).

9) *'Elastic anomalies at the field-induced quantum-critical point in the quasi 2D-antiferromagnet Cs_2CuCl_4'* German spring meeting (Deutsche Physikalische Gesellschaft) - Regensburg, Germany (21st - 26th March, 2010).

10) *'Structural and magnetic properties of the mixed quantum antiferromagnet $Cs_2CuCl_{4-x}Br_x$'* German spring meeting (Deutsche Physikalische Gesellschaft) - Regensburg, Germany (21st - 26th March, 2010).

11) *'Elastic anomalies at the field-induced quantum-critical point in the quasi 2D-antiferromagnet Cs_2CuCl_4'* Annual retreat SFB/ TR 49 - Seehotel Gelterswoog, Kaiserslautern, Germany (7th - 8th October, 2010).

12) *'Ultrasonic investigation in the vicinity of the quantum-critical point in Cs_2CuCl_4'* German spring meeting (Deutsche Physikalische Gesellschaft) - Dresden, Germany (13th - 18th March, 2010).

13) *'Distinct magnetic regimes through site-selective atom substitution in the frustrated quantum antiferromagnet $Cs_2CuCl_{4-x}Br_x$'* German spring meeting (Deutsche Physikalische Gesellschaft) - Dresden, Germany (13th - 18th March, 2011).

14) '*Critical behavior study at antiferromagnetic phase transition in Azurite'* German spring meeting (Deutsche Physikalische Gesellschaft) - Berlin, Germany (25th - 30th March, 2012).

15) '*Pulse field ultrasonic experiments in the quasi-2d antiferromagnet Cs_2CuBr_4*' German spring meeting (Deutsche Physikalische Gesellschaft) - Berlin, Germany (25th - 30th March, 2012).

Teaching Assistantship during PhD Time

1) Winter Semester 2007-2008 - Teaching Assistant for the experiment '*Optical Pumping*' Advance laboratory course for Physics students, J. W. Goethe-Universität Frankfurt, Germany.

2) From summer Semester 2008-2009 to winter semester 2011-2012 - Teaching Assistant for the experiment '*Sound Propagation in Crystals'* - Advance laboratory course for Physics students, J. W. Goethe-Universität Frankfurt, Germany.

3) From summer Semester 2011 to winter semester 2011-2012 - Teaching Assistant for the experiment '*Josephson Effect*' - Advance laboratory course for Physics students, J. W. Goethe-Universität Frankfurt, Germany.